Noninvasive Assessment of Photoreceptor Structure and Function in the Human Retina

Robert Francis Cooper
Marquette University

NONINVASIVE ASSESSMENT OF PHOTORECEPTOR STRUCTURE AND FUNCTION IN THE HUMAN RETINA

By

Robert F Cooper, B.S.

A Dissertation submitted to the Faculty of the Graduate School,
Marquette University,
in Partial Fulfillment of the Requirements
for the Degree of Doctor of Philosophy

Milwaukee, Wisconsin

December 2015

ABSTRACT
NONINVASIVE ASSESSMENT OF PHOTORECEPTOR STRUCTURE AND FUNCTION IN THE HUMAN RETINA

Robert F Cooper, B.S.

Marquette University, 2015

The human photoreceptor mosaic underlies the first steps of vision; thus, even subtle defects in the mosaic can result in severe vision loss. The retina can be examined directly using clinical tools; however these devices lack the resolution necessary to visualize the photoreceptor mosaic. The primary limiting factor of these devices is the optical aberrations of the human eye. These aberrations are surmountable with the incorporation of adaptive optics (AO) to ophthalmoscopes, enabling imaging of the photoreceptor mosaic with cellular resolution. Despite the potential of AO imaging, much work remains before this technology can be translated to the clinic.

Metrics used in the analysis of AO images are not standardized and are rarely subjected to validation, limiting the ability to reliably track structural changes in the photoreceptor mosaic geometry. Preceding the extraction of measurements, photoreceptors must be identified within the retinal image itself. This introduces error from both incorrectly identified cells and image distortion. We developed a novel method to extract measures of cell spacing from AO images that does not require identification of individual cells. In addition, we examined the sensitivity of various metrics in detecting changes in the mosaic and assessed the absolute accuracy of measurements made in the presence of image distortion. We also developed novel metrics for describing the mosaic, which may offer advantages over more traditional metrics of density and spacing. These studies provide a valuable basis for monitoring the photoreceptor mosaic longitudinally. As part of this work, we developed software (Mosaic Analytics) that can be used to standardize analytical efforts across different research groups.

In addition, one of the more salient features of the appearance of individual cone photoreceptors is that they vary considerably in their reflectance. It has been proposed that this reflectance signal could be used as a surrogate measure of cone health. As a first step to understanding the cellular origin of these changes, we examined the reflectance properties of the rod photoreceptor mosaic. The observed variation in rod reflectivity over time suggests a common governing physiological process between rods and cones.

TABLE OF CONTENTS

LIST OF ABBREVIATIONS

AOIP – Advanced Ocular Imaging Program

AOSLO – Adaptive Optics Scanning Light Ophthalmoscope

AO – Adaptive Optics

API – Application Programming Interface

CCD – Charge-Coupled Device

cGMP – Cyclic Guanosine-Monophosphate

CHC – Cumulative Histogram Comparisons

CI – Confidence Interval

DFT – Discrete Fourier Transform

DM – Deformable Mirror

DRP – Density Recovery Profile

DRPD – Density Recovery Profile Distance

ERG – Electroretinogram

FFT – Fast Fourier Transform

FOV – Field of View

GDP – Guanosine-Diphosphate

GMP – Guanosine-Monophosphate

GTP – Guanosine-Triphosphate

GUI – Graphical User Interface

ICC – Intra-class Correlation Coefficient

ICD – Inter-Cell Distance

IS – Inner Segment

LC – Liquid Crystal

LGN – Lateral Geniculate Nucleus

LSO – Line-Scan Ophthalmoscope

NCC – Normalized Cross-Correlation

NND – Nearest Neighbor Distance

NNR – Nearest Neighbor Regularity

NoNR – Number of Neighbors Regularity

OCT – Optical Coherence Tomography

OS – Outer Segment

PDE – Phosphodiesterase

PI – Prediction Interval

PSV – Pixel Shift Vector

RMF – Retinal Magnification Factor

RMS – Root Mean Square

RNFL – Retinal Nerve Fiber Layer

ROI – Region of Interest

RPE – Retinal Pigment Epithelium

SHWS – Shack-Hartmann Wavefront Sensor

SLD – Superluminescent Diode

SNR – Signal-to-Noise Ratio

UI – User Interface

VCAR – Voronoi Cell Area Regularity

LIST OF FIGURES

LIST OF TABLES

Chapter One: General introduction

The Human Visual System

Vision is arguably the most valued of the five human senses; information provided by the visual system drives how we interpret, navigate, and interact with our world. The primacy of vision is reflected in our brain, where the amount of cortex dedicated to vision is greater than any other sense. The process of vision is initiated by the eye, where an image of our environment is focused, captured, and initially processed.

Optical examination of internal structures of the eye began as early as 1704 when Jean Méry observed feline retinal vasculature and optic disk structure (Méry, 1704). Subsequent observations of the internal structures of the eye were facilitated by Charles Babbage's invention of the ophthalmoscope in 1847, and subsequent implementation by Herman Helmholtz (Helmholtz, 1851). Modern versions of his original design are principally the same and are still in use today, allowing direct observation of gross structures within the eye.

Even when viewed externally, the eye is distinctive from the rest of the human body, with a porcelain white exterior surrounding a clear window to the colorful and complex iris. These so-called "whites" of the eye consist of a collagen and elastin shell called the sclera. Other ocular structures, the cornea and optic nerve, protrude through anterior and posterior openings in the eye, respectively (**Figure 1.1**). The cornea is a clear structure consisting of ordered collagen layers, which, in addition to allowing light to enter the eye, is responsible for about 80% of the eye's refractive power.

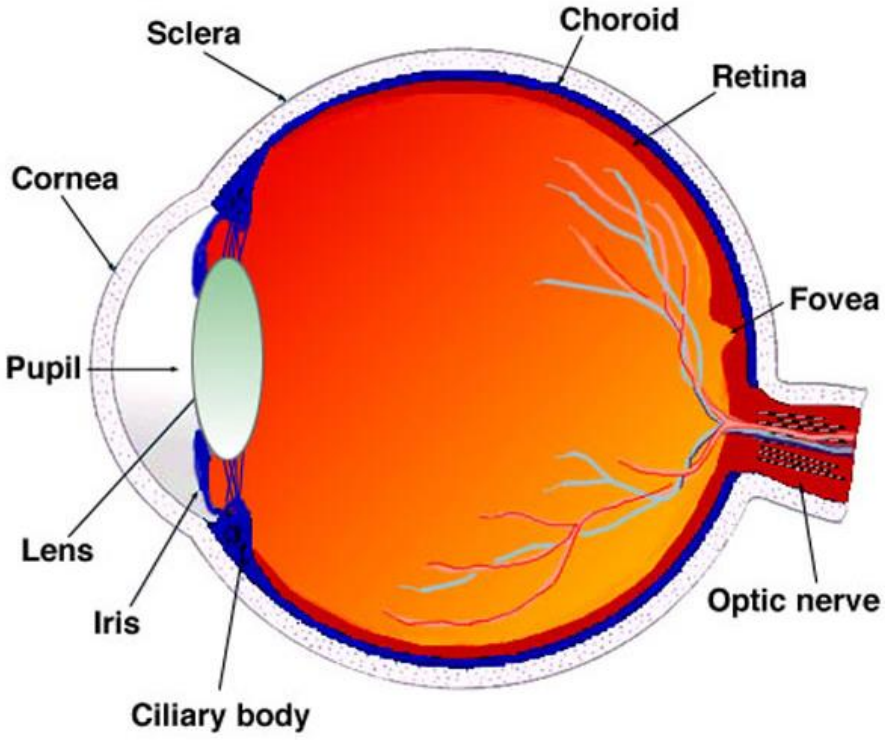

Figure 1.1: A schematic sagittal section through the human eye. (Image Courtesy Webvision; http://webvision.med.utah.edu/book/)

Posterior to the cornea are fluid filled regions called the anterior and posterior chambers. The iris is positioned between the anterior and posterior chambers. It is primarily responsible for regulating how much light enters the globe. Immediately posterior to the iris is the crystalline lens. Surrounding the lens is the ciliary body, which consists of both the ciliary muscle and the ciliary epithelium. The ciliary muscle enables the lens to change shape in order to focus, or accommodate, in response to the desire to focus on either a near or a far object. The ciliary epithelium is responsible for secreting aqueous humor, which maintains intraocular pressure and nutritional balance for the structures it contacts within the anterior and posterior chambers. Posterior to both the anterior and posterior chambers within the vitreous chamber is a transparent gelatinous globe called the vitreous humor that provides structural support for the surrounding retina and sclera.

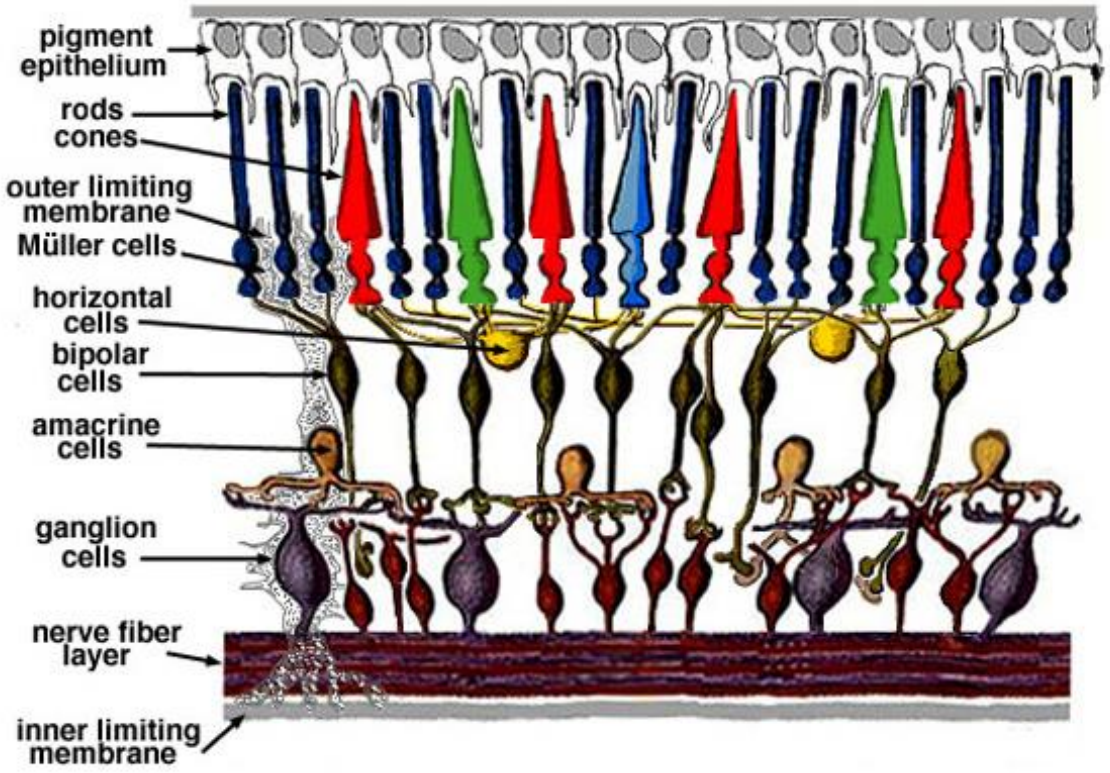

Figure 1.2: A schematic enlargement of the human retina. In this orientation, light enters the retina from the bottom of the image, passing through the transparent inner retina before contacting the photoreceptors. The neural signal then initiates in the photoreceptors and propagates in the opposite direction. (Image courtesy Webvision; http://webvision.med.utah.edu/book/)

Lining the inside of the sclera within the vitreous chamber is a vascular support structure known as the choroid. The choroid is responsible for supplying metabolites to and removing waste from the outer retinal layers. Anterior to the choroid is Bruch's membrane, a five-layered membrane that serves two major functions as both the substratum of the retina and as a vessel wall to the choroid. Adjacent to Bruch's membrane is the retinal pigment epithelium (RPE) (**Figure 1.2**). The RPE has two primary purposes: to absorb any excess light that passes the photoreceptors, and to serve as a custodian of cell waste and metabolic balance. Towards the center of the globe and immediately adjacent to the RPE are the photoreceptors.

Photoreceptors are the primary photosensitive structure within the eye, and are responsible for the first step in vision; the detection of light. The human retina contains two classes of photoreceptor, cones and rods. Cone photoreceptors enable high spatial acuity and color vision. Within a normal trichromatic individual, there are three cone subtypes as defined by the peak spectral sensitivities of the photopigment opsins expressed within each cone cell: long, medium, and short wavelength opsins correspond to peak cone photoreceptor spectral sensitivities of 559nm, 530nm, and 419nm, respectively (Sharpe, Stockman, Jägle, & Nathans, 1999). Short wavelength cones (S-cones) account for an average of about 6% of the cone population in the retina (Curcio et al., 1991; Roorda & Williams, 1999). In contrast, the relative densities of long (L) and medium (M) cones vary substantially between normal individuals, with ratios between L and M cones being recorded as high as 16.5:1 or as low as 1:3 (Carroll, McMahon, Neitz, & Neitz, 2000; Hofer, Carroll, Neitz, Neitz, & Williams, 2005; Roorda & Williams, 1999). Despite the spectral specialization of each cone type, stimulating a cone requires thousands of photons, making the cell type poorly suited for low-light conditions. The other class of photoreceptor in the human retina is the rod photoreceptor. In contrast to cones, all rods contain the same photopigment, rhodopsin, which has a peak spectral sensitivity of 500nm. Moreover, a rod is able to respond to a single photon of light, allowing vision even in extremely scotopic conditions. Across the entire retina, rods substantially outnumber cones at a ratio of about 20:1. However, rod output saturates at a very low light level. This means that in most conditions human vision is dependent solely on cone photoreceptors.

Toward the center of the eye and overlaying the photoreceptors is a network of neural circuitry that contains a variety of neuron types responsible for carrying the photoreceptor signal to the brain. Bipolar cells are directly connected to the photoreceptors, and feature a graded neurotransmitter response as the photoreceptor is

exposed to light. Horizontal cells, along with amacrine cells, laterally inhibit bipolar cells. Cone bipolar cells and amacrine cells innervate ganglion cells, which project to the lateral geniculate nucleus (LGN) through the optic nerve. From the LGN the visual signal is further processed and projected to the cortex, where visual perception occurs. All of work herein will concentrate on the photoreceptor layer.

The Human Photoreceptor Mosaic

The arrangement of the photoreceptor types in the retina is well described histologically (Curcio, Sloan, Kalina, & Hendrickson, 1990; Polyak, 1957; Pum et al., 1990). The cone and rod photoreceptors are closely packed, forming a patterned appearance, or mosaic. Previous literature has remarked upon the fact that the human photoreceptor mosaic is packed in a nearly hexagonal manner (Ahnelt & Kolb, 2000; Coletta & Williams, 1987; Hirsch & Hylton, 1984; Polyak, 1957; Pum et al., 1990). As stated previously, rods substantially outnumber cones over the entire retina. In the developing human retina, the relative distribution of cone and rod photoreceptors is roughly constant; that is, a 20:1 ratio is maintained across the entire retina. However, across an adult retina, the ratio of rods to cones varies substantially. The adult fovea contains the highest density of cone photoreceptors, enabling high acuity vision. However, the density of cone photoreceptors quickly falls off as a function of distance from the fovea, yielding to a high density of rod photoreceptors, which peaks at about 10 degrees from the fovea (**Figure 1.3**).

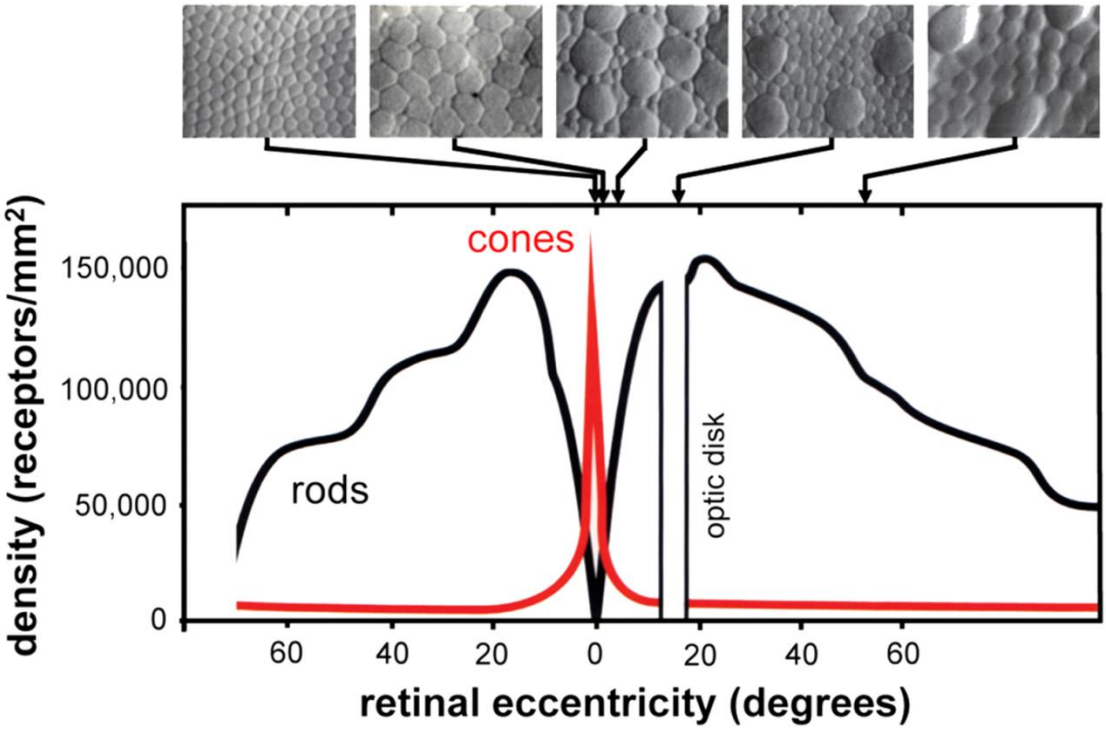

Figure 1.3: The densities of rods and cones in the adult human retina as a function of retinal eccentricity. In a normal retina, the foveal center (< 3°) is cone-dominated, whereas the peripheral regions (> 10°) are rod-dominated. (Hofer, Carroll, & Williams, 2009; Roorda & Williams, 1999)

In addition, the distribution of cone subtypes varies with eccentricity. S-cones are largely absent in the "S-cone free zone" which is within 0.35 degrees of peak cone density. S-cones increase in density radially and peak between 0.35-1.05 degrees from the fovea. Ultimately, their density decreases asymptotically as a function of eccentricity. L and M-cone distributions as a function of eccentricity have not yet been characterized, in part due to their substantially varied relative densities (Roorda & Williams, 1999).

Photoreceptor Structure and Function

The structure of an individual vertebrate photoreceptor consists of the synaptic terminal, cell body, and two major functional parts (**Figure 1.4**): the outer segment (OS),

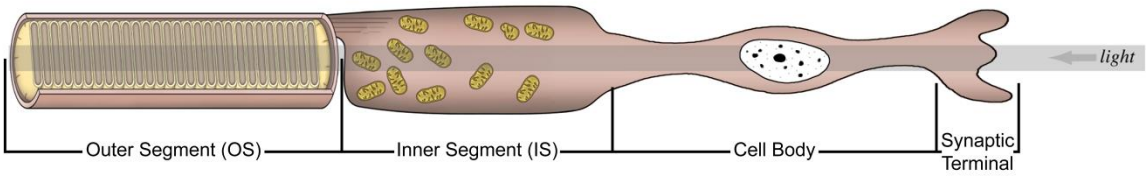

Figure 1.4: The structure of a single of rod photoreceptor from the adult human retina. The outer segment (OS) of a photoreceptor houses the machinery necessary to detect light. The inner segment (IS) is responsible for the production of energy and metabolites that will be shipped to the outer segment. The cell body is responsible for mediating cell function, and synaptic terminals are responsible for carrying the signal to the innervated bipolar cells.

and inner segments (IS). The IS of a photoreceptor is responsible for housing the production of energy and metabolites required for the photoreceptor to detect light. The OS houses the machinery needed to detect light. In the human, IS and OS diameters increase between the foveal and peripheral regions. In the fovea, cones are 1-3 μm in diameter (Hoang, Linsenmeier, Chung, & Curcio, 2002). Rods near the fovea have a diameter of approximately 1 μm (Polyak, 1941). In the near-periphery, cone IS are approximately 6 μm in diameter, with corresponding diameters of 3 μm and 1 μm at the base and tip of the OS, respectively (Pugh & Lamb, 2000). Rods can be as wide as 2.5 μm in the far periphery (Polyak, 1941).

Both cones and rods are depolarized in the dark, and slowly release a “dark current” of glutamate. When exposed to light, the photoreceptors hyperpolarize. This hyperpolarization is enabled through a process called the phototransduction cascade. The process of phototransduction begins when a photon hits a photoreceptor opsin. The first step in the cascade is the absorption of a photon of light by the photopigment inside the photoreceptor. Photopigments have two parts, a chromophore (11-cis retinal) and a protein (opsin). When a photon is absorbed by the photopigment, it results in the isomerization of the chromophore retinal from 11-cis to all-trans. This in turn results in a release of the chromophore and a conformational change, causing the opsin to be

“activated”. The activated opsin then activates transducin at a ratio of approximately 1:20(Krispel et al., 2006) in rods, and at about 1:10 cones (Nikonov, Kholodenko, Lem, & Pugh Jr., 2006). The activated transducin binds to guanosine-triphosphate (GTP), and activates phosphodiesterase (PDE). PDE is an enzyme that catalyzes the breakdown of cGMP to GMP, at a ratio of up to 1 PDE to 6 GMP (Purves et al., 2011) in rods, and about 2.4 in cones (Nikonov et al., 2006). The reduction in cGMP concentration closes the photoreceptor’s cyclic-nucleotide gated ion channels, which results in a very small (~2%) hyperpolarization of the cell. This hyperpolarization ultimately results in a significantly reduced glutamate release at the photoreceptor synaptic terminal.

Inactivation of the cascade in the absence of light is immediate. In rods, the activated rhodopsin is inactivated by a two-step process. First, activated rhodopsin is phosphorylated by rhodopsin kinase (GRK1), reducing the activity of activated rhodopsin. Next, the protein arrestin binds to the activated rhodopsin, further suppressing its activity (Kuhn & Wilden, 1987). Activated transducin is inactivated when its GTP is hydrolyzed into GDP. This inactivation process is most completely characterized in rods; however, there is evidence that much of the inactivation process is paralleled in cones (Tachibanaki, Arinobu, Shimauchi-Matsukawa, Tsushima, & Kawamura, 2005; Tachibanaki, Tsushima, & Kawamura, 2001; Weiss et al., 2001).

Many retinal diseases are associated with disruption of photoreceptor structure and function, including albinism, retinitis pigmentosa, Usher syndrome, cone-rod dystrophy, rod-cone dystrophy, colorblindness, age-related macular degeneration, and geographic atrophy. In humans, these pathologies are typically tracked using clinical instruments which have resolution limited to gross retinal structures, thereby limiting the ability to effectively track disease progression. Adaptive optics ophthalmoscopy can be applied to assess these pathologies on a cellular scale, allowing a finer view of retinal disease progression.

Adaptive Optics Imaging of the Human Retina *In Vivo*

Despite the diverse ophthalmic imaging modalities currently available, the resolution of clinical devices is limited by the optically aberrated characteristics of the human eye. In order to mitigate the effect of these aberrations, adaptive optics (AO) can be applied. AO is an approach to correct the eye's monochromatic aberrations in order to achieve near-diffraction limited optical quality, resulting in a high-resolution image. The proposed use of AO was in astronomical telescopes (Babcock, 1953), but it can be adapted to any optical system where light passes through an aberrated medium. Moreover, AO can be applied to all conventional ophthalmic imaging techniques. For example, incorporating AO in to a standard fundus camera offers a high-resolution improvement over the low-resolution flash-lamp fundus camera (Bedggood & Metha, 2012; Dees, Dubra, & Baraas, 2011; Liang, Williams, & Miller, 1997; Rha, Jonnal, Thorn, et al., 2006). Another ophthalmic modality that can be adapted to AO is the confocal scanning laser ophthalmoscope (cSLO). One of the chief benefits of a cSLO is its ability to perform optical sectioning. The gains in contrast that are achieved by using a confocal pinhole increase substantially when augmented by AO (Burns, Tumbar, Elsner, Ferguson, & Hammer, 2007; Dubra & Sulai, 2011; Roorda et al., 2002)(**Figure 1.5**). Finally, some investigators have applied AO to OCT to greatly improve the lateral resolution of the modality (Pircher & Zawadzki, 2007; Torti et al., 2009; Zawadzki et al., 2009; Zhang, Rha, Jonnal, & Miller, 2005).

Regardless of the modality that is paired with AO, most ophthalmoscopes follow a similar design principle (**Figure 1.6**). First, the light from the retina is detected by a wavefront sensor in order to measure the aberrations

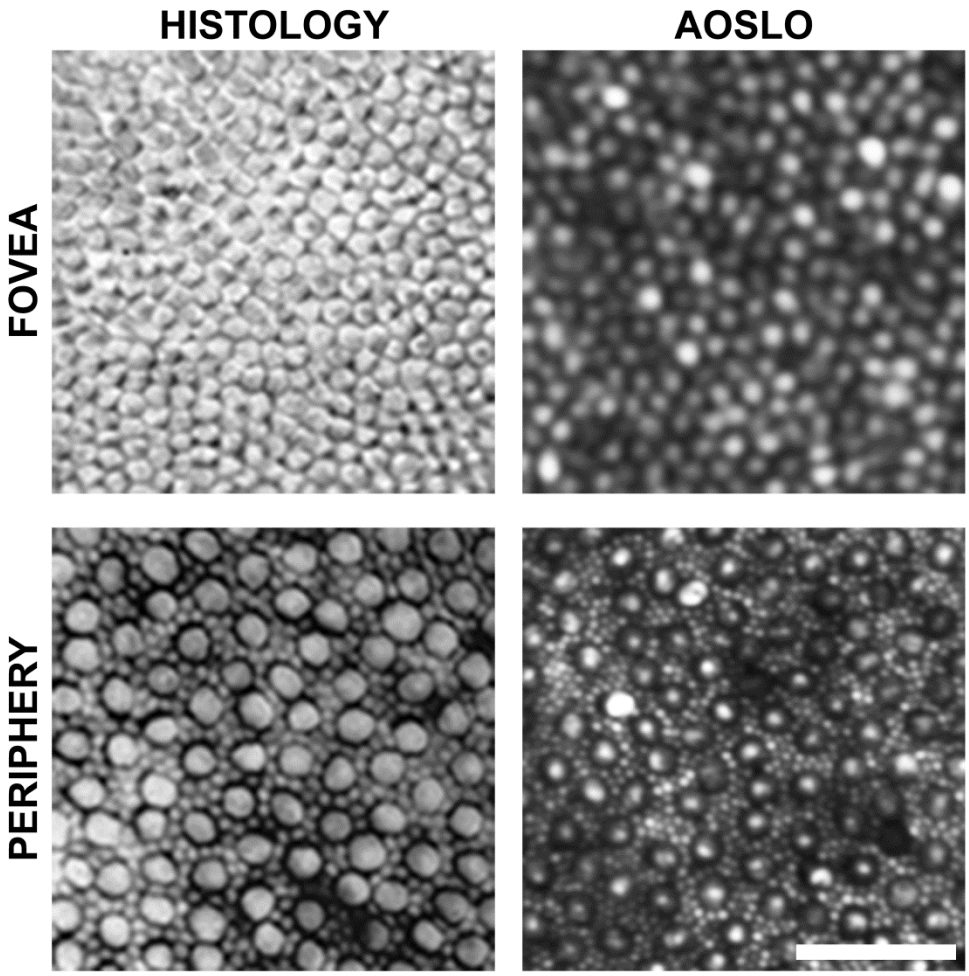

Figure 1.5: Images of the photoreceptor mosaic, acquired from histology (A,C) (Polyak), and AOSLO (B, D). At both foveal (A,B) and peripheral (C,D) locations, similar structures are visible; however, using an AOSLO, images can be obtained *in vivo*. Scale bar is 50 µm.

(Liang, Grimm, Goelz, & Bille, 1994). Every optical system, be it the optics of the human eye, the optics of a telescope, or the optics of the atmosphere, has innate imperfections called aberrations that degrade a flat wavefront (**Figure 1.7**) and hinder the ability of any optical system to perform at its theoretical limit. Accurately detecting the wavefront of an optical system is required for any advanced correction technique, such as AO.

There are a variety of methods for determining a wavefront, such as use of a refractometer, laser ray tracing, or use of a pyramidal sensor

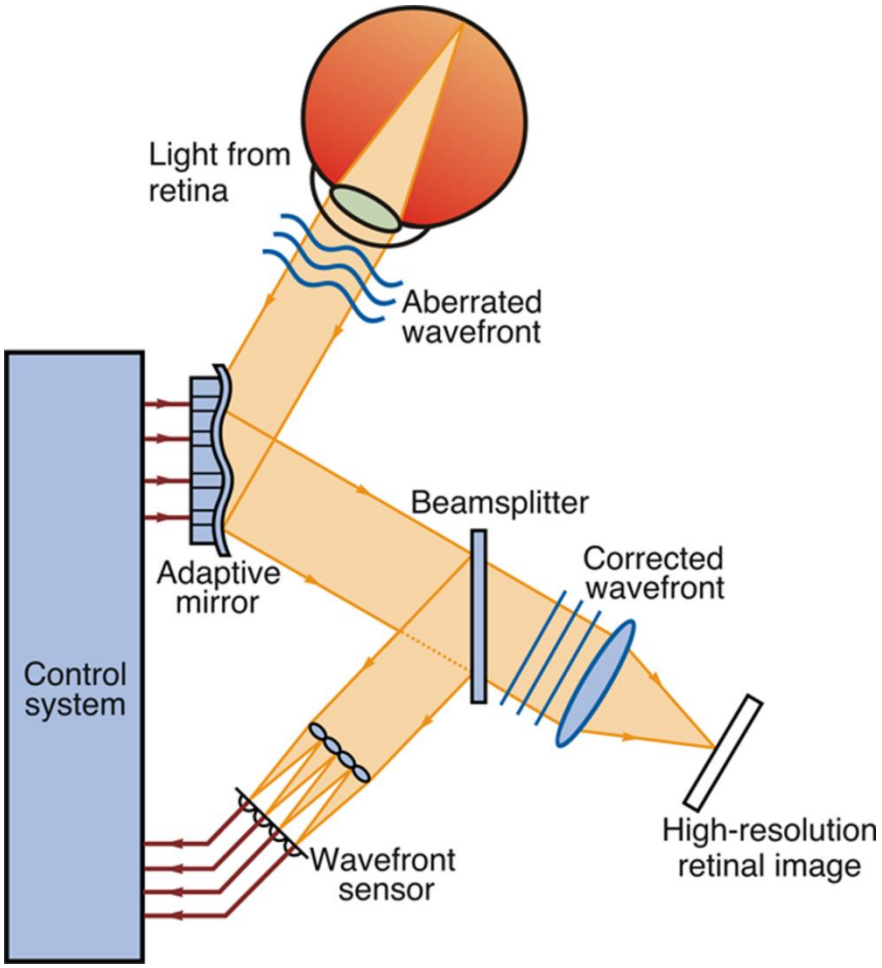

Figure 1.6: A schematic of the standard design principle of AO. Light that is convolved with the aberrations in the human eye is measured by a wavefront sensor. The inverse of the estimated wavefront is calculated and the mirror is adjusted to closely match this inverse. This calculation is run in a closed loop until a high-resolution image is acquired.

(Iglesias, Ragazzoni, Julien, & Artal, 2002). While each is capable of characterizing the aberrations present in an optical system, the most widely used sensor in vision science is the Shack-Hartmann wavefront sensor.

The Shack-Hartmann wavefront sensor (SHWS) allows the quantification of an incoming wavefront by detecting the derivative of the shape of the wavefront(Liang et al., 1994; Liang et al., 1997). It accomplishes this by coupling a two dimensional lenslet array to a charge-coupled device (CCD) image sensor. When incident light passes through the lenslets, it is focused on to the CCD sensor. In a flat wavefront (**Figure**

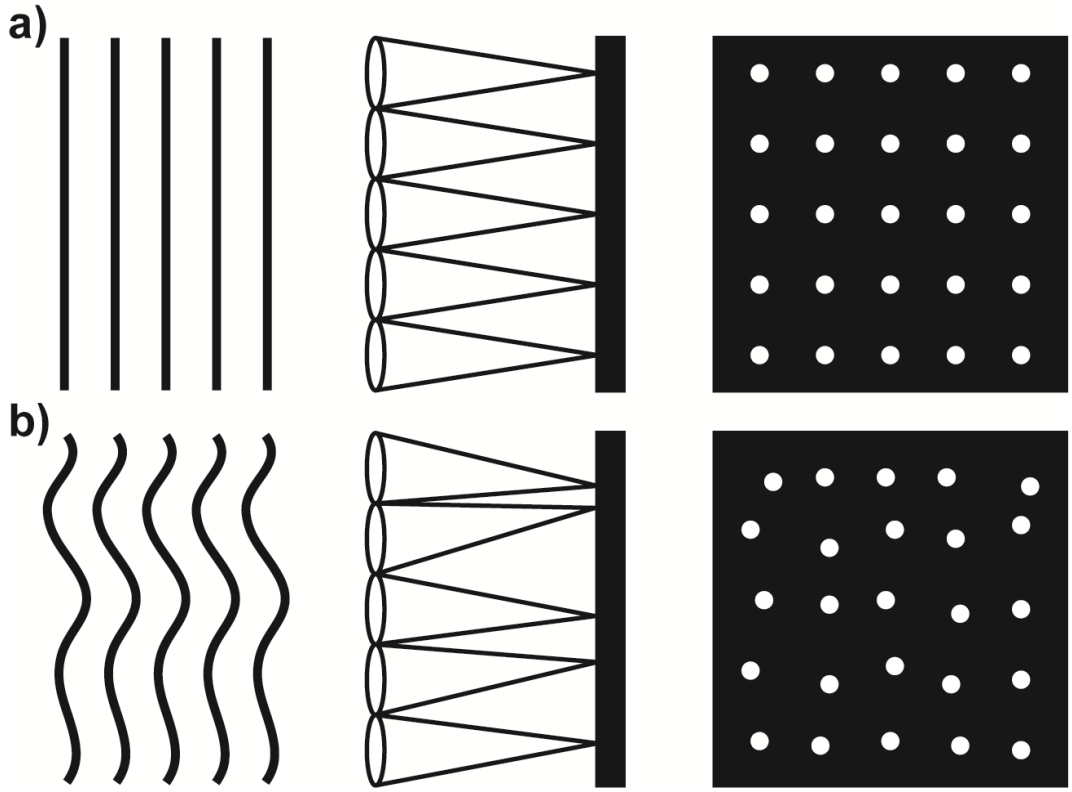

Figure 1.7: (a) A Shack-Hartmann wavefront sensor, showing the centered spots when the incident wavefront is perfectly flat. b) The spots displace from their centers when an aberrated waveform is incident on the lenslets.

1.7a)**,** this creates a pattern of evenly spaced spots that is considered the zero-slope or origin location for each lens. When an aberrated wavefront passes through the same lenslet array (**Figure 1.7b**)**,** the spots displace from their origin. The displacement from each lenslet's origin is directly related to the slope of the wavefront at that lenslet sampling location. This relationship is described by **Equations 1.1** and **1.2**, where $\delta W(x,y)$ are the slopes of the wavefront in x and y, Δy_s and Δx_s are the displacements on the detector, and F is the focal length of the lenslet array.

$$\frac{\delta W(x,y)}{\delta y} = \frac{\Delta y_s}{F} \qquad \textbf{(Eq. 1.1)}$$

$$\frac{\delta W(x,y)}{\delta x} = \frac{\Delta x_s}{F} \qquad \textbf{(Eq. 1.2)}$$

When the spot displacement for each lenslet is calculated, the wavefront can be reconstructed and used for correction.

Once the wavefront has been quantified, the information is passed to a corrective device to begin the process of wavefront correction. There are a variety of corrective devices available for AO systems. These devices include deformable mirrors (DMs), and liquid crystal spatial light modulators (LC-SLMs). DMs come in many different forms (Hardy, 1998; Tyson, 1997), however all DMs adhere to a basic principle: a mirror whose surface can modified by actuators behind the mirror's surface. In order to correct an incident wavefront, the DM surface is modulated to become the inverse of the estimate of the aberrated waveform divided by two, effectively nullifying the estimation of the aberrations detected by the SHWS. LC-SLMs accomplish a similar 'surface' modulation by changing the index of refraction at a single pixel. This acts similar to a deformable mirror. The component that will be used for these projects is a deformable mirror.

Correcting the sensed wavefront is an iterative process, and therefore optimization methods (such as least squared error and derivatives) are commonly used to minimize the amount of detected aberrations in a closed loop. Once the system has reached a minimum, the optical quality of the system will be close to the theoretical diffraction limit. This allows for high resolution image acquisition.

Assessing Adaptive Optics Images of the Photoreceptor Mosaic

AO has been used to resolve multiple structures within the human retina. Cone (Liang et al., 1997; Miller, Kocaoglu, Wang, & Lee, 2011; Scoles, Higgins, et al., 2014; Williams, 2011), and rod (Dubra et al., 2011; Merino, Duncan, Tiruveedhula, & Roorda, 2011; Rossi et al., 2011) photoreceptors have been the most common focus for research groups (**Figure 1.5**), but other structures such as the RPE (Masella et al., 2007; Morgan

et al., 2008b; Roorda, Zhang, & Duncan, 2007; Scoles, Sulai, & Dubra, 2013; Torti et al., 2009), retinal vasculature (Burns et al., 2008; Martin & Roorda, 2009; Popovic, Knutsson, Thaung, Owner-Peterson, & Sjöstrand, 2011; Tam et al., 2011; Tam, Martin, & Roorda, 2010; Zhong, Petrig, Qi, & Burns, 2008), and retinal nerve fiber layer (RNFL) (Kocaoglu, Cense, et al., 2011; Scoles, Sulai, Manguikian, Shareef, & Dubra, 2012; Takayama et al., 2012; Takayama et al., 2013) have also been visualized using AO tools.

Currently, a variety of geometric and statistical algorithms are used to objectively assess the structure of the photoreceptor mosaic. The most basic and widely used is cell density (Chiu et al., 2013; Chui, Song, & Burns, 2008b; Dees et al., 2011; Flatter et al., 2014; Garrioch et al., 2012; Godara, Wagner-Schuman, et al., 2012; Hansen, Cooper, Dubra, Carroll, & Weinberg, 2013; Kay et al., 2013; Li, Tiruveedhula, & Roorda, 2010; Lombardo, Lombardo, et al., 2013; Lombardo, Serrao, & Lombardo, 2014; Menghini et al., 2015; Park, Chung, Greenstein, Tsang, & Chang, 2013; Song, Chui, Zhong, Elsner, & Burns, 2011). This metric is often used as a litmus test of retinal structure; subjects whose densities are substantially lower than previously observed normal subjects are considered to have a pathological retina. As mentioned previously, the human photoreceptor mosaic is packed in a nearly triangular manner, and this morphology enables the ability to calculate cone photoreceptor density from cell spacing by assuming the cones are arranged in a perfect lattice. It was observed that one can use a 2D Fourier domain image to extract the dominant spacing of the cells in the image (Yellott, 1982). Previous researchers have also calculated cell-to-cell spacing using photoreceptor coordinates (Chiu et al., 2013; Duncan et al., 2007; Garrioch et al., 2012; Mkrtchyan, Lujan, Merino, Roorda, & Duncan, 2012; Park et al., 2013; Ratnam, Västinsalo, Roorda, Sankila, & Duncan, 2013; Roorda, Metha, Lennie, & Williams, 2001; Roorda & Williams, 2002; Roorda et al., 2007; Scoles, Sulai, et al., 2014; Syed et al.,

2013; Yoon et al., 2009). Additionally, research groups derive so-called “regularity measurements” (Baraas et al., 2007; Carroll, Rossi, et al., 2010; Dees et al., 2011; Li & Roorda, 2007; Morgan et al., 2007), which assay the expected number of Voronoi sides for photoreceptor locations within a human photoreceptor mosaic.

In addition to measuring the numerosity and arrangement of the photoreceptor mosaic, investigators have begun to use AO to examine the function of the photoreceptors in order to detect subtle changes in function. For example, Makous *et al*. (2006) showed that a patient missing 35% of his cones had normal acuity, normal visual fields, and normal ERG. A significant deficit was revealed only after an AO technique was used to deliver small stimuli to the retina and assess retinal sensitivity. Makous’ application of small stimuli to the retina was further refined by Arathorn *et al*. (2008) using stimuli stabilization. This technique enabled targeted stimulation of a single photoreceptor in order to probe psychophysical properties of human vision.

In addition to allowing psychophysical probes of photoreceptor function, AO has been combined with retinal densitometry to infer the pigment type of individual cone photoreceptors (Roorda et al., 2001; Roorda & Williams, 1999). Moreover, the reflectance of the photoreceptor mosaic has been used as an optophysiological assay of cell function (Jonnal et al., 2007; Rha, Jonnal, Zhang, et al., 2006; Rha, Jonnal, Zhang, & Miller, 2005).

Despite these advances in assessing the photoreceptor mosaic’s structure and function, considerable work remains. In particular, there remain substantial gaps in our understanding of how each metric will change in due to pathology, eccentricity, and image quality. Moreover, tools for analyzing images of the photoreceptor mosaic are not standardized and there has been minimal validation regarding their ability to detect and monitor retinal degeneration. Finally, examination of the origins of photoreceptor reflectance is essential for solidifying the relevance of AO instrumentation not only as a

research tool but also as clinical diagnostic tool. These topics are the focus of this dissertation and of all of the work therein.

Summary of Dissertation Aims

Even with the potential of AO imaging devices to assay the human retina, there remains much work to be done in the translation of the technology to vision research. The focus of these works was to develop a set of validated, robust, and freely available tools, and to apply them to assay the photoreceptor mosaic's structure and function. This was accomplished through the following aims:

Specific Aim 1: Examine the sensitivity of metrics of photoreceptor structure.

Specific Aim 2: Develop improved retinal imaging systems, tools, and analyses to assess human photoreceptor structure.

Specific Aim 3: Examine the origin of changes in photoreceptor reflectivity.

Each of these aims was accomplished using with distinct experimental protocols containing common aspects; these commonalities will be described in detail within Chapter 2, and referred to throughout the dissertation. Multiple projects seek to address the first aim of this dissertation.

First, Chapter 3 explores the relationship between in-use and recently developed metrics of photoreceptor structure and how each is affected by changes in retinal eccentricity and photoreceptor undersampling. Chapters 4 and 5 focus on the development of new approaches for measuring photoreceptor arrangement. Most measurements of photoreceptor mosaic geometry are derived from photoreceptor locations, which in turn are derived from an image. In cases where image quality is poor, extracting cell locations can provide inaccurate results. Chapter 4 introduces an automated approach for a purely image-based extraction of photoreceptor arrangement.

Foveal cones are arranged in a tightly packed hexagonal mosaic, and it has been observed that cones within it form sub-mosaics with distinct orientations. It is thought that these orientations could provide an assay of foveal health. To examine this, Chapter 5 examines three measurements of photoreceptor submosaic orientation, and attempts to assess which, if any, is most accurate. Each measurement of photoreceptor arrangement is extracted from an AO image which is assumed to contain little to no distortion. However, in some AO systems, intraframe eye motions can cause subtle distortions which will affect metrics extracted from the image. To address this, an AO Fundus camera was designed, built, and used to validate measurements taken from AOSLOs in aim 2, and is discussed at length in Chapter 6. One of the more salient features of the photoreceptors as visualized through AO ophthalmoscopes is the variability of reflectivity both across a mosaic and over time. Finally, little is understood about the appearance of photoreceptors themselves, though it has been postulated that it may provide an assay of photoreceptor health. Chapter 7 attempts to address that by examining photoreceptor reflectivity in both rods and cones.

Chapter Two: General methodology

Human Subjects

This research followed the tenets of the Declaration of Helsinki, and was approved by the institutional research boards at the Medical College of Wisconsin and Marquette University. Subjects provided informed consent after the nature and possible consequences of these studies were explained. Subjects were recruited from multiple locations: the surroundings of Medical College of Wisconsin, Marquette University, the New York Eye and Ear Infirmary, and Moorfields Eye Hospital. The demographics of each study population will be described within the context of each experiment. Individuals with ocular pathology, ocular opacity, or high myopia or hyperopia (± 10D) were excluded from these studies. Unless otherwise noted, subjects had one eye dilated and accommodation arrested using Phenylephrine Hydrochloride (2.5%) and Tropicamide (1%), respectively.

Imaging the Human Photoreceptor Mosaic

Two AO ophthalmoscopes were used to acquire images of the human photoreceptor mosaic.

Adaptive Optics Scanning Light Ophthalmoscope (AOSLO)

A previously described AOSLO was used extensively throughout this dissertation (**Figure 2.1**) (Dubra & Sulai, 2011; Scoles, Sulai, et al., 2014). Split-detector and confocal AO scanning light ophthalmoscope modalities were acquired simultaneously

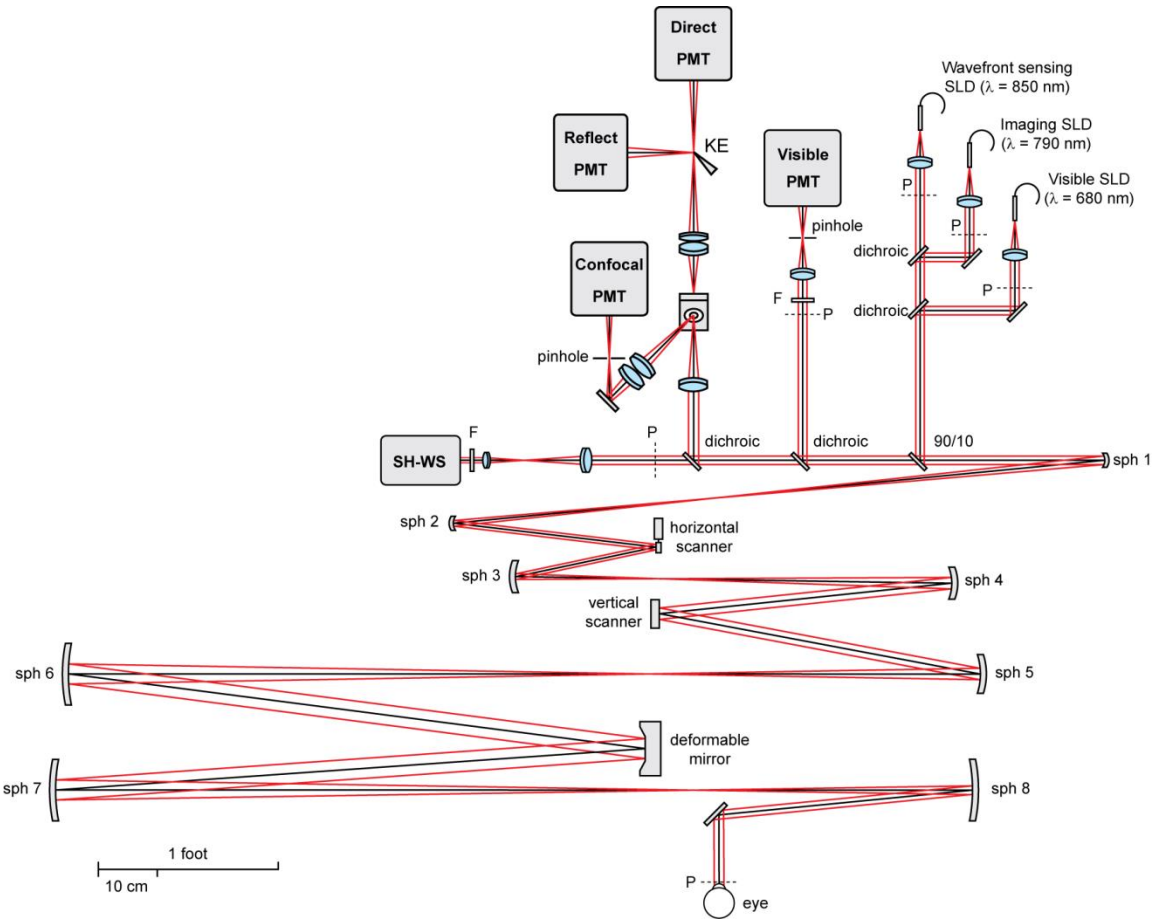

Figure 2.1: The most recent system design of the adaptive optics scanning light ophthalmoscope (AOSLO) used in these studies.

using a 790nm SLD (Superlum, Cork, Ireland). This AOSLO was designed to be capable of multiple of fields of view (FOV), and in the work described herein, 1.0°x1.0° FOV were used for all analyses, with the exception of determining the peak foveal density, which used a smaller 0.75°x0.75° FOV. 1.5°x1.5° FOV images were obtained whenever data was collected for montaging. While the larger FOV did not allow for resolution of foveal cones or rods, it could be used to ensure that images acquired in eccentric sequence (For example: images obtained at 1°, 2°, and 3° from the center of fixation) overlap for montaging.

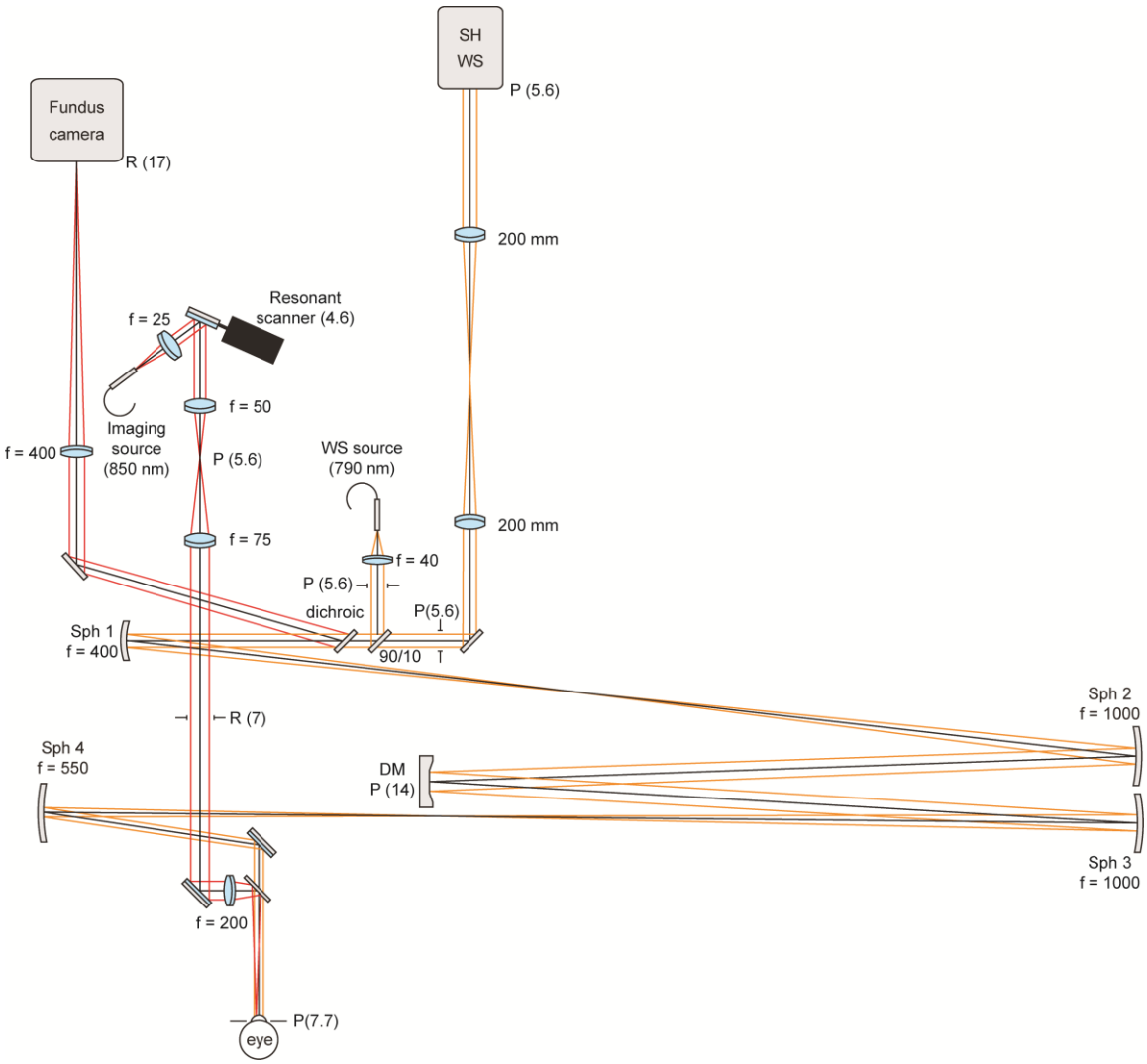

Figure 2.2: The most recent system design of the adaptive optics fundus camera used in these studies.

Adaptive Optics Flood Illumination Ophthalmoscope

An AO fundus camera was constructed for the the work described in Chapter 6 ofin this dissertation (**Figure 2.2**). The AO fundus camera was designed to allow a 2.0° diameter circular imaging beam through a 7.7 mm pupil at the eye. Wavefront sensing was performed with a Shack-Hartmann sensor which consists of a Rolera-XR camera (QImaging, Surrey, British Columbia, Canada) and a 7.8 mm focal length lenslet array arranged in a square lattice with a 203 µm pitch (Adaptive Optics Associates,

Cambridge, Massachusetts, USA). The measured wavefront aberrations are corrected using a Hi-Speed DM97 deformable mirror (ALPAO S.A.S., Biviers, Grenoble, France). The pupil of the eye was relayed to the deformable mirror and Shack-Hartmann using afocal telescopes made of pairs of spherical mirrors (CVI Laser optics, Albuquerque, New Mexico, USA; JML Optical Industries Inc., Rochester, New York, USA). Each afocal telescope was folded off the plane to minimize astigmatism in retinal plane as well as each pupil plane (Dubra & Sulai, 2011; Gómez-Vieyra, Dubra, Malacara-Hernández, & Williams, 2009). We used an 841 nm super luminescent diode (SLD) with a bandwidth of 14.1 nm for wide field retinal illumination and a 790 nm SLD with a 14 nm bandwidth as the wavefront sensing beacon. To reduce the effect of speckle in the illumination path, light from the 841 nm source was scanned on the cornea using a resonant galvanometric optical scanner (Electro-Optical Products Corp., Fresh Meadows, New York, USA). While the previous approaches using multi-modal fibers appeared to reduce speckle effectively (Miller, Williams, Morris, & Liang, 1996), we found that images objectively less speckle using the resonant scanner approach. 841 nm light back-scattered from the central 1.84°x0.8° FOV was focused onto a Sarnoff (SRI International, Menlo Park, California) CAM1M100-SFT 12-bit camera using a 400 mm focal length achromatic lens (Thorlabs, Newton, New Jersey, USA).

Custom capture software was written using C++ in Windows 7 (Microsoft, Redmond, WA). The software was designed to operate as two separate processes communicating via the Qt (Digia, Helsinki, Finland) signals and slots mechanism, and were separately responsible for camera control and framegrabbing. This design was chosen due to a legacy x86-only camera control API and the need for 64-bit addressing space for image capture. A Qt-based graphical user interface (GUI) was created for acquisition and camera control.

AO Image Scaling

Because there are no inter-subject constant distances in the human retina suitable for image calibration, an image of an object of known size must be imaged in order to determine the image scale in μm. As there have been no AO phantoms developed to date, we acquired images of a Ronchi ruling positioned at the focal plane of a lens with a 19mm focal length to determine the conversion between image pixels and degrees. In order to convert to μm on the retina, this conversion needed to be multiplied by the retinal magnification factor (RMF).

A schematic eye, such as the Gullstrand model (Helmholtz, 1866), can be used to determine the micron size of an imaging beam on the retina, thus informing as to the size of any object within the image field and providing the RMF. However, this model includes the six optical surfaces within the eye: the anterior and posterior surfaces of the cornea, anterior lens cortex, and posterior lens cortex. Moreover, it contains empirically observed refractive index changes between each of the six surfaces. While Gullstrand's model is exhaustive in its description of the optics of the eye, it was considered impractical for the purposes of this dissertation to measure each of the six surfaces in a living subject. Li *et al.* (2010) proposed a simplified model, which consisted of four surfaces. These four surfaces were derived from measurements able to be obtained using a non-invasive ocular biometer (Li et al., 2010). However, due to missing corneal curvature data in some subjects, we were unable to use this approach. Therefore, an adjusted axial length method was used to approximate the RMF (Bennett, Rudnicka, & Edgar, 1994). In Bennett's *et al.*'s (2010) model, RMF changes in proportion to the subject's axial length. We compared the Bennet and Li models, and found that the maximum percent difference was 5.4% (**Table 2.1**), with a correspondingly large axial length. However, it is unlikely that high axial length (and high % difference) individuals

Table 2.1: A comparison of the retinal magnification factors (RMF) estimated by Bennet *et al.* and Li *et al.* using data published in Li *et al.*

Axial Length (mm)	*Bennett et al.* RMF (µm/°)	*Li et al. RMF (µm/°)*	% Difference
22.86	277	272	1.8
22.87	277	271	2.4
23.4	284	279	1.8
23.5	285	280	1.6
23.51	285	281	1.3
24.08	292	288	1.2
24.18	293	288	1.6
24.48	297	299	0.6
24.49	297	299	0.6
24.54	298	299	0.5
25	303	306	0.8
25.37	308	311	1.0
25.61	311	317	1.9
25.73	312	320	2.6
26.85	326	336	3.0
27.05	328	342	4.1
27.46	333	349	4.7
28.31	343	362	5.4

would meet the inclusion criteria for these studies, due to the established correlation between axial length and severe myopia (Llorente, Barbero, Cano, Dorronsoro, & Marcos, 2004). Axial length measurements were able to be obtained from all subjects using an IOL Master (Carl Zeiss Meditec, Dublin, CA), and used in combination with Bennett's approach to convert from degrees of visual angle to µm on the retina.

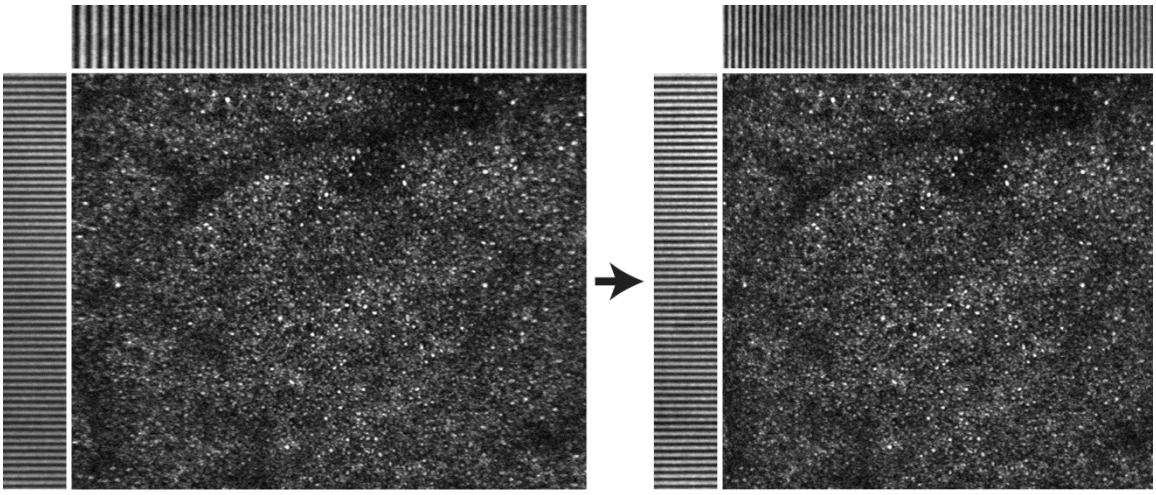

Figure 2.3: The resampling of a distorted AOSLO image (left) using a Ronchi ruling(borders) to an image with equally spaced pixels (right). The minima of the distorted Ronchi ruling (borders, left) were fit to a sinusoid, and a sinc interpolant used created to convert to an image with equally spaced pixels (right). (Images courtesy Drew Scoles)

Image Post-Processing

AOSLO

Post-processing image sequences from the AOSLO consisted of two steps: resonance scanner correction, and image registration. To correct for static intraframe distortions resulting from the sinusoidal motion of the AOSLO's resonant scanner, we estimated the image distortion from images of a stationary Ronchi ruling and then resampled each frame of the raw image sequence over a grid of equally spaced pixels (**Figure 2.3**). After this "desinusoiding", the image sequence could be registered. Registration was performed using a previously described "strip registration" algorithm (Dubra & Harvey, 2010). The algorithm was designed to compensate for the intraframe distortions caused by intraframe eye motion, by dividing each image in an AOSLO sequence in to a set of "strips" (**Figure 2.4**). Each strip is rectangular and oriented along

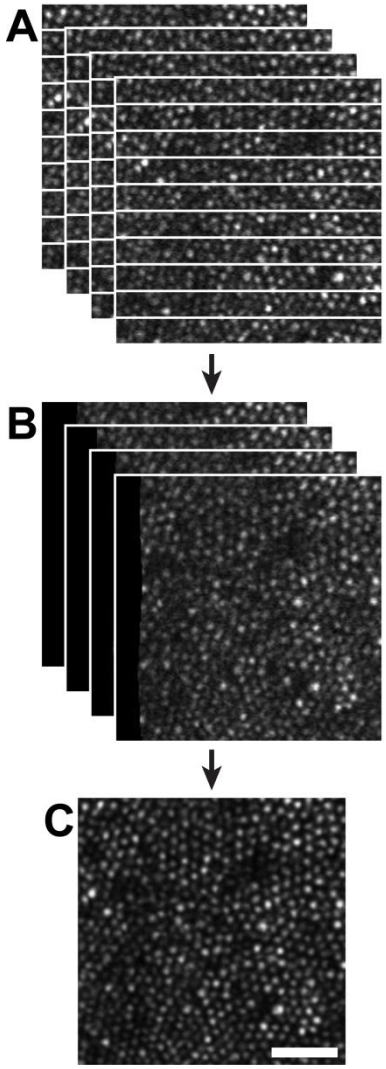

Figure 2.4: The basic steps of strip registration (Dubra & Harvey, 2010). A) First, the each image in the image sequence is divided in to strips. B) Then, each strip is registered to a manually selected reference frame using normalized cross correlation. C) Finally, the strip registered images are averaged together to create a high signal-to-noise ratio image. Scale bar is 25 µm.

the system's resonance scanner orientation. The side of each strip parallel to the resonant scanner orientation is as wide as the image, and the side orthogonal to the scanner orientation can consist of a variable number of pixels, depending on the size of objects within the image. After strip formation, each strip from each image is registered to a manually selected reference frame using modified normalized cross correlation (NCC). Due to the computational intensiveness required to perform NCC, registration is

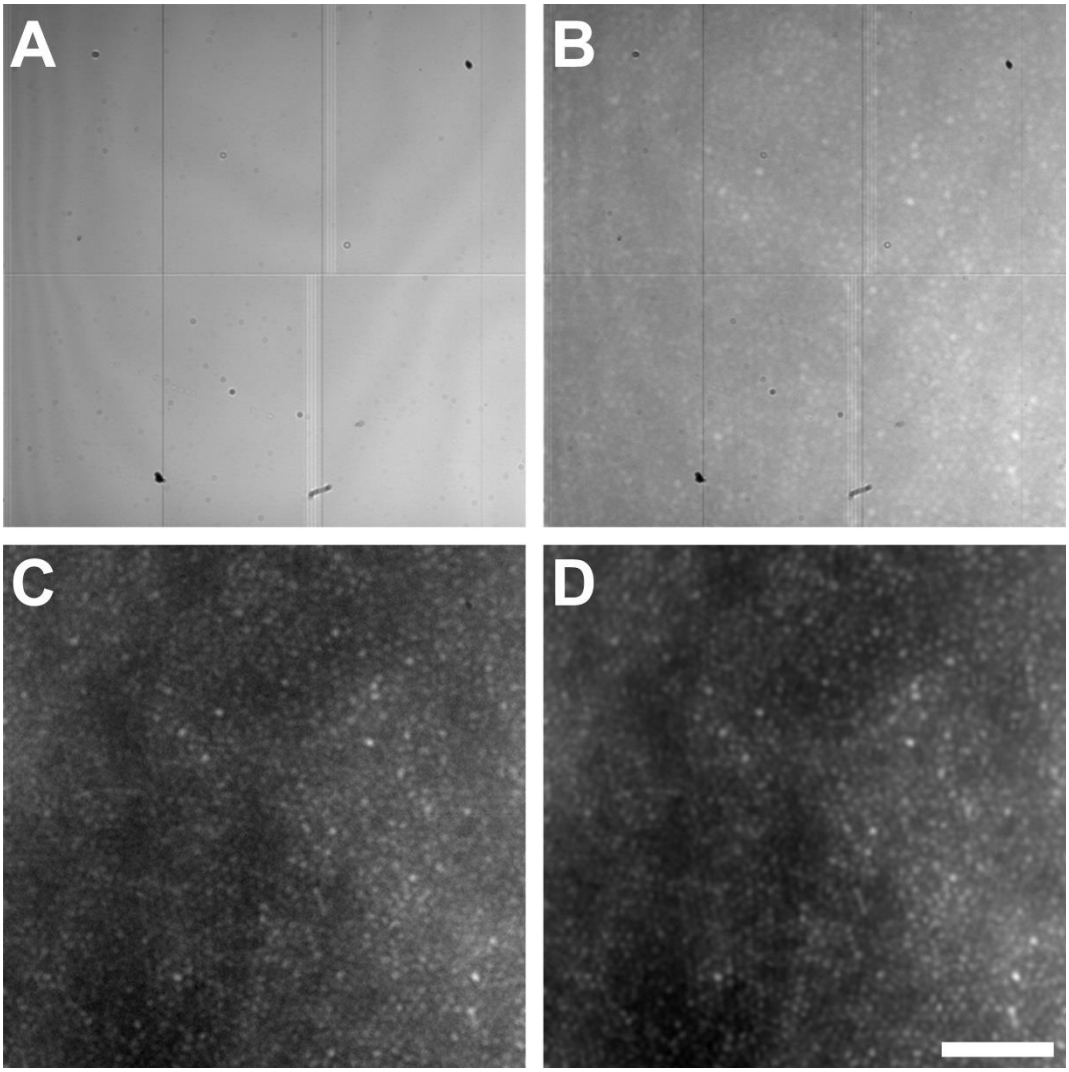

Figure 2.5: The basic steps of AO fundus camera registration. A) A defocused image is acquired to isolate the Sarnoff CCD artifacts. B) Image sequences containing the CCD artifact are acquired from subjects. C) Each image is flat fielded using the defocused image acquired in (A). Finally, each image is registered to a manually selected reference frame using normalized cross correlation. These images are averaged together to create a high signal-to-noise ratio image (D). Scale bar is 50 µm.

performed using general-purpose graphical processing unit APIs (CUDA, Nvidia, Santa Clara, California). Once strip alignments have been attempted for each strip and each image, the strip registered images with the highest NCC values are averaged together, creating an image with an improved signal-to-noise (SNR) ratio.

AO Fundus Camera

Post-processing images from the AO fundus camera consisted of two steps: flat-fielding, and registration. Due to static image artifacts from the back-illuminated Sarnoff charge-coupled device (CCD), and low-frequency image non-uniformities due to non-uniform illumination, each AO fundus image sequence needed to be flat fielded. Flat fielding was performed by first acquiring a defocused image sequence, averaging all frames within the sequence (**Figure 2.5A**). Each subsequent in-focus image (**Figure 2.5B)** was then divided by the averaged, defocused image, to remove the CCD artifacts and reduce non-uniformity (**Figure 2.5C**). Once the image sequences were flat-fielded, they were registered using NCC. Images with low NCC were excluded from the registered sequence. All remaining registered images were then averaged to improve SNR (**Figure 2.5D**).

Cell Identification

Cell locations were determined from confocal AOSLO and AO fundus camera images using a previously described semi-automatic cone identification algorithm (Garrioch et al., 2012; Li & Roorda, 2007). The algorithm was performed as follows: First, the image was filtered using an ideal low-pass filter that reflected the largest possible photoreceptor in an image. Next, the coordinates of all local maxima are determined within the image. The local maxima were binarized and combined using the “close” morphological operation. The centroid of each connected component was used as the cell coordinate. Next, the average nearest neighbor distance was calculated between the extracted coordinates, and that value was used to determine the cutoff of an ideal low-pass filter that reflected the spacing of the cells in the image. The original image was then filtered using the more accurate ideal

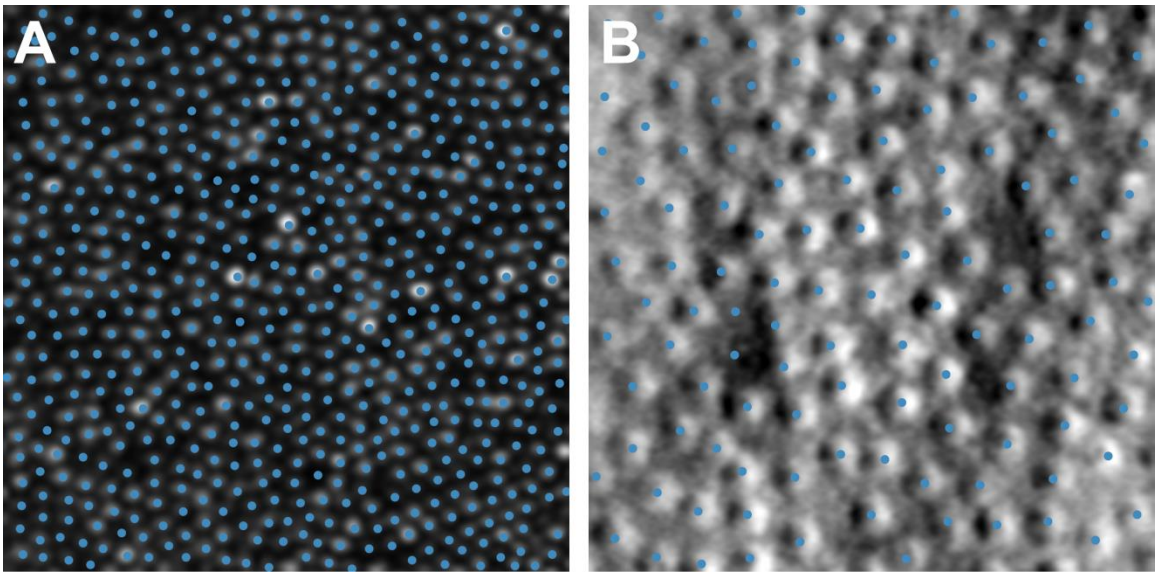

Figure 2.6: A confocal (A) and split-detector (B) image with after cell identification. Cells are semi-automatically identified in confocal images (A) using a previously described approach (Garrioch et al., 2012; Li & Roorda, 2007). Cells are manually identified in split-detector images (B).

low-pass filter. After filtering, binarization, and connected component analysis, the local maxima were again determined, and considered the final location of cells in the image (**Figure 2.6A**). Cone coordinates were manually determined from split-detector AOSLO images (**Figure 2.6B**).

ROI Boundary Effects

All geometrical descriptors extracted from a discrete set of coordinates are subject to boundary effects. Boundary effects are an unavoidable aspect of sampling, and in images of the cone mosaic they are caused by cones positioned around the edge of an ROI. The cells on the edge do not contribute all of their connected neighbors to a spacing measurement, or all the area that they encompass to a density measurement. To mitigate this effect, we used the Voronoi tessellation to establish which cell locations should be included for analysis. A given Voronoi cell that was completely contained within an ROI was considered “bound”, and was thus included in subsequent analyses.

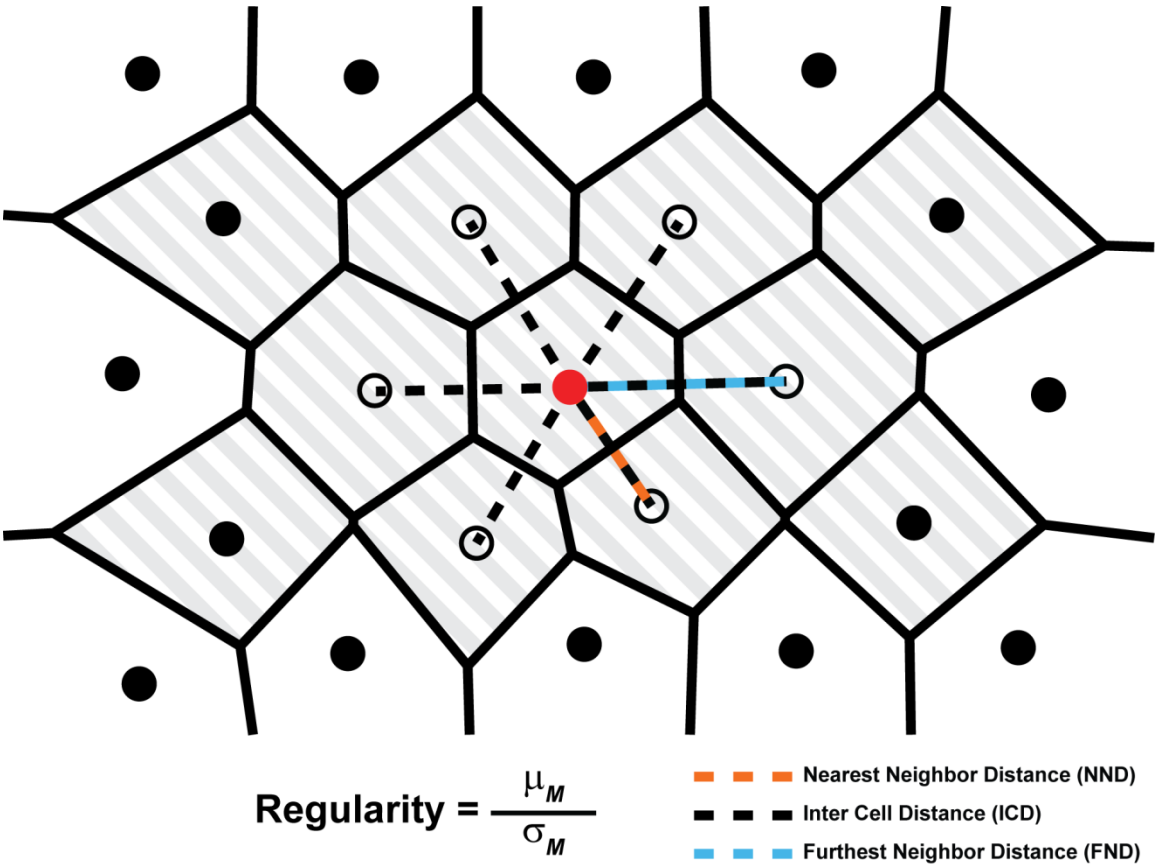

Figure 2.7: A schematic of hexagonally arranged cones illustrating the relationship between distance measurements. NND is defined as the distance of from each cell (red dot) to its closest neighbor (orange dashed line). FND is defined as the distance from each cell to its most distant neighbor (blue dashed line). ICD is defined as the average distance between a cell and all of its neighbors (dashed lines). Regularity was defined as the mean of a metric divided by its standard deviation. In order to mitigate boundary effects, only cells with bound Voronoi regions (striped region) were included when calculating each metric.

All density measurements were calculated with respect to the total area encompassed by all bound Voronoi regions.

Descriptive Metrics of the Cone Mosaic

Cell locations were analyzed using several metrics of cell concentration, spacing, homogeneity, and regularity: density, the density recovery profile distance (DRPD), nearest neighbor distance (NND), inter-cell distance (ICD), furthest neighbor distance (FND), percent six-neighbor Voronoi cells, nearest neighbor regularity (NNR), number of

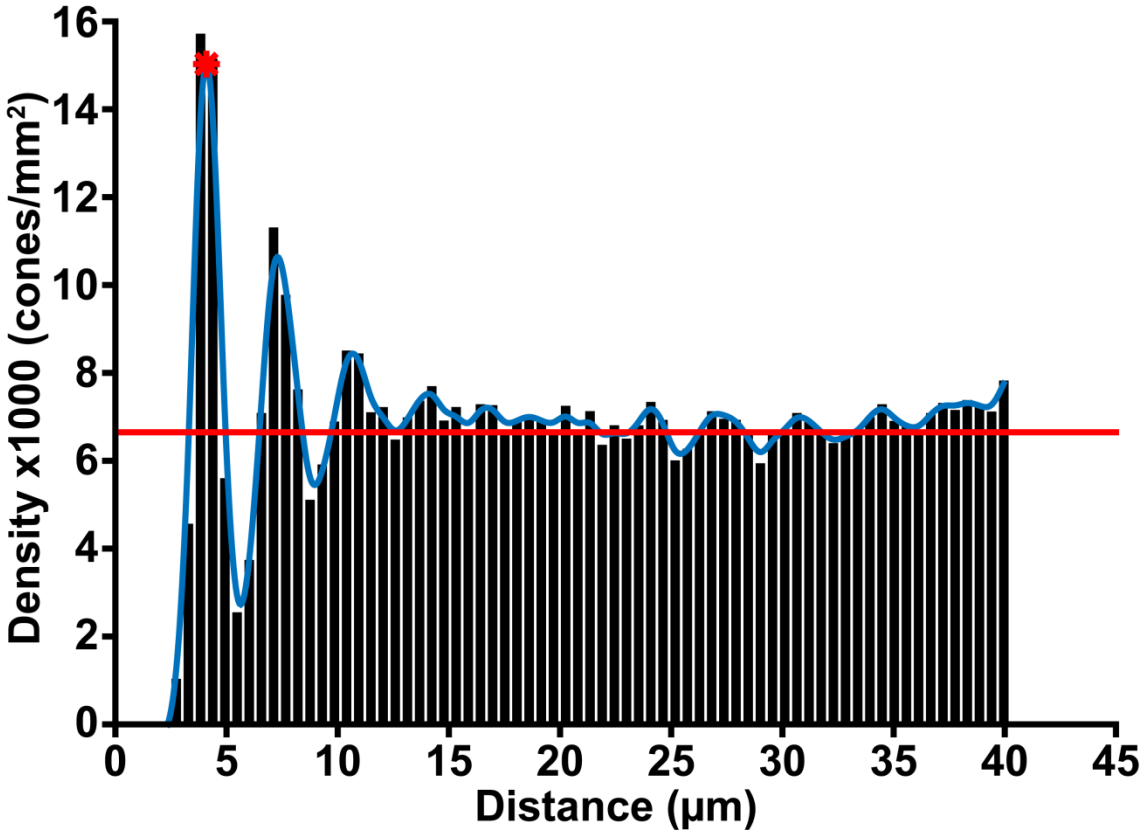

Figure 2.8: The algorithm for automatically determining the DRP distance (DRPD). Once the DRP has been derived using the method outlined by Rodieck, *et al.* (black bars), the peaks of the DRP are fit using a smoothing spline (blue line). DRPD was defined as the first peak of the smoothing spline (red star) which was greater than the average density (red line).

neighbors regularity (NoNR), and Voronoi cell area regularity (VCAR) were extracted from coordinates with bound Voronoi cells.

For each set of cell locations, the Voronoi tessellation was calculated. Density was defined as the ratio of the number of bound Voronoi cells to the amount of area occupied by bound Voronoi cells within an ROI. NND, ICD, and FND measure the average closest, overall, and furthest distances between cells, respectively (**Figure 2.7**). The DRP was used to derive the average spacing within an ROI. The DRP is a method based on a two dimensional autocorrelogram that is an expression of the spatial density of cells as a function of the distance of each cell from all other cells (Rodieck, 1991;

Roorda et al., 2001). To determine spacing from the DRP, we first interpolated between each bin using a 3rd order smoothing spline with equivalent weights. We then found the first local maximum that was greater than the DRP density mean. The x-axis location (distance) of the maximum was used as the DRP-derived spacing, or DRPD (**Figure 2.8**). Voronoi tessellations of cell locations were used to determine the area of each Voronoi cell, as well as the number of six-sided Voronoi cells. Regularity metrics were defined as the mean of a metric divided by its standard deviation. Regularity metrics, as the name implies, allow measurement of the consistency of a particular metric over an ROI. We examined the regularity of nearest neighbor spacing (NNR), Voronoi cell area (VCAR), and number of Voronoi cell neighbors (NoNR).

Chapter Three: Assessing the performance of metrics describing the human cone mosaic

Contributions

These experiments were designed by Dr. Carroll and myself, in collaboration with Dr. Alfredo Dubra, Sergey Tarima (biostatistics), and Melissa Wilk (experimental design). I imaged all subjects within this paper and implemented and performed the analyses. Sergey Tarima performed the statistical tests and designed the classifier tool. I completed the writing and figures in collaboration with Melissa Wilk and Dr. Carroll, with editing assistance from Dr. Dubra and Tarima. I completed image acquisition with the assistance of Phyllis Summerfelt, Christopher S. Langlo, Melissa A. Wilk, Brian Higgins, Erika Phillips, and Dr. Moataz Razeen.

Introduction

Adaptive optics (AO) enhanced imaging devices permit non-invasive visualization of the human retina with cellular resolution. Imaging of the cone (Liang et al., 1997; Miller et al., 2011; Scoles, Sulai, et al., 2014; Williams, 2011; Zhang, 2015), rod (Dubra et al., 2011; Merino et al., 2011; Rossi et al., 2011), and retinal pigment epithelium (RPE) mosaics (Masella et al., 2007; Morgan et al., 2008a; Roorda et al., 2007; Scoles et al., 2013; Torti et al., 2009) has been demonstrated in normal and diseased eyes. While pathology can often be quite striking when imaging with single-cell resolution, the ability to use these images to detect more subtle changes relies on the ability to extract quantitative information about the mosaic of interest. This often involves deriving a descriptive metric of the mosaic, nearly all of which require extracting cell locations within each image. Metrics such as density (Chiu et al., 2013; Chui et al., 2008b; Dees et al., 2011; Flatter et al., 2014; Garrioch et al., 2012; Hansen et al., 2013; Li et al., 2010; Lombardo, Lombardo, et al., 2013; Menghini et al., 2015; Park et al., 2013; Song et al., 2011), cell spacing (Chiu et al., 2013; Duncan et al., 2007; Garrioch et al., 2012; Mkrtchyan et al., 2012; Park et al., 2013; Ratnam, Carroll, Porco, Duncan, & Roorda, 2013; Roorda et al., 2001; Roorda et al., 2002; Roorda et al., 2007; Syed et al., 2013; Yoon et al., 2009), and cell regularity (Baraas et al., 2007; Carroll, Rossi, et al., 2010; Dees et al., 2011; Li & Roorda, 2007; Morgan et al., 2007) are frequently used to assess mosaic integrity. Despite their broad utilization, there has been minimal testing of the ability of these metrics to detect disruptions of the photoreceptor mosaic. Such testing is needed to objectively assess the strengths and weaknesses of these metrics in evaluating retinal mosaics.

One of the more significant factors known to affect the performance of the above metrics is undersampling. Undersampling can come from one of two sources: cell

misidentification and retinal pathology. Algorithms used to identify cells in retinal mosaics have some amount of error (Chiu et al., 2013; Garrioch et al., 2012; Li & Roorda, 2007). As the above metrics typically rely on cell identification rather than the retinal image itself (though see (Cooper, Langlo, Dubra, & Carroll, 2013)), the error introduced by this undersampling is an inherent feature of most current AO analyses. How undersampling affects a given metric provides a direct measure of its robustness. Undersampling can also result from real changes in the retinal mosaic due to pathology (Carroll et al., 2009; Carroll et al., 2004; Choi et al., 2006; Duncan et al., 2007; Hansen et al., 2013). How a metric changes in response to known amounts of pathology defines its sensitivity. As there are a wide range of metrics used to assess retinal mosaics, it is critical to characterize how each metric is affected by undersampling. An ideal metric should be sensitive enough to detect pathology, but robust enough to not be affected by small errors in cell identification.

Due in part to the optical waveguide properties of photoreceptors, the cone mosaic can be imaged with particular ease. In fact, the cone mosaic can be imaged in some individuals even without using AO (Larocca, Nankivil, Farsiu, & Izatt, 2013; Miller et al., 1996; Wade & Fitzke, 1998; Wolsley, Saunders, Silvestri, & Anderson, 2010). Moreover, cone photoreceptors drive the majority of our visual function and are affected in a variety of retinal diseases. Thus there is continued interest in the development and validation of metrics for detecting disruptions of the cone mosaic. Here we examined the performance of a series of descriptive metrics, including many that have been previously illustrated. Specifically, we applied known amounts of undersampling to real photoreceptor coordinates derived from images of the human cone mosaic acquired at various retinal eccentricities. This has been observed in conditions such as inherited retinal degenerations (Carroll et al., 2004; Choi et al., 2006; Duncan et al., 2007) and acute macular neuroretinopathy (Hansen et al., 2013). In addition, this type of

undersampling approximates the expected pattern that might occur as a result of errors in cell selection. We observed significant variability in the sensitivity of the different metrics to undersampling. The data presented here provide a useful framework for understanding the strengths and limitations of these metrics, and highlight the important "philosophical" issue of whether the insensitivity (or robustness) of a metric represents a strength or a weakness when trying to determine whether a given cone mosaic is normal or abnormal.

Methods

Human Subjects

This research followed the tenets of the Declaration of Helsinki, and was approved by the institutional research boards at the Medical College of Wisconsin and Marquette University. Twenty subjects with normal trichromatic vision were recruited for this study (**Table 3.1**). Subjects provided informed consent after the nature and possible consequences of the study were explained. Individuals with high myopia or hyperopia (± 10D) were excluded from this study. Axial length measurements were obtained on all subjects using an IOL Master (Carl Zeiss Meditec, Dublin, CA), and used in combination with a simplified Gullstrand II model to convert from degrees of visual angle to μm on the retina.

Imaging the Human Photoreceptor Mosaic

Confocal (Dubra & Sulai, 2011) and split-detector (Scoles, Sulai, et al., 2014) AOSLO modalities were used to simultaneously image the photoreceptor mosaic along the temporal, inferior, nasal, and superior meridians using a 790nm superluminescent diode. Using a 1.0° field of view (FOV), each meridian was sampled every half degree from fixation out to 6°, and then every degree from 7° to 10°. Using a 1.5° FOV, each

Table 3.1: Subject demographics.

Subject ID	DOB	Age	Refraction	BCVA	Eye	Axial Length (mm)
AD_10252	10/26/1988	26	-5.75 +1.00x55	20/13 -2	OS	26.73
AD_10253	12/21/1988	26	-4.25 +0.75x90	20/13	OS	25.27
JC_0200	5/29/1987	28	-3.00 +0.25x80	20/13 -1	OS	24.72
JC_0677	9/12/1988	26	-1.25	20/10 -1	OS	24.01
JC_0878	3/6/2006	9	-0.25 +0.25x182	20/20	OD	23.36
JC_0905	2/18/1992	23	+1.00 +1.00x49	20/20	OS	21.98
JC_10119	11/11/1991	23	-3.75 +0.75x84	20/16 +1	OD	25.9
JC_10121	7/27/1991	24	0.50 +0.25x76	20/13 +2	OS	23.93
JC_10122	6/9/1988	27	plano	20/13 -1	OD	23.42
JC_10145	6/7/1965	50	-2.75 +0.25x16	20/16 +4	OD	24.66
JC_10147	8/3/2001	14	-1.5	20/16 +1	OS	24.67
JC_10220	3/30/1990	25	1.75 +1.75x170	20/13 +1	OS	22.35
JC_10304	4/8/2004	11	-.00 +0.50x107	20/16 -1	OD	24.12
JC_10311	7/9/1952	63	+1.00 +0.25x25	20/20-1	OD	22.86
JC_10312	6/11/1999	16	-6.00 +1.50x70	20/16	OS	26.88
JC_10316	1/11/2001	14	-0.50 +0.50x0	20/20 +3	OS	24.59
JC_10317	1/11/2001	14	-0.50	20/16 +1	OS	24.56
JC_10318	1/11/2001	14	-0.75 +0.50x10	20/16 +2	OS	25.06
JC_10329	3/29/1992	23	-0.75 +1.00x175	20/13 +2	OS	24.46
JG_10182	5/6/1948	67	+0.50 +0.25x120	20/20	OS	24.15

meridian was sampled every degree from fixation out to 10°. To correct for static intraframe distortions within the raw image sequences resulting from the sinusoidal motion of the resonant optical scanner, we estimated the distortion from images of a stationary Ronchi ruling and then resampled each frame of the raw image sequence over a grid of equally spaced pixels. After this “desinusoiding”, a reference frame was selected manually from within each image sequence for subsequent registration using custom software (Dubra & Harvey, 2010). Montages of overlapping split-detector and confocal images using both 1.0 and 1.5° FOVs were created semi-automatically using custom software. To simply the process of montaging, custom software was created in

MATLAB (Mathworks, Natick, MA) that allows the user to rapidly screen which images should be included in a montage. After screening the images, they were automatically placed in a corresponding Photoshop (Adobe, San Jose, CA) file at a location extracted from the digitized image acquisition notes. Once the montage was “seeded” using the above software, the user manually aligned the images within Photoshop to achieve a more accurate alignment.

Sampling the Cone Photoreceptor Mosaic

Because foveal cones could not be reliably resolved in all subjects, the location of peak foveal density was determined using a previously described method (Putnam et al., 2005). First, cone coordinates were semi-automatically identified from a foveal montage using a previously described cell identification algorithm (Garrioch et al., 2012). Density maps were generated from the resulting coordinates. Six contours (at 80 to 93% of the peak cone density) were derived from each density map, and the center of each contour was averaged to provide an estimate of the location of peak foveal cone density.

Regions of interest (ROIs) were then extracted from each montage, relative to the location of peak foveal cone density, using custom software (Adobe, San Jose, CA and Mathworks, Natick, MA). The size of each ROI varied as a function of eccentricity. To determine the size for each ROI, we used previously published AOSLO-derived cone density data (Wilk et al., 2014) to estimate the area necessary to encompass approximately 100 cones at each eccentricity. Using the minimum observed foveal density in that study (84,000 cones/mm^2), we set the area of ROIs at the location of peak foveal cone density to 37x37 μm. Due to the minimal change in cone density beyond 10°, we set the area of ROIs at and beyond 10° to 100x100 μm. We next fit an exponential function to these areas, establishing an eccentricity-to-ROI area relationship. We obtained ROIs at the foveal center, every 50 μm from 50 to 600 μm eccentricity,

every 200 μm from 600 to 1600 μm eccentricity, and every 300 μm from 1600 to 3100 μm eccentricity. Within 500 μm of peak foveal cone density, ROIs were extracted from the confocal modality, while beyond 500 μm ROIs were extracted from the split-detector modality due to superior cone contrast. When either blood vessels or seams between overlapping images occurred at a desired ROI sampling location, we adjusted the ROI's location to a nearby unobstructed area. To enable easier comparison at a sample eccentricity, each ROI was binned based on the nearest sample location. ROIs within an eccentricity bin were then compared across all subjects. On average, the ROIs deviated from their bin location by 4.7 μm within 600 μm of the foveal center, and 67.4 μm beyond 600 μm from the foveal center. Cone coordinates were then semi-automatically identified within each confocal ROI (Garrioch et al., 2012), and manually identified within each split-detector ROI using custom software by a single observer (R.F Cooper).

Descriptive Metrics of the Cone Mosaic

Cell locations were analyzed using several metrics of cone prevalence described in chapter two: spacing, and regularity: density, the density recovery profile distance (DRPD), nearest neighbor distance (NND), inter-cell distance (ICD), furthest neighbor distance (FND), percent six-neighbor Voronoi cells, nearest neighbor regularity (NNR), number-of-neighbors regularity (NoNR), and Voronoi cell area regularity (VCAR) were extracted from coordinates with bound Voronoi cells.

Examining the Sensitivity of Metrics to Undersampling

To determine the sensitivity of each metric to cell undersampling, cone locations from all subjects were analyzed using the metrics described above. The data were transformed to establish a polynomial relationship: eccentricity values were transformed according to the equation

$$E_t = \frac{1}{1+E_{\mu m}} \quad \textbf{(Eq. 3.1)}$$

where $\mathrm{E}_{\mu\mathrm{m}}$ is eccentricity in μm, and E_{t} is the transformed eccentricity value. All metric outputs (M) were transformed using a natural log ($\log(\mathrm{M}) = \mathrm{M}_{\log}$). Polynomial regressions (order range:1^{st}-4^{th}) were performed to model the relationship between different metric values ($\mathrm{M}_{\log}$) and eccentricity (E_{t}). To determine the threshold at which a metric could sensitively detect an abnormal mosaic, we created a prediction ellipse from the mean coefficients of each metric's regression and simulated cone undersampling within each ROI. We then generated an abnormal detection rate curve (statistical power curve) for each metric. We did this by randomly selecting a subject, then simulating cone loss in all of that subject's cone coordinates by randomly removing 5-80% of cone coordinates from each ROI. We then performed a polynomial regression on metrics derived from the "disrupted" mosaic loss and used Hotelling's T-squared statistic to determine when the fit coefficients were significantly different than the ellipsoid for any given metric. This process was repeated in 1,000 trials for each cone loss amount. A metric was considered sensitive to loss when it correctly identified abnormal mosaics in 80% of trials. Finally, at each eccentricity, we constructed 95% pointwise prediction intervals (PIs) for each of the above metrics to allow pairwise comparisons.

Table 3.2: Cone mosaic metrics as a function of eccentricity.

Eccentricity Bin (μm)	Density (cones/mm^2)	NND (μm)	DRPD (μm)	ICD (μm)	FND (μm)	% Six Sided	VCAR	NoNR	NNR
0	118,680±23,290	2.43±0.244	3.10±0.367	3.15±0.380	3.98±0.529	54.8±10.9	3.70±1.07	7.88±1.40	8.37±1.38
50	114,390±20,154	2.56±0.233	3.28±0.340	3.27±0.321	4.06±0.453	62.9±12.2	6.16±0.851	9.39±2.32	8.35±1.14
100	103,978±16,996	2.69±0.241	3.50±0.345	3.41±0.308	4.19±0.422	69.0±10.2	6.57±1.04	10.4±2.06	8.57±1.30
150	87,629±13,435	2.94±0.193	3.82±0.289	3.71±0.314	4.50±0.429	70.9±9.56	7.13±1.22	10.9±2.02	8.98±1.46
200	75,405±10,657	3.20±0.181	4.08±0.258	3.98±0.285	4.81±0.377	71.2±8.99	7.68±1.23	11.1±1.95	9.41±1.41
250	65,850±9,407	3.38±0.202	4.33±0.270	4.27±0.301	5.17±0.395	67.4±9.47	7.85±1.35	10.3±1.85	9.56±1.54
300	58,431±9,390	3.57±0.216	4.55±0.290	4.54±0.375	5.55±0.515	64.4±9.73	7.88±1.50	9.84±1.68	9.55±1.65
350	52,172±9,302	3.78±0.334	4.73±0.315	4.83±0.470	5.93±0.651	61.5±9.00	7.90±1.65	9.32±1.45	9.71±1.79
400	46,200±9,931	3.92±0.288	4.94±0.390	5.17±0.648	6.29±0.652	58.0±8.38	7.76±1.85	8.82±1.35	9.48±2.14
450	42,661±10,109	4.20±0.427	5.01±0.379	5.39±0.645	6.58±0.627	57.2±7.28	7.56±1.69	8.60±1.08	9.51±2.09
500	38,914±6,625	4.39±0.333	5.17±0.333	5.59±0.488	6.97±0.679	54.8±5.75	7.25±1.59	8.29±0.842	9.10±2.12
550	34,745±8,446	4.54±0.473	5.36±0.545	5.88±0.644	7.35±0.830	52.9±6.08	6.92±1.69	7.92±0.884	8.59±2.05
600	31,516±8,092	4.72±0.464	5.50±0.553	6.15±0.636	7.72±0.832	52.5±6.10	7.00±1.79	7.95±0.839	8.55±2.22
800	24,194±5,859	5.46±0.709	6.40±0.964	7.18±0.899	9.01±1.21	51.8±6.55	6.93±1.60	7.85±0.818	7.64±1.63
1000	20,104±5,110	5.98±0.780	7.15±1.21	7.85±0.925	9.85±1.22	52.6±6.56	6.96±1.45	7.92±0.946	7.59±1.21
1200	16,381±3,143	6.60±0.703	7.82±1.27	8.61±0.781	10.7±1.02	54.5±6.09	7.18±1.44	8.08±0.896	7.86±1.32
1400	15,074±2,454	6.87±0.599	8.31±1.05	8.95±0.759	11.2±1.09	54.1±5.85	7.45±1.43	8.11±0.843	7.87±1.23
1600	13,148±2,079	7.35±0.56	9.09±0.860	9.56±0.778	12.0±1.14	53.2±6.64	7.52±1.56	7.96±0.84	8.33±1.27
1900	11,883±1,955	7.73±0.60	9.38±0.889	10.1±0.882	12.6±1.40	53.4±7.10	7.59±1.48	8.05±0.89	8.30±1.21
2200	10,429±1,606	8.19±0.56	10.1±1.00	10.7±0.791	13.4±1.15	50.9±7.32	7.62±1.60	7.80±0.74	8.20±1.20
2500	9,569±1,392	8.48±0.60	10.5±1.11	11.2±0.797	14.0±1.11	50.3±7.19	7.46±1.50	7.56±0.89	8.02±1.21
2800	8,783±1,284	8.83±0.59	11.0±1.12	11.6±0.804	14.6±1.18	49.0±8.52	7.27±1.35	7.53±0.94	7.72±1.10
3100	7,955±1,308	9.21±0.68	11.4±1.39	12.2±1.02	15.4±1.59	48.6±7.65	7.02±1.50	7.42±0.92	7.64±1.10

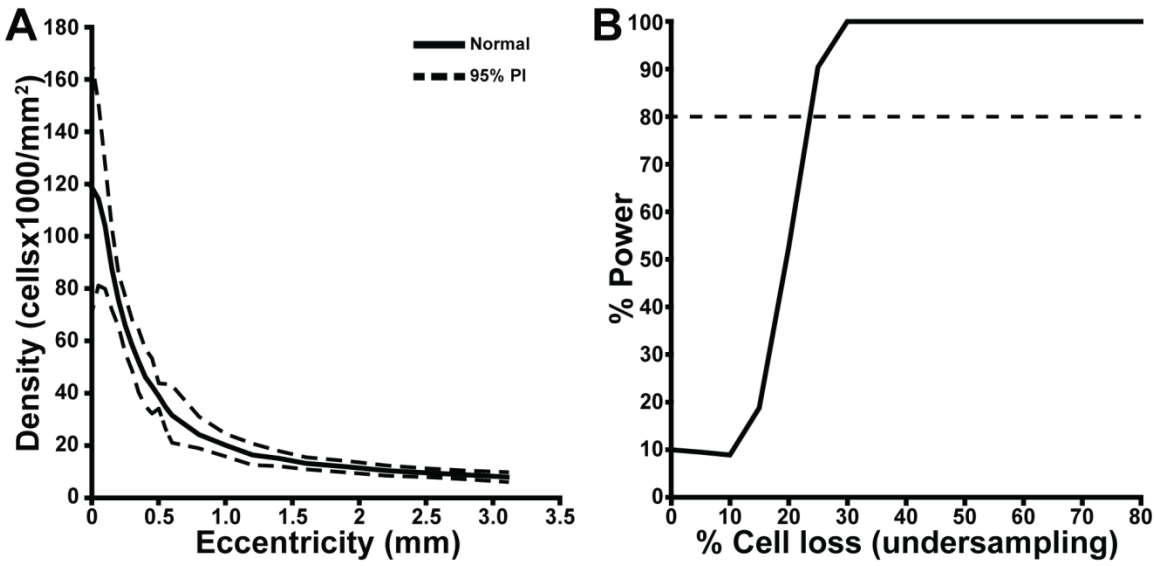

Figure 3.1: The mean of all 20 subjects' density as a function of eccentricity (A), and their associated statistical power curves (B). In (A), the solid line represents the mean of all 20 subjects' density, with the 95% prediction intervals (95% PI) shown as dashed lines. B) Density's statistical power curve (solid line) does not reach the 80% threshold (dashed line) until over a 20% cone undersampling, implying that density cannot reliably detect an abnormal cone density until greater than 20% of the cells have been removed from a subjects' cone mosaic.

Results

We were able to obtain images from all 20 subjects across each eccentricity. The numerical results are summarized in **Table 3.2**. **Figure 3.1A** illustrates the expected exponential decrease of cone density with eccentricity in our data (Curcio et al., 1990; Dees et al., 2011; Lombardo, Lombardo, et al., 2013; Wilk et al., 2014), and its 95% PI. The PI appears larger near the foveal center due to the increased normal variability in foveal cone density. In contrast, all types of cone spacing increased monotonically as a function of eccentricity (**Figure 3.2**). Each 95% PI was smaller near the fovea (<500 μm) and larger in the perifovea. Metrics of regularity tended to follow previously observed patterns for regularity in the retina (Baraas et al., 2007; Carroll, Rossi, et al., 2010; Dees et al., 2011; Li & Roorda, 2007; Morgan et al., 2007); all regularity metrics were low in

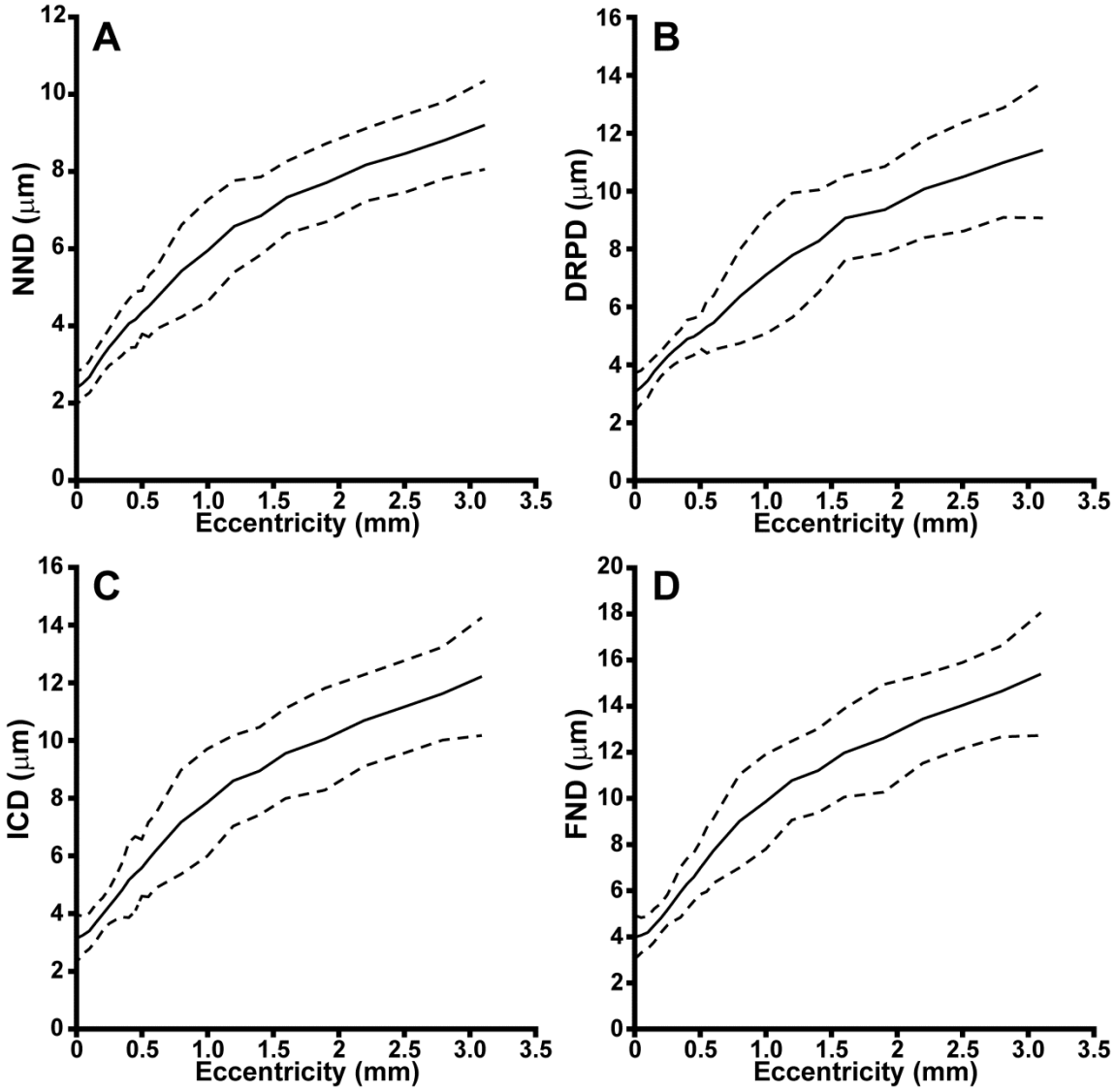

Figure 3.2: Mean population cone spacing measurements. (A-D) Four different spacing measurements (NND, DRPD, ICD, FND) are plotted as a function of eccentricity (solid lines) with their respective 95% prediction intervals (dashed lines). All four spacing metrics increased monotonically towards the parafoveal region.

the foveal center and reached their maximum at about 250 μm (**Figure 3.3**). Percent six-sided and NoNR decreased after 250 μm (**Figure 3.3 A,C**). However, VCAR and NNR exhibited more complex behavior (**Figure 3.3 B,D**). Both metrics peaked at about 250 μm, dropped at 500 μm, peaked again at 1000 μm, and decreased again with increasing eccentricity.

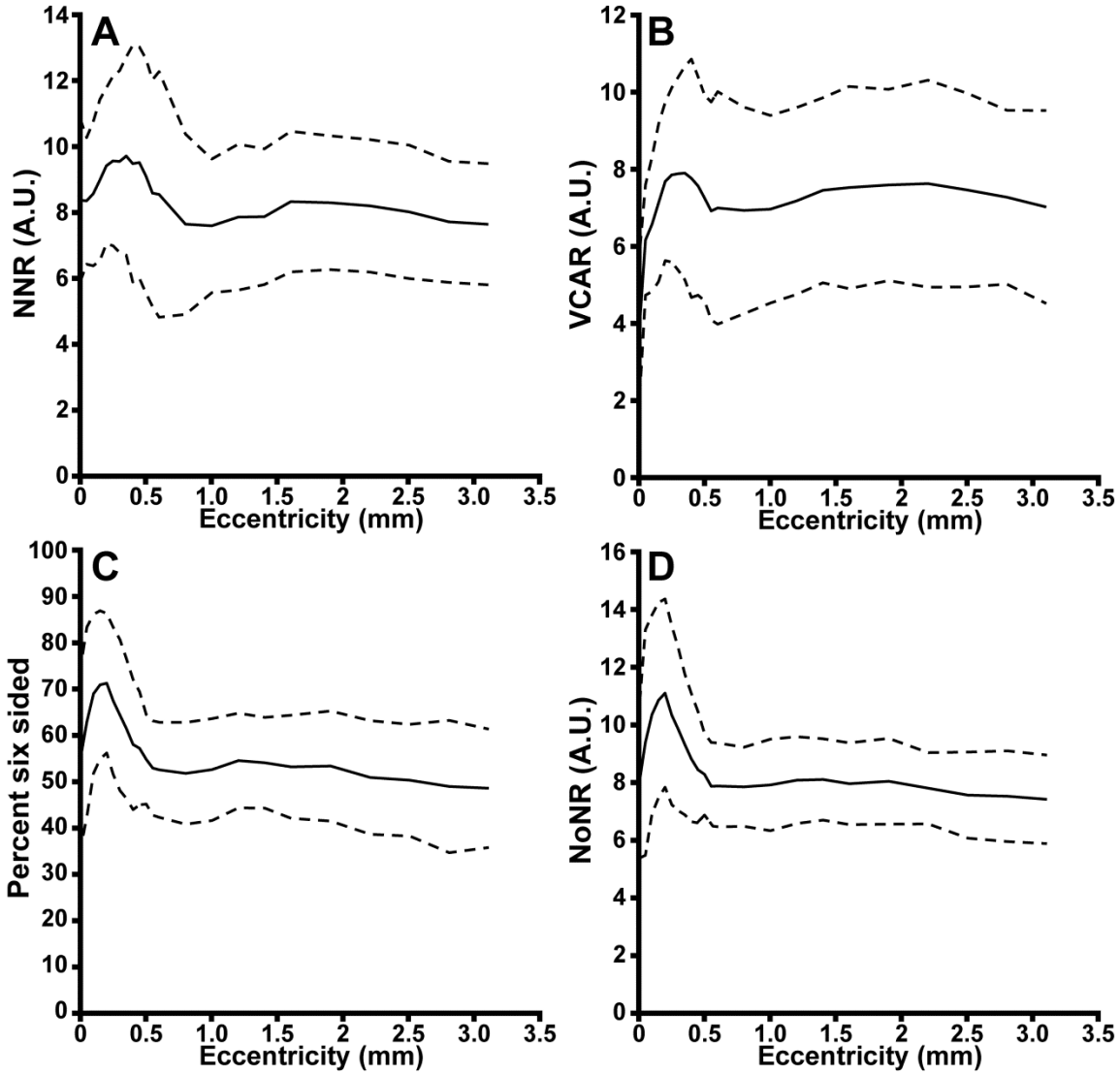

Figure 3.3: Mean population regularity measurements. (A-D) Four different regularity measurements (NNR, VCAR, percent six-sided cells, NoNR) are plotted as a function of eccentricity (solid lines) with their respective 95% prediction intervals (dashed lines). All four regularity metrics exhibited increased regularity in the parafoveal region with a drop in regularity at the foveal center.

To characterize how each metric was affected by undersampling, we first applied undersampling to a single ROI that exhibited near-average metric values (JC_10145, 200 μm eccentricity). **Figure 3.4** illustrates the effect of 40% and 80% undersampling on this ROI. Qualitatively, the uniformity of the mosaic decreases substantially with each type of loss. However, without *a priori* eccentricity information, the ROI could simply be

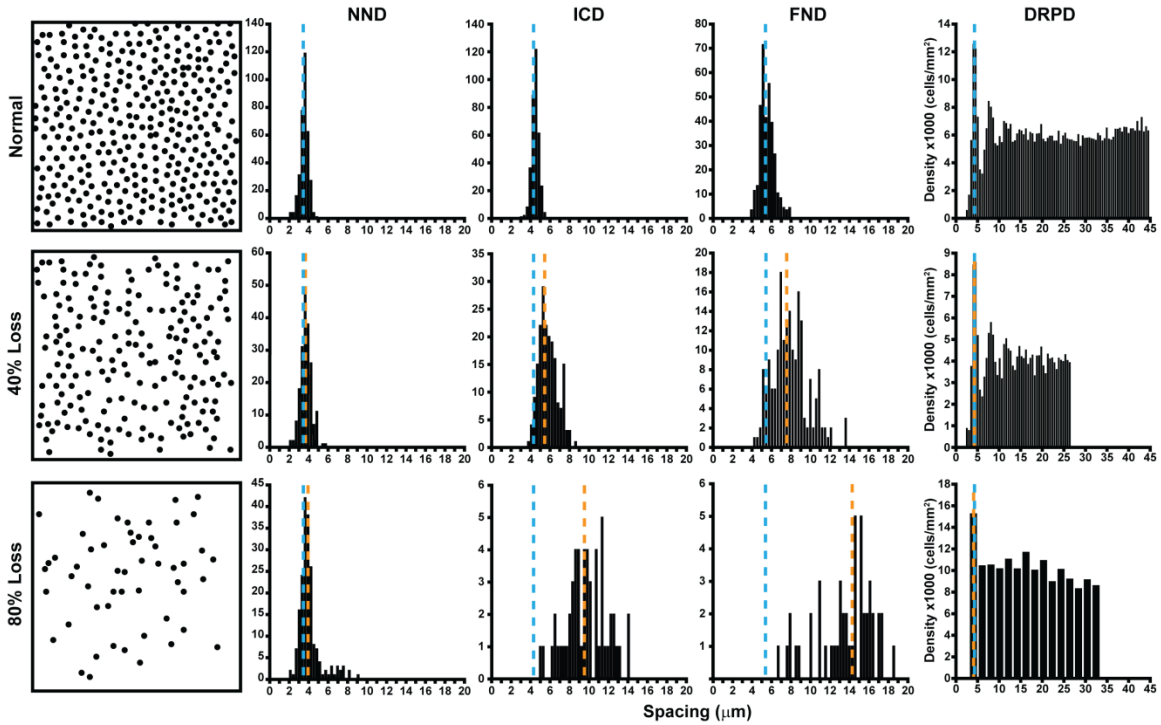

Figure 3.4: An illustration of the effect of cone undersampling on histograms of cell distances (NND, ICD, FND) and the DRP from a single subject (JC_10145, 200 μm eccentricity). The blue dashed line is the 0% loss histogram mean, and the orange dashed line is the mean of the 40% loss (middle row) and the 80% loss (bottom row) histograms. The Y-axis is the number of cells within each histogram bin. The NND histogram is only marginally affected, even with an 80% loss. Similarly, the DRPD is largely unaffected by cell loss; its estimated spacing is only affected when the bin size increases (bottom right) due to a decrease in density. In contrast, the means and spreads of both ICD and FND increase substantially with cell loss.

from a location more distant to the fovea. The histograms of each type of spacing appear different; NND remains tightly clustered about the mean, whereas the mean and spread of ICD and FND measurements change as increasing amounts of loss are applied. In the DRP, the mean only slightly changes; in fact, the estimated spacing decreased, though this is likely an artifact due to the bin size selection algorithm. All measurements of regularity for this ROI decreased in response to undersampling (**Figure 3.5**). The percentage of six-sided cells decreased by a similar amount (by 39% between 0 and 40% undersampling, by 40% between 40 and 80% undersampling) between each percent undersampling. NoNR decreased by 47% between 0 and 40%

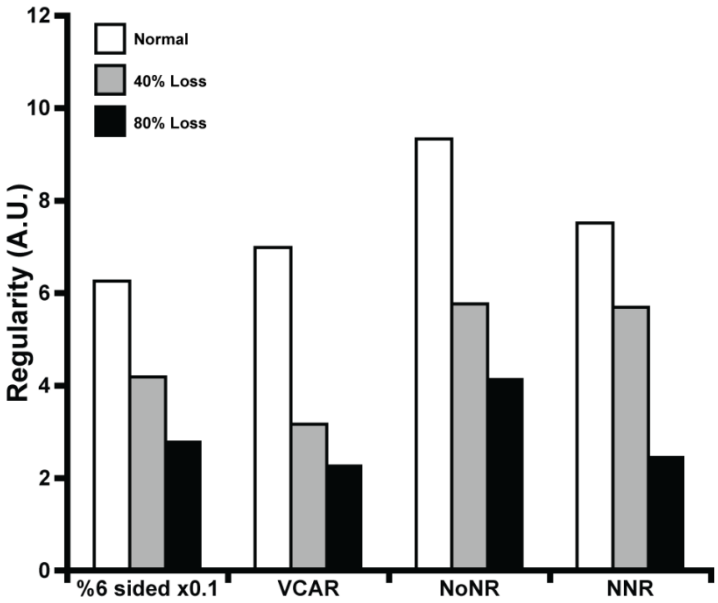

Figure 3.5: The effect of cone undersampling on measurements of regularity (percent six sided cells, VCAR, NoNR, NNR) in a single ROI. The measured regularity (0% loss) is represented by white bars. Cone loss of 40% (grey bars) and 80% (black bars) results in a reduction in regularity for all four metrics, though each metric decreases at different rates. Note that percent six sided cells has been divided by 10 to fit the scale.

undersampling, and 32% between 40 and 80% undersampling. Interestingly, VCAR decreased by 75% between 0 and 40% undersampling, and roughly half that (31%) between 40 and 80% undersampling, implying that the metric changes more with lower amounts of loss. NNR was the opposite, decreasing only 27% between 0 and 40% undersampling, but substantially more (79%) between 40 and 80%.

We then used the classifier described above to examine each metric's ability to detect undersampling in simulations from all 20 subjects. Density did not reliably detect an abnormality until 24% of the cones had been removed across all eccentricities (**Figure 3.1B**). The NND and DRPD were remarkably insensitive to undersampling; an abnormal mosaic was unable to be detected in either metric until 53%and 55% of cone coordinates were removed, respectively (**Figure 3.6**). In contrast, ICD and FND were able to detect an abnormal mosaic at a 29% and 23% cone loss, respectively (**Figure 3.6**). Of the regularity metrics, NNR was the least sensitive, and detected abnormality

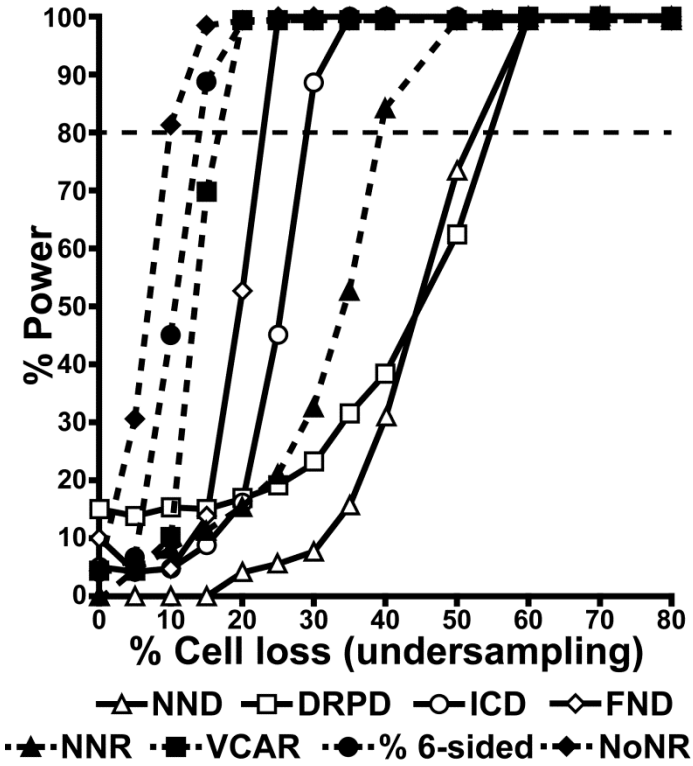

Figure 3.6: Statistical power curves (*solid lines*) for spacing and regularity measurements as a function of the amount of undersampling (i.e., cell loss). The sensitivity of a given regularity measurement was defined as the point at which the statistical power curve crossed 80% power (*horizontal dashed line*). Mean NND and DRPD are insensitive to cone undersampling and are only able to reliably detect a cell loss of 53%and 55% of cone coordinates were removed, respectively. Mean ICD can reliably detect that the cone mosaic is abnormal after a 29% cone undersampling. Mean FND is the most sensitive of the four spacing metrics and is able to detect an abnormal mosaic after 23% cell loss. Mean NNR was relatively insensitive and was unable to detect an abnormal mosaic until a 40% undersampling. Percent six-sided cells and VCAR were able to detect abnormal mosaics with 17% and 14% undersampling, respectively. Mean NoNR was the most sensitive, detecting abnormal mosaics at 10% undersampling.

with above 35% (**Figure 3.6**). The VCAR and percentage of six sided cells and were similarly sensitive and were able to consistently detect a deviation from normal beyond a 17% and 14% loss, respectively (**Figure 3.6**). Of the regularity metrics, NoNR was the most sensitive, and was able to detect an abnormal mosaic at only a 10% loss (**Figure 3.6**).

Discussion

We characterized the normal cone mosaic as a function of eccentricity using a variety of metrics, including some that have been previously described. Our data demonstrate that different metrics have different 95% PI widths, and different metrics respond more sensitively than others. NND, DRPD, and NNR were the least sensitive to cone undersampling, whereas percentage of six sided Voronoi cells, VCAR, and NoNR were the most sensitive. Intuitively, one might think that the most sensitive metrics should always be used; however, there are some important limitations to this study that should be reviewed to provide context to these results.

The pointwise PIs constructed here represent the range that single future metric values will fall with 95% likelihood. For each metric's PI, we aggregated the results from all meridians to construct the PI. This assumes that the metrics measured along each meridian (Temporal, Inferior, Nasal, and Superior) behave similarly, which may not always hold. Moreover, the PIs for each metric presented here are constructed from our 20 subjects, which, assuming our 20 normal subjects are representative of the true variability in the population, make the actual estimate of the PI more conservative than it would be if we had included a larger population. In contrast, the classifier tools were constructed for each metric to classify all ROIs from a single subject as either abnormal or normal. However, these classifiers were based off of multiple regressions of our data. While density and spacing metrics fit predefined models, the unusual shape of the regularity metrics required higher-order (4^{th}) polynomials in order to fit closely. While on average subjects had R^2 goodness-of-fit values above 0.8, without an ideal regression model our classifier may underestimate the true amount of variability (covariance) from regularity metrics across all subjects.

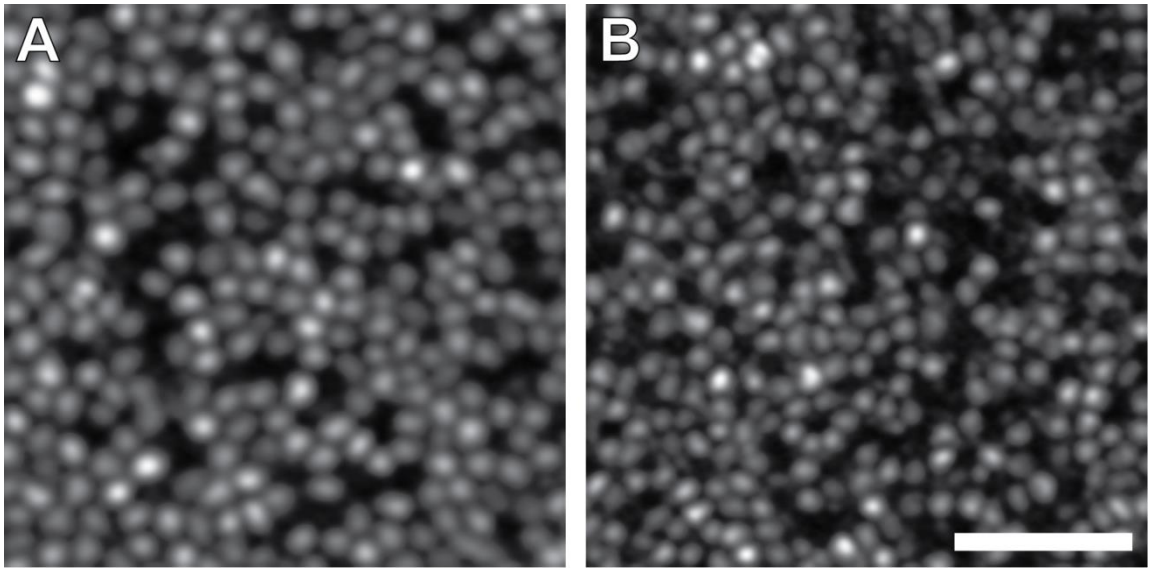

Figure 3.7: An example of a subject with a diffuse cone loss (Carroll et al., 2004). We analyzed a mosaic with non-reflective cones at two locations: (A) 200 µm and (B) 350µm, paralleling the undersampling simulations performed here. For both locations, both density and ICD were consistent with a 48% cell loss (undersampling). However, NND and DRPD were consistent with a greater than 70% cell loss, and VCAR, NoNR, and percent six sided were consistent with only a 20% cell loss at the same location.

While this study finely sampled all four meridians, the samples were extracted from only 20 subjects. This sample size can cause a number of artifacts when constructing the statistical power curves. The classifier which generates the power curves is constructed from the normal data with no loss; thus, the classifier should correctly identify normal mosaics at a rate similar to the significance level of 95%, or statistical power of 5%. From the baseline of 5%, the statistical power should monotonically increase with increased cone loss; however, that was not always the case. For example, in density's statistical power curve (**Figure 3.1**), the power decreases from a value of 10% at a 0% loss to 8.8% at a 10% undersampling. These types of artifacts could be surmounted by the inclusion of more subjects; however, due to the substantial quantity of processing and analysis overhead needed to obtain these results, more work in the automation of both pre-processing and ROI extraction is

needed before acquisition of data from larger subject population is practical. Moreover, because these statistical power curves are constructed from a smaller population, the % cone loss at which they could reliably detect an abnormal subject may be worse than what would be seen with a larger subject pool.

A different issue relates to the type of cone loss that was adopted for these analyses. Photoreceptor loss is a dynamic process; when cones die, their neighbors can move and “fill” the gaps, albeit to varying degrees (**Figure 3.7**) (Carroll et al., 2009; Cideciyan et al., 2013; Curcio, 2001; Hansen et al., 2013). This is evidenced in part by **Figure 3.7**; the ROIs are from 200 μm (**Figure 3.7A**) and 350 μm (**Figure 3.7B**) from the fovea, but have densities and ICD that correspond to only 48% of the normal mean at that eccentricity. However, both have NND and DRPD values that are consistent with a greater than 70% undersampling, and VCAR, NoNR, and percent six sided are consistent with only a 20% undersampling at the same location. Given that each of these metrics describe a different aspect of the mosaic, and that there is such a large disparity between each metric and the undersampling prediction, the behavior of each metric is likely indicative of photoreceptor remodeling following cone degeneration. Regardless, exploring the relationship between different metrics and examining how each responds to both simulated and real loss could enable a quantitative description of the type of loss present within a given mosaic.

In addition, the structural contributions of the rod photoreceptor mosaic were ignored. The ratio of rods to cones has been estimated at 20:1 (Curcio et al., 1990), with rods greatly outnumbering cones by about 10-20 degrees from the fovea. One would expect that the packing of rods and cones into a single mosaic would lead to complex geometrical responses to rod and cone loss that has not been captured by the analysis in this manuscript. Moreover, some retinal degenerations begin in the rod photoreceptor mosaic (*i.e.*, retinitis pigmentosa), and future characterization of the effects of

photoreceptor loss on metrics of the rod and cone mosaic will be essential to characterizing the structural progression of these diseases.

While we examined a wide variety of metrics describing the cone mosaic, this is not an exhaustive list; new metrics may be derived as other retinal cell types are imaged, or as disease processes are better understood. Additionally, metrics can be derived directly from the image; approaches based analysis of the Fourier spectrum of the image ("Yellot's Ring") are already in use (Cooper, Langlo, et al., 2013; Duncan et al., 2007; Ratnam, Västinsalo, et al., 2013; Roorda et al., 2001; Roorda & Williams, 2002; Roorda et al., 2007; Syed et al., 2013; Yoon et al., 2009), and others have been published to assess beam direction in the lamina cribrosa (Sredar, Ivers, Queener, Zouridakis, & Porter, 2013). Metrics derived in this manner have the advantage of being immune to cell identification error, and could be explored in future research.

Our analysis focuses on metric sensitivity, with the assumption that the image quality will be sufficient enough to visualize the entire photoreceptor mosaic. However, there may be situations where image quality cannot be guaranteed, and certain metrics would provide incorrect information. Pathologies such as age-related macular degeneration and RP are also linked with poor image quality due to age or secondary effects of the disease such as cystoid macular edema or cataracts. In those situations the use of a metric that is insensitive (*i.e.*, robust) to undersampling (DRPD, NND, NNR) could provide more accurate data. However, these same metrics would be poorly suited for use in longitudinal studies such as clinical trials, due to this very same insensitivity. In other words, the most sensitive metric cannot be assumed to be the "best" metric. In some situations it may be advantageous to combine metrics with a variety of sensitivities so that a more comprehensive assessment of the integrity of the cone mosaic can be established.

Chapter Four: Methods for investigating the local spatial anisotropy and the preferred orientation of the cone mosaic in adaptive optics retinal images

The contents of Chapter 4 were as a result of collaboration between Dr. Joseph Carroll, Dr. Marco Lombardo (Fondazione G.B. Bietti IRCCS), Dr. Giuseppe Lombardo (Istituto per i Processi Chimico-Fisici), Dr. Kenneth R. Sloan (University of Alabama), and myself. This work was submitted during my graduate studies.

Citation

Cooper, R.F., Lombardo, M., Carroll, J., Sloan, K.R., Lombardo, G. (2015) Methods for investigating the local spatial anisotropy and the preferred orientation of cones in adaptive optics retinal images. Visual Neuroscience. *Submitted.*

Contributions

This project focused on the comparison of three separate algorithms to determine the orientation of sub-mosaics within the photoreceptor mosaic. Dr. Carroll, Marco Lombardo and I were responsible for the overall experiment design. I completed image acquisition with the assistance of Phyllis Summerfelt, Christopher S. Langlo, Melissa A. Wilk, Brian Higgins, Erika Phillips, and Dr. Moataz Razeen. I implemented two of the algorithms presented below: an orientation algorithm described by Pum *et al.*, and a Radon algorithm invented by me, which extracts local orientation based on the Radon transform. Giuseppe Lombardo implemented the Fourier-based algorithm, which he invented. I performed all simulation, image, and algorithm analyses, with guidance provided by both Marco Lombardo and Kenneth Sloan.

The manuscript and figures were created by me, with critical input and feedback provided by Marco Lombardo and Joseph Carroll.

Introduction

AO retinal imaging tools have substantial potential for use in the diagnosis of retinal disease. The improvement in retinal image contrast and resolution allows the direct observation of the cone and rod photoreceptors (Dubra et al., 2011), allowing the opportunity to directly assess pathology early in the disease course. Central to the clinical application of this technology is the ability to quantitatively analyze the photoreceptor mosaic. At present, the majority of studies have focused on the analysis of cone density and spacing of cones (Chiu et al., 2013; Chui, Song, & Burns, 2008a; Dees et al., 2011; Garrioch et al., 2012; Li & Roorda, 2007; Li et al., 2010; Lombardo, Lombardo, et al., 2013; Park et al., 2013; Ratnam, Västinsalo, et al., 2013; Song et al., 2011). These studies demonstrate moderate to high variability within cone density and spacing within the healthy adult population, making it difficult to detect small deviations from normal. However, despite individual differences in cone density and spacing, the parafoveal cone mosaic uniformly presents as a triangular lattice, and it is thought that the quality of the cone lattice is involved in the inter-receptoral network and cell signaling (Hirsch & Miller, 1987; Lombardo, Serrao, Ducoli, & Lombardo, 2013; Pum et al., 1990). Thus, disorder in cone packing could serve as an important and sensitive measure with which to characterize the cone mosaic (Baraas et al., 2007; Wojtas, Wu, Ahnelt, Bones, & Millane, 2008).

The geometry of the overall cone mosaic can be easily visualized by defining the Voronoi domain associated with each cone photoreceptor cell in the mosaic. In a perfectly triangular lattice, all cones will have hexagonal Voronoi domains. While numerous investigators have demonstrated that the majority of cones in the normal parafoveal cone mosaic have this geometry (Baraas et al., 2007; Carroll, Banin, et al., 2010; Dees et al., 2011; Dubra et al., 2011; Li & Roorda, 2007; Lombardo, Serrao, et al.,

2013; Rossi, Carroll, & Roorda, 2008; Wagner-Schuman et al., 2010), there are only a few studies in which mosaic geometry is used to detect retinal pathology in AO imagery. For example, Baraas et al. (2007) imaged individuals with congenital tritan color vision deficiency and observed density within normal limits but significantly disrupted regularity, with the percentage of six-sided Voronoi cells being substantially lower (55%) than normal controls (70%). The authors concluded that the short-wavelength sensitive (S-) cones degenerated in these patients, and the observed normal density could be explained by the fact that the S-cones comprise only about 5% of the total number of cones, which is significantly smaller than the known inter-individual variability in cone density. Wagner-Schuman et al. (2010) observed normal mosaic geometry in patients with a novel W149X mutation in the middle-wavelength opsin gene, despite significant reduction in cone density. This suggested that the cones expressing the mutated opsin were lost early in development, allowing the remaining cones to pack in a regular fashion.

Further insight into the packing regularity of the cone mosaic can come from assessment of the local orientation of cones within the mosaic. Orientation is defined as the local apparent angle of the photoreceptor mosaic. Previous work has shown that the human cone mosaic forms a variable number of hexagonal sub-mosaics that differ in orientation and are separated by cones with non-hexagonal arrangements (Ahnelt & Kolb, 2000; Pum et al., 1990). Algorithms for assessing the orientation of the cone mosaic were originally developed for use in histological images, but to our knowledge have not been applied to AO images of the cone mosaic. Thus, the aim of the present work was to apply Pum's method (1990) as well as two new methods for analyzing the anisotropy and orientation of cones, in simulated and real AO images of the parafoveal cone mosaic. The new methods were based on Fourier (Meitav & Ribak, 2011) and Radon transforms (Deans, 1983) and were compared to the previously developed

algorithm (Pum et al., 1990). We demonstrate that the orientation of individual cones within the mosaic can be accurately measured using these techniques.

Methods

Three algorithms were implemented to assess the orientation of a set of photoreceptors in images using MATLAB (Mathworks Inc, Natick MA, USA). Each algorithm was tested on both simulated and real images of the cone photoreceptor mosaic. For each image, cone photoreceptor coordinates were used to derive a Voronoi diagram for the mosaic. The number of neighbors of a given cone was defined as the number of sides of the Voronoi polygon corresponding to that cone's location. Only orientation information for cones with six neighbors was obtained with each algorithm.

Neighbor Derived Orientation

Spatial orientation analyses assess the local neighborhoods of individual cones. For a given cone location, nearby neighbors can be identified either by distance (Pum et al., 1990) or by using a Voronoi diagram (Curcio & Sloan, 1992). The original method in Pum et al. (1990) selected the seven nearest neighbors and excluded any cones outside ±30% of the median neighbor distance. Cells within the ±30% median distance "band" were used for analysis. Curcio & Sloan (1992) modified this step to use the neighbors defined by the Voronoi diagram of the cone centers. Both methods limited further analysis to those cones with only six neighbors.

In the neighbor-derived orientation, a vector is created from the central cone to each neighbor. Pum et al. (1990) used the median-distance neighbor to define an initial reference vector, and computed the difference between that vector and the vector from the central cone to each of the other neighbors, adjusting the differences in angle to lie between ±30°. These adjusted vectors plus the original reference vector were added and

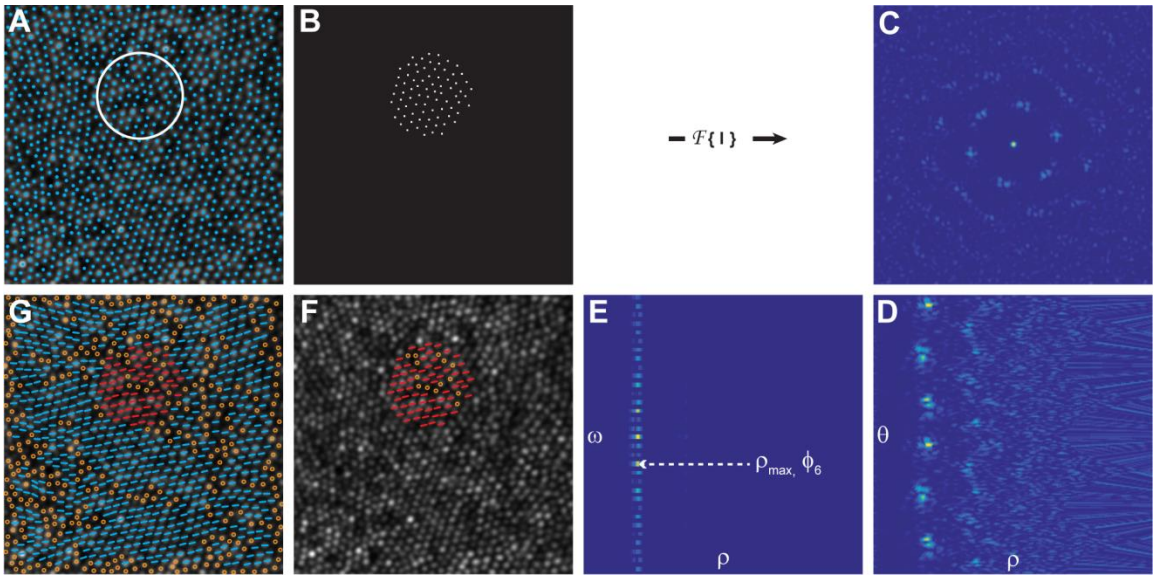

Figure 4.1: An outline of the steps to retrieve the orientation of individual cones using the Fourier method. A) Individual cones in an image of the cone mosaic (AOSLO or AO-flood) are identified using a cone identification algorithm, and the mean inter-cell neighbor distance is calculated. A region of interest (ROI; white circle) with a diameter 4.5 times greater than the inter-cell distances is sampled uniformly across the image such that each ROI overlaps by 50% with each of its neighboring ROIs. B) For each ROI, a binary mask is used to generate an image of the cone coordinates, I(x,y). C) The power spectrum, f(u,v) = FFT (|I(x,y)|2), is calculated for each ROI and converted to polar coordinates, f(ρ,θ), as shown in (D). E) Next, a 1D - FFT is performed on the angular content of the power spectrum of f(ρ,θ): F(ρ,ω) = FFT(|f(r,θ)|^2). The spatial characteristic length scale, associated with the hexagonal arrangement of the cones within the ROI, is defined as dhex = 1/ρ_max, in which ρ_max represents the maximum value of the module F(ρ,6). F) The corresponding local mean orientation of the hexagonal arrangement is calculated as Φ6 = -arg(F(ρ_max,6)/6) and it expresses the average angular hexagonal neighbor orientation for each ROI. G) The final orientation for each six-sided cell is computed by taking the mean of average angular hexagonal neighbor orientations of the ROI in which that cell fell. Non six-sided cells are shown as open circles in F & G. The AO image subtends a 120x120 μm area.

divided by 6 to yield a “characteristic vector” which contained information about size and orientation of a hexagon centered on that central cone (Pum et al., 1990). Curcio & Sloan (1992) used a slightly different method of computing orientation, which took the median of the adjusted vectors and reference vector to create the “characteristic vector”, though both methods yielded similar results, producing a characteristic orientation which

ranges over 60° because of the presumed six-way symmetry of the hexagonal neighborhood. The Pum algorithm was implemented for this study.

Fourier Derived Orientation

Fourier spectral analysis is intrinsically insensitive to cones missed or misidentified in the image and provides global, reliable information on their spacing, arrangement and periodicity. Based on this premise, a spectrum angular Fourier method was performed on several overlapping circular regions of interest (ROIs) (*e.g*, two adjacent areas were 50% overlapped), I(x,y), with a diameter 4.5 times greater than the inter-cell distance (ICD) of the given mosaic (**Figure 4.1**). This ROI size was empirically determined to be optimal. The power spectrum of each ROI, f(u,v) = *FFT* (|I(x,y)|^2), was extracted and converted to polar coordinates f(ρ,θ). In general f(ρ,θ) can be written as a sum of cosine angular function components:

$$f(\rho,\theta) = A_0(\rho,\theta) + \sum_{n=1}^{\infty} A_n(\rho,\theta)\cos[n(\theta - \phi_n(\rho,\theta))] \qquad \textbf{(Eq. 4.1)}$$

where $A_n(\rho,\theta)$ and $\phi_n(\rho,\theta)$ are the amplitude and the phase of the nth Fourier harmonic components of $f(\rho,\theta)$ respectively. The information on the packing arrangement, such as spacing and orientation, can be retrieved by taking the 1-D Fourier transform on the angular content of the power spectrum of (1) and evaluating the modulo component and the phase of (2).

$$F(\rho,\omega) = FFT(|f(\rho,\theta)|^2) \qquad \textbf{(Eq. 4.2)}$$

The sixth spectrum component, F(ρ,6), contains frequency information about the six equidistant vertices, regardless of the orientation of the hexagonal packing. For each ρ value, the modulus F(ρ,6) represents the size of the hexagonal arrangement and its corresponding phase represents the local hexagonal packing orientation. If we extract the value ρ_{max}, which represents the maximum value of the modulus F(ρ,6), the

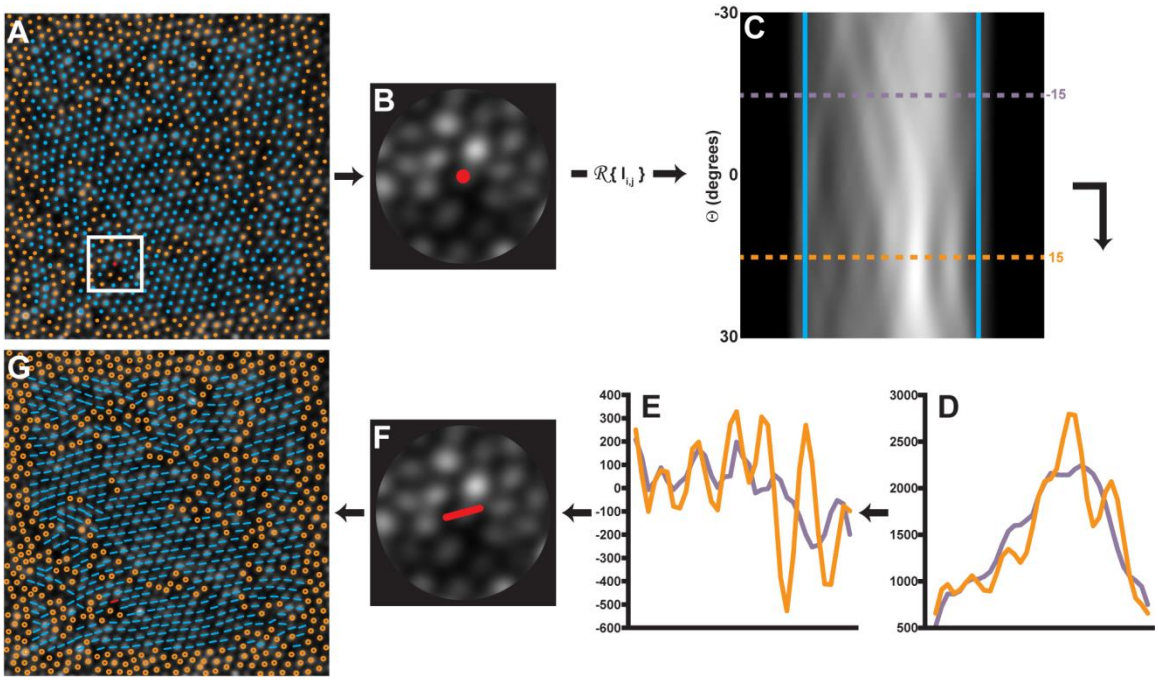

Figure 4.2: An outline of the steps used to determine the orientation of individual cones using a Radon transform. A) An ROI 4.5 times the ICD is centered on each cone with a 6-sided Voronoi domain (cyan closed circles) within the image. Non six-sided cells are not analyzed (orange closed circles). B) A circular mask is applied to the ROI. B-C) The Radon transform is applied to the ROI and the sides of the transform are cropped (blue lines). Each cropped row of (C) contains information from each angle θ of Radon projection. D) Shows the projection profiles at two rows corresponding to -15° (purple profile) and 15° (orange profile). To determine the row with the most contrast, the 2nd derivative of each row is performed (E), and the row θ with the highest RMS (orange profile) is selected as the orientation at that location. A low RMS location (purple profile) is shown for comparison. F) The orientation is assigned to that cell. G) The algorithm is repeated for each 6-sided cell location in the image. Non six-sided cells are shown as open circles in G. The AO image subtends a 120x120 µm area.

corresponding $d_{hex} = 1/\rho_{max}$ can be identified as the spatial characteristic length scale associated with the hexagonal arrangement on the ROI. The corresponding local mean orientation of the hexagonal arrangement is calculated as $\phi_6 = -\arg(F(\rho_{max},6))/6$ and here was used as the *average angular hexagonal neighbor orientation.* The algorithm steps are shown graphically in **Figure 4.1**.

Radon Derived Orientation

Another approach was derived using the Radon transform (Deans, 1983). The Radon transform is an integral transform typically performed over a series of straight "projection" lines. The inverse of the Radon transform is used extensively in reconstruction of medical computed tomography images (Deans, 1983). Here we used the Radon transform to assess orientation by determining the projection angle, which typically occurs along the orientation of the cones. To accomplish this, an ROI that was 4.5 times the mean ICD was extracted at each cone location **(Figure 4.2A)**. This ROI size was empirically determined to be optimal; a larger ROI was insensitive to local changes in orientation, while a smaller ROI was too sensitive to local changes and had noisy results. A circular mask was applied to each ROI **(Figure 4.2B)**, and each ROI was transformed using the Radon transform

$$f(r,\theta) = R(I(x,y)^2) \quad \textbf{(Eq. 4.3)}$$

where θ is the angle of the projection and r is the projection bin. In the radon-transformed ROI, each row (θ) was an angle and each column was a projection bin (r) **(Figure 4.2C)**. Because the rotation of a hexagon can only be detected over a -30° to 30° range, only θ between the values of 60-120° (where 90° is horizontal) were considered.

When a Radon transform is oriented along the axis of the photoreceptors contained in a ROI, it creates a characteristic multi-peak pattern across the projection bins (r) (**Figure 4.2D, orange profile**) corresponding to the dominant orientation at that location. This information can be extracted from the Radon transform by assessing the row (θ) at which the multiple-peak pattern is most resolvable. To mitigate the effect of image noise on our measurement of the multiple peaks, each row (θ) was smoothed with a Gaussian filter (5^{th} order, $\sigma = 0.75$), and the 2^{nd} order derivative of the smoothed row was calculated. The central region of the row was cropped to exclude the masked area

using the first and last zero-crossings, and the root-mean-square (RMS) of the cropped, differentiated profile was calculated along each row. The row with the maximum RMS was taken as the main orientation of the ROI.[1]

Algorithm Validation

To assess the accuracy of the algorithms, a simulated cone mosaic with perfect hexagonal packing was created as an idealized model of the human parafoveal cone mosaic. The simulated mosaic subtended 150x150 μm with a 0.45 μm/pixel, and the cone spacing (ICD = 3.64 μm) corresponded to a density of 87,000 cones/mm^2. The relationship between spacing and density is consistent with that of a perfect hexagonal mosaic, according to methods described by Coletta & Williams (1987). The coordinates were rotated (between ±30°; with 1° step), and then cropped to a 120x120 μm area for analysis. From this set of coordinates, an accompanying cone "image" was generated by convolving a 2D Gaussian with a binary mask at each of the cone locations. Each algorithm was run on each rotated cone mosaic. The results of each algorithm were then compared to the known rotation.

We further examined the accuracy of the algorithms in the presence of noise by perturbing the coordinates in the perfect mosaics by a random amount drawn from a Gaussian distribution with a mean of 0 and a standard deviation equivalent to 5% of the cone spacing (0.21 μm). Additionally, the intensity of each cone in the image was

---

[1] ***Orientation Unwrapping***
Since six-neighbor cells can assume orientations over a periodic range of ±30°, a *wrapping effect* can occur whenever the value is close to either extreme of that range. The orientation periodicity precludes the direct recovery of true orientation differences. For example, cone orientations of -29° and 30° without adjusting for wrapping would erroneously be considered 59° apart. This can be particularly detrimental for any comparisons that rely on a monotonic scale, such as the intraclass correlation coefficient (ICC). To address this, we unwrapped the orientations when differences between algorithm orientations were greater than 30° apart. Thus, in the example presented above, the angles would become 31° and 30°, correctly representing the actual difference (1°) between results from the different algorithms.

adjusted by randomly selecting an intensity from a log-normal distribution with a 24.9 arbitrary units (A.U.) standard deviation and mean intensity of 80 A.U., based on cone reflectivity values previously observed in AO images from normal subjects (Cooper, Dubis, et al., 2011).

Testing Algorithm Performance

To examine the performance of each algorithm on a more realistic simulated mosaic, we generated mosaics that contained multiple sub-mosaics of differing local orientation. A 130x130 μm area (0.45 μm/pixel scale) was created, and twenty locations from within the area were randomly drawn from a uniform distribution and used as seed locations for each sub-mosaic. Each seed location was assigned a random rotation within a range of ±30°, and new cones were added radially to each seed, separated by an azimuth of 60° and a radius defined by an ICD of 3.64 μm so as to maintain a hexagonal lattice fixed at the seed's assigned orientation. This process was repeated for each cone until encountering another cone. Once no more cones could fill the area, the cone locations were "relaxed" 100 times using a "hard disk" model similar to that proposed by Stillinger et al. (1964) (Stillinger, DiMarzio, & Kornegay). The final mosaic was then cropped to a 120x120 μm area for analysis. One hundred simulated mosaics, which contained 77±2% six-sided Voronoi cells, were created in this manner. An accompanying cell image was generated for each simulated mosaic as previously stated, and all three algorithms were then run on each simulated image.

Finally, each algorithm was tested using 17 images acquired from 17 subjects using a custom AOSLO (Dubra & Sulai, 2011). This research was conducted according to the tenets of the Declaration of Helsinki, and image acquisition was approved by the Institutional Research Boards at the Medical College of Wisconsin and Marquette University (Milwaukee, WI). AOSLO images were acquired 0.5 degrees temporal from

fixation using a 790nm scanning beam over a 1.0° field of view (FOV). Axial length measurements were obtained on all subjects using an IOL Master (Carl Zeiss Meditec, Dublin, CA), and used in combination with a simplified Gullstrand II model to convert from degrees of visual angle to microns on the retina. The central 120x120 µm was cropped from each image. Cone coordinates were semi-automatically identified using a previously described algorithm (Garrioch et al., 2012). The spacing of cones and their packing arrangement were analyzed using ICD and a Voronoi tessellation, which was used to extract the percentage of six-sided cones. The Pum, Fourier, and Radon algorithms were run on each image as described above.

Analysis of Algorithm Performance

To examine algorithm accuracy in the rotated versions of a perfect simulated mosaic, we compared the orientation of each six-neighbor cone to the known rotation of the simulated mosaic. The detected orientation of each cone from each algorithm was subtracted from the known rotation for evaluating the error. A tolerance interval ±3° of the known rotation was used to account for rounding error and noise. Any cone orientations which fell outside the tolerance interval were considered incorrect.

For simulated mosaics containing multiple sub-mosaics or real images of the cone mosaic collected using AOSLO, we compared the algorithms by estimating sub-mosaic homogeneity. Homogeneity was determined by overlaying a grid with 15x15 µm spacing on each mosaic. The variance of the orientation of cells within each grid square was calculated. Homogeneity was defined as the average pooled variance across all grid squares. Pooled variance describes the average spread of all grid variances about their mean; the higher the pooled variance in this analysis, the lower the sub-mosaic homogeneity by a given algorithm.

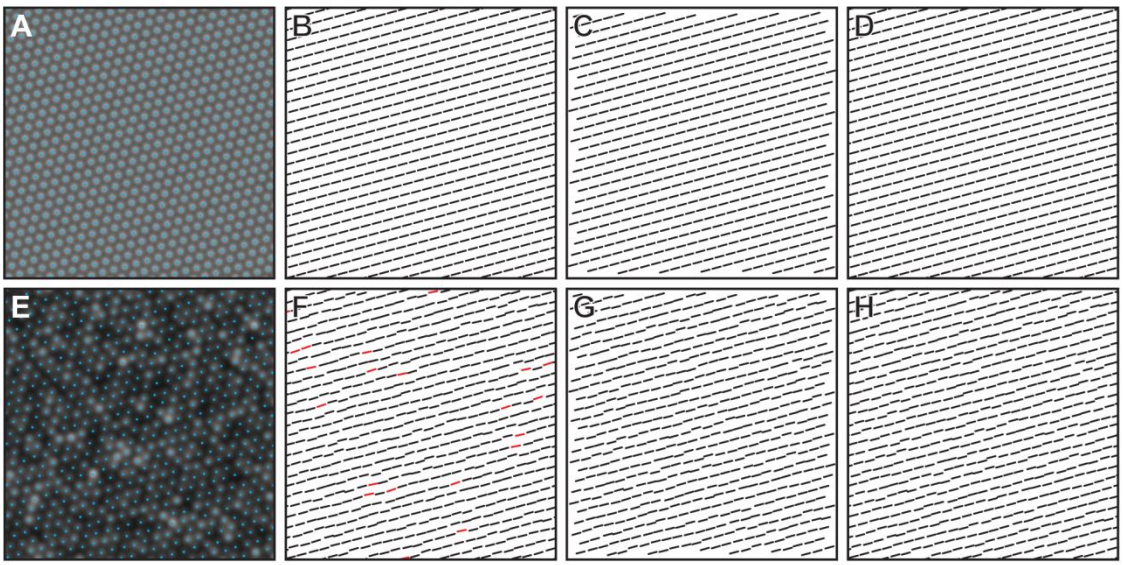

Figure 4.3: Comparison of orientation algorithms using an 87,000 cones/mm2 simulated mosaic with (A) and without (E) cone intensity variation and coordinate jitter. The neighbor derived orientation (Pum, Ahnelt, & Grasl, 1990) algorithm correctly determines the orientation of the mosaic without any coordinate jitter (B, black orientation bars), but can produce results outside of tolerance (>|3°|, red orientation bars) when the coordinates are jittered and cone intensity varied (F). Both the Radon (C,G) and Fourier (D,H) algorithms are insensitive to coordinate jitter and image intensity variability.

We measured algorithm agreement using both the Pearson correlation coefficient and the intraclass correlation coefficient (ICC) based on a two-way random model. The Pearson correlation coefficient was calculated to estimate the correlation between algorithm pairs, and the ICC was used to estimate the reliability between orientations from all three algorithms. All statistical analyses were performed in SPSS (IBM, Armonk, NY).

Results

Simulated Mosaic Performance

For the rotated versions of the ideal simulated mosaic, each algorithm was able to correctly assess the amount of rotation applied to the mosaic. **Figure 4.3** exemplifies the

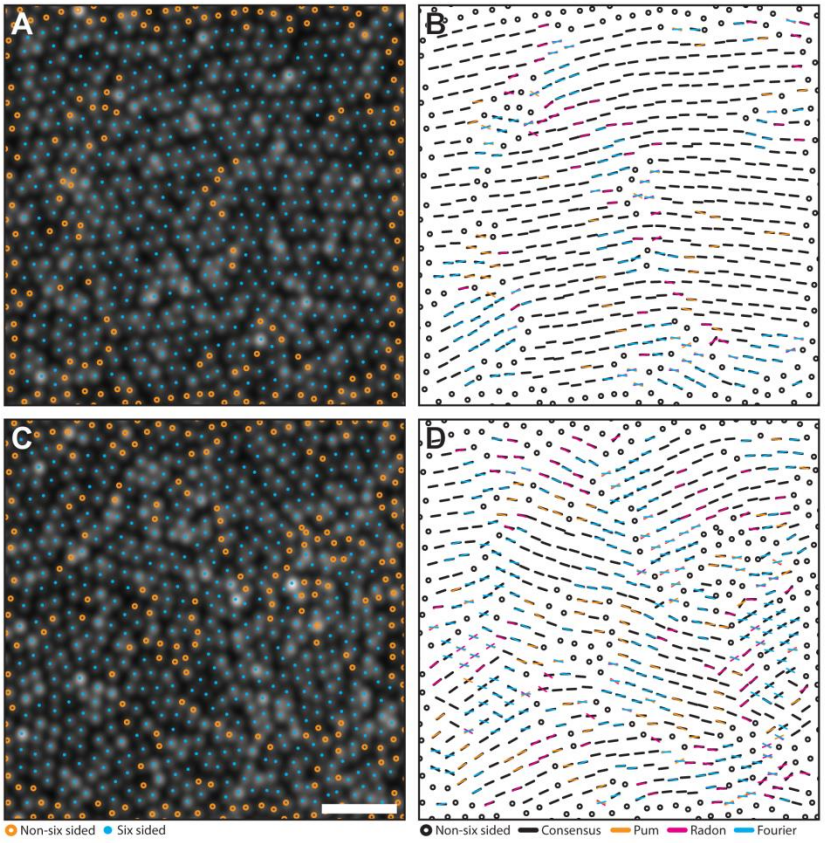

Figure 4.4: A comparison of the agreement of orientation algorithms in simulated mosaics with the high (A-B) and low (C-D) agreement. Cyan closed circles mark six-sided cell locations, while orange circles mark unanalyzed, non-six sided cells (A, C). Black bars are locations where at least two algorithms agreed within their combined 6° tolerances (B, D). Each color in the right column corresponds to results from each algorithm (Pum: orange, Radon: magenta, Fourier: cyan). If one algorithm was outside tolerance, a bar with the corresponding color was overlaid on the black bar. If all three algorithms disagreed, the orientation from each method is plotted. Scale bar is 20 µm.

ability of each algorithm to detect the orientation of a perfectly hexagonal mosaic either in the absence or presence of noise. In a perfect mosaic (**Figure 4.3A**), correct identification of cone orientation within the ±3° tolerance was achieved for 100%, 99.8%, and 100% of cones using the Pum, Fourier, and Radon approaches, respectively (**Figure 4.3B-D**). The Fourier algorithm's 0.2% error was due to the perfect lattice with no rotation; the hexagonally located coordinates created artifacts in the Fourier domain, causing the algorithm to return erroneous values. Given that this only occurred in an

extreme (and non-physiologic) case, we considered the algorithm's performance to be equivalent to that of the other two. The average absolute errors were 0.06±0.02°, 0.11±0.04°, and 0.10±0.24° for the Pum, Fourier, and Radon approaches, respectively. When noise in the form of coordinate jitter and cone intensity variation was applied to the image (**Figure 4.3E**), correct identification of cone orientation within the ±3° tolerance was achieved for 95.8%, 99.9%, and 99.9% of cones using the Pum, Fourier, and Radon approaches, respectively (**Figure 4.3F-H**). The average absolute errors for the noisy mosaic were 1.18±0.04°, 0.15±0.08°, and 0.22±0.26° for the Pum, Fourier, and Radon algorithms, respectively. Taken together, these results demonstrate excellent accuracy for all three algorithms.

The 100 simulated mosaics containing multiple sub-mosaics had an average of 76.9±2.1% six-sided Voronoi cells, and an average ICD of 3.8±0.03. This ICD was slightly larger (5.5±0.7%) than the ICD derived from the average density of each simulated mosaic (78,486±1,262 cones/mm^2). This was consistent with previous observations that within the photoreceptor mosaic there are point and line discontinuities where the hexagonal lattice is disrupted (Ahnelt & Kolb; Pum et al., 1990). The presence of these disruptions in the mosaic reduces the number of ideally packed cones, increasing the measured ICD. Qualitatively, we found that both the Pum and Fourier methods were particularly susceptible to artifacts around the edges of six-sided sub-mosaics; this was likely related to noise from neighboring non-hexagonal cones. On average, the Fourier method was the most homogenous with a 20.2±9.0 pooled variance across all sub-mosaics, while the Pum and Radon methods showed pooled variances of 28.1±4.5 and 32.6±6.3, respectively (**Figure 4.4**). The results from each simulated mosaic are summarized in **Table 4.1.** We found that the Radon and Pum methods correlated more closely ($r=0.92$; $p<0.01$) than the Radon and Fourier methods ($r=0.85$;

Table 4.1: Summary of Simulated Mosaic Descriptive Metrics (continued on next page)

Mosaic #	Density (cones/mm^2)	ICD (μm)	%6 Sides	Average Sub-mosaic Pooled Variance			Mosaic #	Density (cones/mm^2)	ICD (μm)	%6 Sides	Average Sub-mosaic Pooled Variance		
				Pum	Radon	Fourier					Pum	Radon	Fourier
1	77596	3.82	74.6	19.9	21.3	31.9	**51**	78063	3.88	78.2	29.3	37.3	29
2	77962	3.86	71.7	27.9	34.6	30.5	**52**	77932	3.84	78.2	32	35.3	7.7
3	78575	3.86	73.8	36.9	34.1	10.1	**53**	77660	3.85	69.7	27	30.2	32.7
4	78127	3.84	79.5	26.1	27.4	13.6	**54**	78112	3.87	78.2	21.7	22.4	34.6
5	79149	3.84	76.9	29.3	34.3	8.3	**55**	78673	3.85	76.5	30.6	34.8	17.3
6	79026	3.84	76.7	24.5	28.3	17.1	**56**	77878	3.84	77.6	26.4	37.3	37.6
7	77110	3.83	76.2	23.8	31.6	46	**57**	77839	3.85	77.4	26.7	25.7	22.3
8	78343	3.87	78.2	29.2	31.6	21.4	**58**	78229	3.86	78.9	27	27.2	29.5
9	80415	3.85	79.3	30.6	34.5	31.5	**59**	77870	3.85	77.4	34.2	38.8	9.3
10	76731	3.81	76.4	30	34.3	29.1	**60**	78419	3.85	78.2	29.2	30.5	10.2
11	79219	3.88	76.4	33.8	34.6	25.4	**61**	78195	3.85	77.3	36.8	37.3	12.4
12	79707	3.83	77.9	32.3	36.6	9.3	**62**	77428	3.85	78.2	23.2	30.5	29
13	77672	3.78	76.5	35.3	31.1	19.5	**63**	78726	3.87	78.7	23	25.4	15.4
14	81162	3.86	78.1	37.5	47.7	10	**64**	80915	3.84	76.2	32.4	39.9	19.2
15	77873	3.78	77.7	23	33.6	10.5	**65**	76372	3.8	77.1	24.6	34.9	7.1
16	78298	3.86	77.3	25.6	35.9	21.7	**66**	77466	3.9	77.2	27.6	41.5	25.1
17	77436	3.86	72.3	25.1	20.4	15.5	**67**	78390	3.87	75.2	27.4	32.8	22.3
18	80399	3.87	76.7	33.9	37.6	15.6	**68**	78691	3.84	80.5	33.6	47.4	18.7
19	80074	3.8	75	30	34.9	20.3	**69**	80413	3.84	76.6	33.7	35.9	23
20	79314	3.81	77.4	29.4	39.6	16.3	**70**	77953	3.8	76.5	26.7	36.6	13.4
21	76961	3.83	70.4	23.2	28.8	9.1	**71**	79811	3.86	73.5	26.7	39.2	17.9
22	77464	3.87	79.3	26.8	33.6	22.1	**72**	78632	3.82	78.1	26.9	36.9	33.2
23	81777	3.87	76.3	35.2	38.2	25.2	**73**	78491	3.84	76.1	27.9	38.7	14
24	77462	3.8	78.3	25.1	28.6	27.7	**74**	78404	3.85	78.2	26.5	34.8	32.2
25	78238	3.87	73.7	20.9	23.2	18.6	**75**	78827	3.85	77	27.9	28.3	14.1
26	82282	3.85	75.9	28	33.6	21	**76**	78120	3.84	76.4	31.1	35.3	22.4

Mosaic #	Density (cones/mm^2)	ICD (µm)	%6 Sides	Average Sub-mosaic Pooled Variance			Mosaic #	Density (cones/mm^2)	ICD (µm)	%6 Sides	Average Sub-mosaic Pooled Variance		
				Pum	Radon	Fourier					Pum	Radon	Fourier
28	77426	3.88	79.8	25.2	21.2	11.7	**78**	78464	3.87	77.4	29.9	30.2	26.9
29	77811	3.87	77.7	34.3	32	13.5	**79**	77595	3.85	77.8	27.9	27.5	35.9
30	76876	3.87	78.2	22.7	23.6	27.4	**80**	77791	3.87	79.7	33	27.4	15.1
31	78697	3.89	79.7	29.7	33	16.4	**81**	79181	3.86	76.7	32.2	37.1	16.2
32	79403	3.84	71.6	28.1	27.1	7.2	**82**	77673	3.82	78	20.6	20.8	21
33	77583	3.82	74.1	27.6	21.8	8.6	**83**	77325	3.87	79.7	33.5	33.4	10.8
34	80415	3.87	77.4	26	37.3	26.1	**84**	79387	3.86	78.5	24.2	30.8	31.4
35	77882	3.85	75.5	28	43.7	4.4	**85**	77134	3.83	78.8	25.4	23.7	23.8
36	76864	3.85	79.6	25.5	26.8	20.5	**86**	78809	3.87	78.7	32.7	40.2	21.8
37	77621	3.88	79.4	21.1	20.3	38.2	**87**	77175	3.84	78.5	38.7	45.8	10.2
38	77793	3.86	77.4	25.5	30.9	19.8	**88**	81248	3.88	76.4	33.7	40.5	18.1
39	77643	3.86	79	24.2	27.2	35.3	**89**	78245	3.79	72.1	22.6	32.7	17.3
40	80524	3.87	75.2	32.6	39.9	9	**90**	76911	3.84	78.5	21.7	24.5	16.9
41	77592	3.8	78	27.4	29.9	29.5	**91**	78126	3.88	78.1	26.1	26.7	16.4
42	77483	3.87	77.9	21	28.9	5	**92**	78185	3.85	77.1	27.6	36.2	34.5
43	79328	3.87	78.5	27.3	41.5	13.1	**93**	78245	3.85	75.6	31.9	39.7	8.5
44	78328	3.83	78.9	21.5	21.9	26.2	**94**	78749	3.85	77.6	32.9	41.2	13.8
45	78285	3.86	76.5	21.5	31.2	18.4	**95**	77376	3.84	77.8	25.2	30.6	20.8
46	81855	3.86	78.5	27	29.3	16.5	**96**	78471	3.87	79.5	26	27.1	18.6
47	80904	3.78	80.1	28.7	27.5	28.7	**97**	78819	3.85	77.8	20.5	31.5	28.4
48	76999	3.8	76.3	25.9	33.5	14.2	**98**	79484	3.85	74.3	32.2	36.7	40.9
49	81930	3.87	79.8	38.9	38.5	18.3	**99**	78569	3.81	76.7	29.6	43.9	4.6
50	77350	3.77	76.1	30	36.8	20.9	**100**	78541	3.85	78	26.2	26.9	20.1
							Average	**78486**	**3.85**	**77.08**	**28.14**	**32.61**	**20.2**

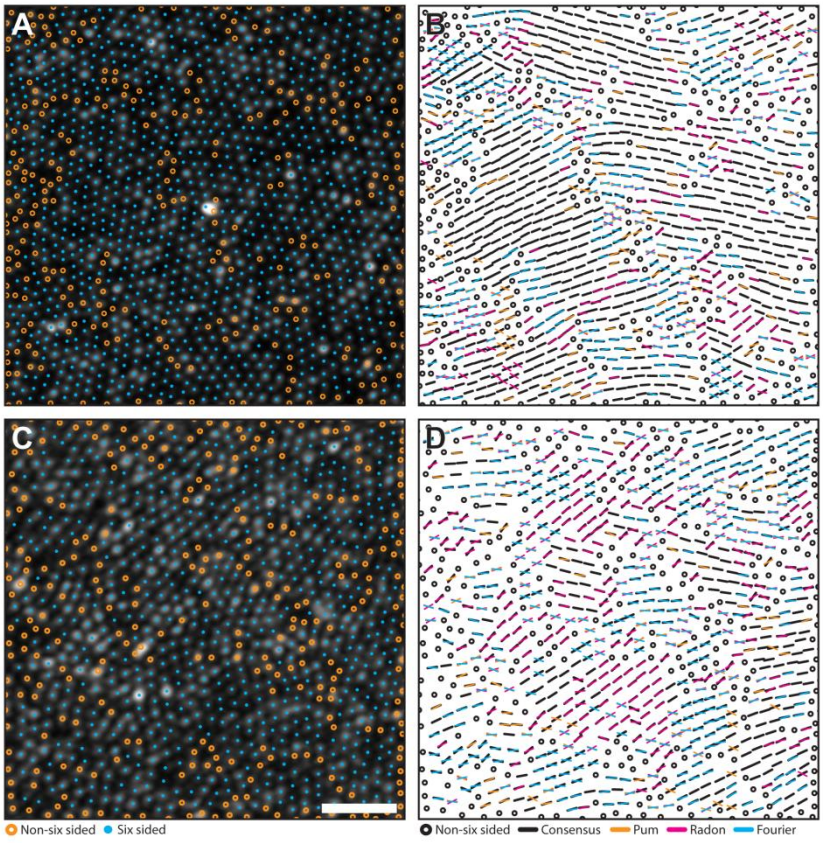

Figure 4.5: A comparison of the agreement of orientation algorithms in AOSLO images with high (A-B) and low (C-D) agreement. Cyan closed circles mark six-sided cell locations, and orange circles mark to unanalyzed, non-six sided cells (A, C). Black bars are locations where at least two algorithms agreed within their combined 6° tolerances (B, D). Each color in the right column corresponds to results from each algorithm (Pum: orange, Radon: magenta, Fourier: cyan). If one algorithm was outside tolerance, a bar with the corresponding color was overlaid on the black bar. If all three algorithms disagreed, the orientation from each method is plotted. Scale bar is 20 µm.

$p<0.01$) and the Pum and Fourier methods ($r=0.84$; $p<0.01$). The average ICC for all pairwise correlations among all three algorithms was 0.95.

Real Mosaics

The real photoreceptor mosaics from 17 subjects contained on average 71±3% six-sided Voronoi cells. The average density was 85,789±13,251 cones/mm^2, and average ICD was 4.0±0.3 µm. Using each mosaic's density to calculate the expected ICD for a perfect

triangular lattice (Coletta & Williams, 1987), we again found that the measured ICD was consistently larger (9.0±0.8%) than the ICD derived from the mosaic density. When examining the orientation of the real mosaics, only the Fourier algorithm had an average pooled variance similar to the simulated parafoveal mosaics (22.2±7.9)(**Figure 4.5**). In contrast, the Pum and Radon methods were less homogenous than the simulated mosaics with average pooled variances of 40.6±5.6 and 41.3±7.9, respectively. The decreased homogeneity of both the Pum and Radon methods could be due to the lower percentage of six-sided Voronoi cones in real mosaics; on average, there were 5.9% fewer hexagonal cones in real mosaics than in simulated mosaics. While the orientation of non-hexagonal cones is not calculated for either algorithm, their presence still influences the orientation of neighboring hexagonal cones, potentially decreasing the observed homogeneity. Despite the decreased homogeneity in real mosaics, we found that the Radon and Pum methods still correlated more closely ($r=0.87$; $p<0.01$) than the Radon and Fourier methods ($r=0.82$; $p<0.01$) and the Pum and Fourier methods ($r=0.82$; $p<0.01$). The average ICC for all pairwise correlations among all three algorithms was 0.94. The results from each AOSLO dataset are summarized in **Table 4.2.**

Discussion

In this work, we have shown the performance of a previous orientation detection algorithm (Curcio & Sloan, 1992; Pum et al., 1990), as well as two new approaches for detecting cone orientation. The algorithms had very good reliability across both simulated (0.94) and real mosaics (0.95), suggesting that each algorithm would provide an accurate description of photoreceptor orientations when applied to the coordinates (Pum and Fourier) or directly to an image (Radon). Analysis of inter-algorithm correlations highlighted the differences between the Fourier method and the Pum and

Radon methods; we found a lower correlation between the Fourier and Pum algorithms and the Fourier and Radon algorithms than between the Pum and Radon algorithms.

Table 4.2: Summary of AOSLO Descriptive Metrics

				Average Sub-mosaic Pooled Variance		
Subject ID	**Density (cones/mm^2)**	**ICD (mm)**	**% 6 Sides**	**Pum**	**Radon**	**Fourier**
AD_10252	90932	3.97	71.8	41.7	54.6	24.2
AD_10253	78959	4.18	68	45.2	40.5	18.8
JC_0077	84418	4.03	73.3	41.3	41.2	29.6
JC_0677	111954	3.49	74.8	32.5	47	30.7
JC_0878	81264	4.09	69.7	45.5	44.6	31.7
JC_0905	87428	3.96	77.3	34.3	34.6	21.3
JC_10119	83935	4.04	71.1	41.1	47.2	26.8
JC_10121	87417	3.93	73.3	42.6	42.6	20.4
JC_10122	113970	3.47	68.2	43.1	51.7	15.9
JC_10145	78572	4.2	71.9	39.3	32.7	15.3
JC_10147	99352	3.69	70.9	47.7	46.4	31.7
JC_10304	87701	3.99	71.2	47.2	35.2	12
JC_10312	73170	4.42	68.3	40.5	34.5	10.8
JC_10316	74534	4.31	67.3	34.2	27.6	12.4
JC_10317	61587	4.76	67.8	43.7	50.8	18.1
JC_10318	75277	4.3	74.2	26.7	31.8	37.2
JC_10329	87940	3.96	71.7	43.4	39.2	19.8
Average	**85789**	**4**	**71.2**	**40.6**	**41.3**	**22.2**

This is likely due to orientation averaging present in the Fourier algorithm. Specifically, the orientation of an area determined by the Fourier algorithm is the average of the local mosaic orientation and the orientations of the surrounding region. This is in contrast to the Pum and Radon methods, which do not average surrounding orientations. The intrinsic regional averaging performed in the Fourier method allows the algorithm to be robust to local changes in orientation; this property was reflected by sub-mosaic homogeneity that was similar between the Pum and Radon algorithms but consistently lower for the Fourier algorithm in both simulated and real data (**Table 4.1 and 4.2**).

However, regionally averaging multiple orientations can result in inaccuracies near the edges of sub-mosaic patches where non six-sided cells and sub-mosaics with different dominant orientations meet (Curcio & Sloan, 1992; Lombardo, Serrao, et al., 2013; Lombardo et al., 2014; Pum et al., 1990). Understanding this difference as well as other algorithm limitations is essential to understanding the specific utility of each algorithm. For example, the accuracy of the Fourier and Pum approaches is directly linked to the accuracy of the cone identification algorithms that provide their coordinates. Cone identification algorithms can miss cones, identify extra cones, or incorrectly identify a cone's centroid (Lombardo et al., 2014); each of these scenarios could affect the results of both the Fourier and Pum algorithms. The Fourier method is able to overcome cell coordinate imprecision, or "jitter", because any small differences in coordinate location are integrated when the coordinates are first transformed (**Figure 4.1D**), whereas the Pum method can return an erroneous result if the axis of the jitter is perpendicular to the circumference of the polygon formed by neighboring cones. This limitation can be seen in the ideal mosaic results (**Figure 4.3**), where the accuracy of the Pum method decreases markedly from 100% to 95.8% in the presence of coordinate jitter.

In contrast to coordinate-centric approaches, the Radon method is performed directly on the image and only uses the cone coordinates to determine which locations to analyze. Because the algorithm is performed directly on the image, the algorithm requires image quality sufficient enough to resolve inter-cell spacing. Therefore, any image with poor cell resolution due to either poor image quality or an insufficient system resolution will cause the algorithm's results to be unreliable. Moreover, the Radon algorithm cannot determine the orientation of cells near the edge of an image without using some form of correction (edge replication, mirroring, or padding). A benefit of image-based methods is that they do not require cell coordinates, and in principle, orientation could be determined at each pixel within an image, removing the requirement

of pre-determined cell coordinates. An image-only approach could also be used in the Fourier algorithm. However, future work is needed to understand the reliability of the Fourier method using only the retinal image.

As each algorithm accurately defines orientation in ideal mosaics, the primary difference between the algorithms is how each responds to input imprecision. This could directly influence which algorithm is applied. For example, the Fourier algorithm appears to be the most robust to poor signal-to-noise ratio (SNR) and poor cell identification precision. This makes it an ideal candidate for instances where the data reliability is poor. Conversely, in situations where there is good image quality but unreliable cell identification, our results suggest that the Radon algorithm would perform optimally. Finally, in cases where both the image and cell coordinate reliability is excellent, Pum's method would be expected to perform optimally.

Cell orientation has the potential to detect subtle changes in photoreceptor regularity, but there are numerous other aspects of orientation that still need to be examined. Principle among them is the effect of eccentricity on orientation. It has been established that the percentage of six-sided cells increases away from the fovea and peaks at approximately 0.5 degrees before decreasing to foveal levels at 1 degree and beyond (Baraas et al., 2007; Carroll, Kay, Scoles, Dubra, & Lombardo, 2013; Dees et al., 2011; Li & Roorda, 2007; Lombardo, Serrao, et al., 2013). The effect of the percentage of six-sided cells (*e.g.*, by analyzing real mosaics collected beyond 1 degree) was not explored in this manuscript, although we would expect that the orientation of cone photoreceptors would be far less homogenous due to the loss of the hexagonal lattice. Other phenomena that may contribute to the orientation of hexagonal cones as a function of eccentricity are local variance of the cone shape and the compression along the vertical meridian as a consequence of the expansion along the horizontal meridian of the photoreceptor mosaic; the effect of these properties could be explored in future work.

In addition to the effect of eccentricity on orientation, it has not yet been determined how the orientation of a mosaic changes in response to retinal pathology. Nevertheless, the results from each algorithm suggest that the orientation of individual cones is not random, but correlated to their neighbors, consistent with previous observations (Curcio & Sloan, 1992; Pum et al., 1990). Thus, deviations in the expected orientation of neighbors within the cone mosaic could be used as a metric of photoreceptor structure, especially when used as a complement to conventional cone metrics such as cell density and spacing. Indeed, the most commonly used mosaic descriptors are not directionally sensitive and only provide distance measurements derived from cone positions. Measurements of cone regularity, like cell orientation, have the potential to measure a unique aspect of the structure of a photoreceptor mosaic. As the clinical utility of AO devices continues to expand, the development of novel, sensitive metrics are essential to characterizing the human photoreceptor mosaic.

Chapter Five: Automatic detection of modal spacing (Yellott's ring) in adaptive optics scanning light ophthalmoscope images

The contents of chapter five were published during my graduate studies.

Citation

Cooper, R. F., Langlo, C. S., Dubra, A., & Carroll, J. (2013). Automatic detection of modal spacing (Yellott's ring) in adaptive optics scanning light ophthalmoscope images. Ophthalmic & Physiological Optics, 33(4), 540-549.

Contributions

For this chapter, I conceived of and implemented the algorithm featured as part of the publication. Experimental design assistance (to test and refine the algorithm) was provided by Christopher S. Langlo, Dr. Alfredo Dubra, and Dr. Carroll. In addition to the algorithm design, I performed the analyses, and wrote the publication and figures, with Dr. Carroll and Dr. Dubra providing editing assistance.

Introduction

Adaptive optics (AO) retinal imaging systems permit direct visualization of the rod and cone photoreceptor mosaics (Dubra et al., 2011; Liang et al., 1997; Rossi et al., 2011). Central to the clinical application of this imaging capability is having robust methods for analyzing images of the photoreceptor mosaic, and there are a number of well-defined metrics derived for use on histological specimens that have been translated to the analysis of AO retinal images (Cook, 1996; Curcio, Sloan, & Meyers, 1989; Rodieck, 1991). Currently used metrics within the ophthalmic AO community require identification of cells within the region of interest, and include photoreceptor density (Carroll et al., 2004), Voronoi-based analyses of mosaic geometry (Baraas et al., 2007; Carroll, Rossi, et al., 2010), the histogram-based density recovery profile (Roorda et al., 2001), and the calculation of average inter-cell spacing (Rossi & Roorda, 2010). Given the expanding clinical applications for AO imaging (Duncan et al., 2007; Godara, Cooper, et al., 2012; Han et al., 2012), and the emergence of clinical prototypes (Fay, Faridi, Garg, & Pennesi, 2012; Morgan, Chung, Nozato, Maguire, & Bennett, 2012), it is important that the relative merit of these metrics is objectively demonstrated to facilitate their use in comparative and prospective clinical studies.

Impeding progress in these efforts is the subjectivity of current cone identification processes in AO retinal images. Garrioch *et al.* recently quantified the repeatability of an automated algorithm for identifying individual cone photoreceptors (Garrioch et al., 2012), though similar inspection of other approaches is lacking. Metrics derived from directly counting the cells work well in images where every cell is resolvable; however in images of lower quality where some cells may not be visible, the accuracy of these methods could be significantly diminished. It is possible to avoid cone identification altogether by examining images of the photoreceptor mosaic in the frequency domain.

Originally observed by Yellott (Yellott, 1982, 1983), the Fourier transform of a cone mosaic image has an annular appearance. As described previously, and as adopted here, the radius of this annulus corresponds to the modal frequency of the cone mosaic, and the reciprocal of this modal frequency is defined as the modal spacing of the cones in the original image (Coletta & Williams, 1987). Numerous investigators have used this relationship to extract estimates of cone spacing from images of the living cone mosaic obtained using laser interferometry (Artal & Navarro, 1989), fundus photography (Miller et al., 1996), and AO fundus photography (Liang et al., 1997). Derivation of an estimate of photoreceptor density from such modal spacing values requires some assumptions about the underlying geometry of the mosaic. Here, we use the commonly adopted assumption that the human cone mosaic is arranged in a regular triangular lattice (Coletta & Williams, 1987; Williams & Coletta, 1987). Extraction of the modal frequency has been a highly subjective process, thus limiting the widespread implementation of the technique. Here we propose an algorithm for estimating modal cone spacing (and from this, cone density) from images of the photoreceptor mosaic using automated identification of the modal frequency in the power spectrum. We validate this algorithm against direct-count estimates of density using images of the normal parafoveal cone mosaic. To provide further assessment of the algorithm, we examined normal images of the perifoveal rod and cone mosaics as well as images of disrupted parafoveal cone mosaics from individuals with retinal disease.

Methods

Human Subjects

All experiments were performed in accordance with the Declaration of Helsinki and study protocols were approved by the institutional research boards at the Medical College of

Wisconsin and Marquette University. Parafoveal images from twenty-one subjects (thirteen males and eight females, age 25.9 ± 6.5 years) with no vision-limiting pathology were used from a previous study (Garrioch et al., 2012). Additionally, four subjects with retinal disease were recruited including a subject with retinitis pigmentosa (female, age 46 years), a subject with red-green color blindness caused by an LVAVA mutation (male, age 15 years) (Neitz et al., 2011), a subject with red-green color blindness caused by an LIAVA mutation (male, age 36 years) (Carroll et al., 2004), and a subject with photoreceptor disruption with an unknown etiology (male, age 11 years). Two female subjects with normal vision (ages 23 and 27 years) were also recruited for this study, from which images of the perifoveal photoreceptor mosaic were acquired. All subjects provided written informed consent after explanation of the nature and risks of the study. Axial length measurements were obtained using a Zeiss IOL Master (Carl Zeiss, Oberkochen, Germany).

Photoreceptor Image Acquisition and Processing

A previously described AO scanning light ophthalmoscope (AOSLO) was used to image each subject's photoreceptor mosaic (Dubra & Sulai, 2011). The wavelength of the super luminescent diode used for retinal imaging was 775 nm. The system's pupil used for imaging was 7.75 mm in diameter and we estimate that the confocal pinhole of our system was about one Airy disk diameter. Image sequences of 150 frames were recorded at each retinal location, and the retinal area scanned was 0.96×0.96°. Intra-frame distortion due to the sinusoidal motion of the resonant optical scanner was estimated from images of a Ronchi ruling and removed by resampling each frame of the raw video over a square pixel grid. After desinusoiding, a reference frame with low distortion due to eye motion was manually selected from each image sequence for

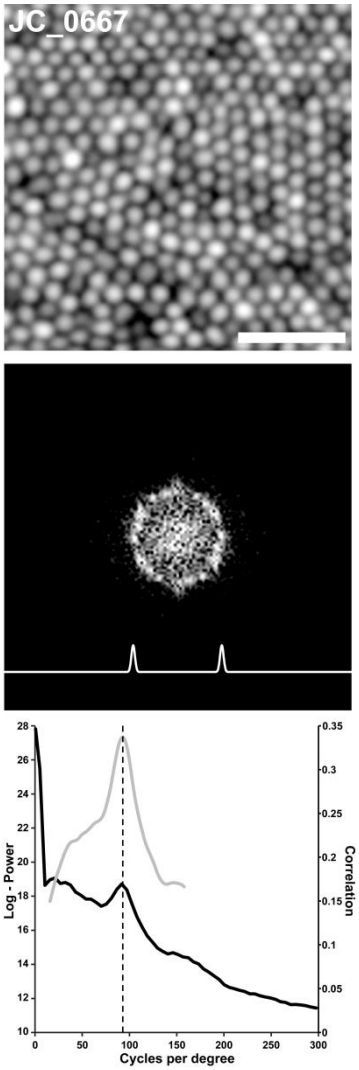

Figure 5.1: Extracting cone density from the power spectrum. Shown is an exemplar parafoveal cone photoreceptor image. Scale bar is 20 μm. The middle panel shows the 2D log10-power spectrum of the photoreceptor image in the top panel. Due to the highly regular mosaic in the image, the hexagonal packing of the photoreceptors is visible in the Fourier domain as a ring with peaks in a hexagonal pattern. The trace shown below the power spectrum ring represents the cross-section of the template whose radius was adjusted to best fit the power spectrum. The lower panel shows a plot of the radial average of the log-power spectrum (solid black line) as well as a plot of the correlation function (solid gray line). The vertical dashed line indicates the peak of the correlation function automatically determined by the algorithm, which corresponds well to the visible peak in the radial average of the power spectrum. This spacing corresponds to a density of 90,332 cones/mm^2, which is close to the direct count value for this mosaic (86,344 cones/mm^2).

subsequent registration using a strip-based registration method (Dubra & Harvey, 2010).

Each frame was divided into strips and each strip was registered against the reference

frame by finding the relative position that maximizes the normalized cross-correlation between them (Dubra & Harvey, 2010). The registered frames were then averaged to create a single high signal-to-noise ratio image for each image sequence.

As mentioned above, two datasets were used in this study. The normative dataset from Garrioch *et al.* (2012) consisted of images from four separate locations approximately 0.65° from center of fixation. The four locations were imaged in a random order, with the subject remaining positioned on the chin/forehead rest for each set of image sequences. This procedure was repeated 10 times for each subject, with a short break in between each set, resulting in a total of 840 images (21 subjects, four locations per subject, 10 images per location). Garrioch *et al.* analyzed the central 55 × 55 μm portion of each image, and we did the same. Due to individual differences in ocular magnification, the number of image pixels subtended by the 55 × 55 μm sampling window was variable across subjects (ranging from 120 to 148 pixels). The second dataset included images collected from four subjects with retinal disease at approximately 0.65° from center of fixation and perifoveal images (about 10° temporal to fixation) from the two normal female subjects. For analysis, all photoreceptor images were transformed to a logarithmic intensity scale.

Detecting Yellott's Ring

The proposed algorithm is based on feature extraction and detection using pattern matching. To begin, the photoreceptor image was transformed into this using the Discrete Fourier Transform (DFT), and this image was resampled to five times its size using bi-cubic interpolation (Liang et al., 1997).

The power spectrum was calculated as the $\log_{10}$ of the square of the absolute value of the DFT image (**Figure 5.1**). Next, we created an annular template with a Gaussian profile centered on the power spectrum with a standard deviation of 7.5 cycles

per degree; the cross-section is shown in **Figure 5.1**. The cross-sectional width of Yellott's ring varies, in part, as a function of irregularity in packing geometry – the power spectrum from more irregularly packed mosaics will have a ring with a wider cross-sectional profile than that from more uniformly packed mosaics. Looking at previously published normative cone spacing values (Garrioch et al., 2012), irregularities in cone spacing would correspond to a standard deviation of about 5.5 cycles per degree in the frequency domain. As other factors, such as local variation in iso-orientation contours will also broaden the cross-sectional profile, we relied on empirical observations (Cooper, Rha, Dubra, & Carroll, 2011) to set the standard deviation at 7.5 cycles per degree. While this parameter is adjustable, it was fixed for the present analysis.

Normalized cross-correlation using Pearson's correlation coefficient was performed between the power spectrum and annuli of varying sizes to maximize the correlation between the pattern and the image. Considering physiological limits of the axial length of the human eye (Oyster, 1999), as well as previously reported rod and cone density values for normal eyes (Curcio et al., 1990), the radius of the annulus was allowed to vary from 15 to 160 cycles per degree, enabling detection of all physiologically plausible cell spacing values for this cohort.

Intrasession Repeatability of Power Spectrum Derived Density Estimates

In order to assess the intrasession repeatability of cone density estimates derived with the algorithm, we assessed the power-spectrum derived cone density for all 840 normal parafoveal images. The power spectrum-derived spacing values were converted to density, D, in cells per mm^2, using the approximation described in equation 5.1 (below), where s is the modal spacing in cycles per degree and M is the RMF in mm per degree (Coletta & Williams, 1987). It is important to note that this assumes the cells are arranged in a triangular crystalline mosaic. For a 24 mm axial length eye, the

magnification is 0.291 mm per degree, and we estimated the magnification for each image using a linear scaling based on each subject's measured axial length.

$$D = \frac{\sqrt{3}}{2\left(\frac{m}{s}\right)^2} \quad \textbf{(Eq. 5.1)}$$

The repeatability measures were based on the within-subject standard deviation, s_w, as described by Bland and Altman (1996). To estimate s_w, we first calculated the standard deviation of the repeated measures for each subject and then squared this to get the variance for each subject (Bland & Altman, 1996). The square root of the average variance for the 84 image sets (four per subject, 21 subjects) gives s_w, and the repeatability is defined as s_w multiplied by 2.77. The 95% confidence interval for repeatability is given by equation 5.2, where n is the number of subjects and m is the number of observations for each subject (Patel, Chen, Ikeji, & Tufail, 2011).

$$\text{95\% Confidence Interval} = 1.96\left(\frac{s_w}{\sqrt{\left(2n(m-1)\right)}}\right) \quad \textbf{(Eq. 5.2)}$$

We compared these repeatability estimates to those previously reported for an automated cone counting algorithm (automated and automated with manual correction) (Garrioch et al., 2012). Intrasession repeatability was expressed in cones/mm^2 as well as a percentage of the mean value.

Assessing the Agreement Between Direct Count and Power Spectrum Derived Density Estimates

To validate the performance of this method, we examined the agreement between direct count density estimates and those derived from the power-spectrum method in the image set previously published by Garrioch *et al.* In this previous study, the direct-count density was measured over the central 55 × 55 μm portion of each image, and was obtained using the automated cone counting algorithm with manual correction. As we

have repeated measures for both the direct count algorithm and the power-spectrum method, we can utilize all of the data to compare the agreement between the methods. While the details of this statistical approach have been provided in detail (Bland & Altman, 1986, 1999), we provide a brief overview here for this particular analysis. First, the average within-subject standard deviation is calculated for each method alone, as described above, denoted s^2_{xw} and s^2_{yw}. The mean difference between within-subject means is $\overline{D} = \overline{X} + \overline{Y}$. The variance of the differences between the within-subject means is given as $s^2_{\overline{d}}$. The number of observations on each subject by each method is given by m_x and m_y. The adjusted variance of differences is then given by equation 5.3.

$$\hat{\sigma}^2_{\overline{d}} = s^2_{\overline{d}} + \left(1 - \frac{1}{m_x}\right)s^2_{xw} + \left(1 - \frac{1}{m_y}\right)s^2_{yw} \qquad \textbf{(Eq. 5.3)}$$

The 95% limits of agreement between the two methods is given by $\overline{D} - 1.96\sqrt{\hat{\sigma}^2_{\overline{d}}}$ and $\overline{D} + 1.96\sqrt{\hat{\sigma}^2_{\overline{d}}}$. This comparison can be represented using a Bland-Altman plot, which plots the difference between the power spectrum derived density estimate and the direct count density against the mean of the two values, $(\overline{X} + \overline{Y})/2$. We also examined the agreement between the power spectrum method and direct count method in examples of non-uniform mosaics – parafoveal images in four patients with retinal pathology and two perifoveal images containing both rod and cone photoreceptors.

Results

Intrasession repeatability of power-spectrum derived estimates of cone density

We found that the algorithm had an average intrasession repeatability of 4953 cones/mm^2 (95% CI = 4,772 – 5,133 cones/mm^2). This corresponds to an intrasession repeatability of 6.7%. This means that the difference between any two measurements on

Table 5.1: Intrasession repeatability of cone density measurements derived from the power spectrum spacing

Fixation location	Mean Density (cones/mm^2)	Measurement error (cones/mm^2)	Repeatability (cones/mm^2)	95% CI for repeatability (cones/mm^2)	Repeatability (%)	95% CI for repeatability (%)
Bottom left	72,712	2,278	3,219	3,102-3,336	4.4	4.3-4.6
Bottom right	71,555	2,902	4,102	3,953-4,251	5.7	5.5-5.9
Top left	77,224	3,479	4,917	4,739-5,096	6.4	6.1-6.6
Top right	74,129	5,358	7,573	7,297-7,849	10.2	9.8-10.6
Average	**73,905**	**3,504**	**4,953**	**4,772-5,133**	**6.7**	**6.4-6.9**

the same subject would be less than 4,953 cones/mm^2 (or 6.7%) for 95% of observations with this algorithm. The measurement error, or expected difference between a measurement and the true value (cones/area), was calculated to be 3,504 cones/mm^2. These statistics are summarized in **Table 5.1**. This intrasession repeatability is comparable to that reported by Garrioch *et al.* who assessed the repeatability of cone density measurements using a fully automated direct count algorithm(Garrioch et al., 2012).

Examination of their data reveals a repeatability of 4,829 cones/mm^2 (95% CI = 4,653 – 5,005 cones/mm^2), or 6.4%. However, as shown by Garrioch *et al.* (2012), the use of manual correction of the automated density estimates resulted in improved repeatability of 2,123 cones/mm^2 (95% CI = 2,046 – 2,200 cones/mm^2), or 2.7%.

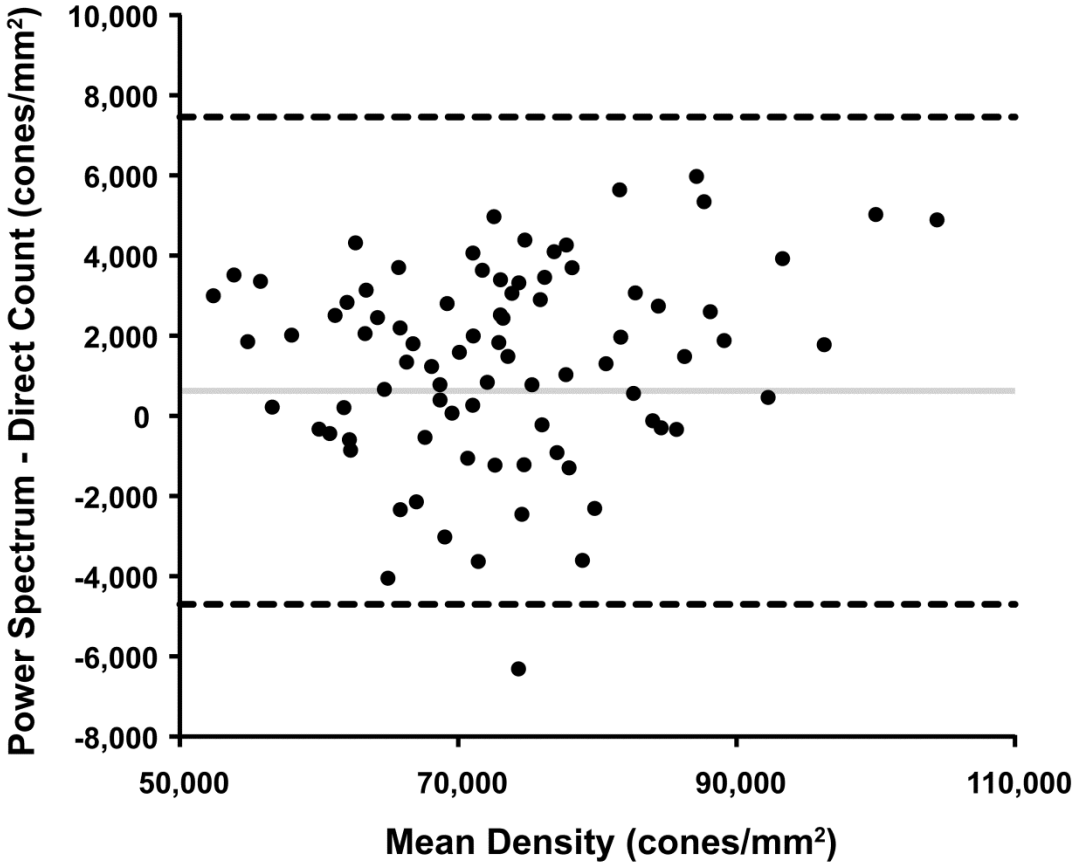

Figure 5.2: A Bland-Altman plot of cone density derived from the direct count algorithm (with manual correction) and from the power-spectrum algorithm presented here. Solid lines: average mean difference (1,377 cones/mm^2); dotted lines: 95% confidence limits.

Comparison of Direct Count and Power-Spectrum-Derived Estimates of Density

Despite having worse repeatability, the average cone density from the power-spectrum derived method (73,905 cones/mm^2, **Table 5.1**) was similar to the average cone density from the direct count with manual correction method (72,528 cones/mm^2). Both of these values are greater than the average cone density reported for this data set using the fully automated direct count algorithm (68,535 cones/mm^2)(Garrioch et al., 2012). To quantify the agreement between the cone density from the power-spectrum

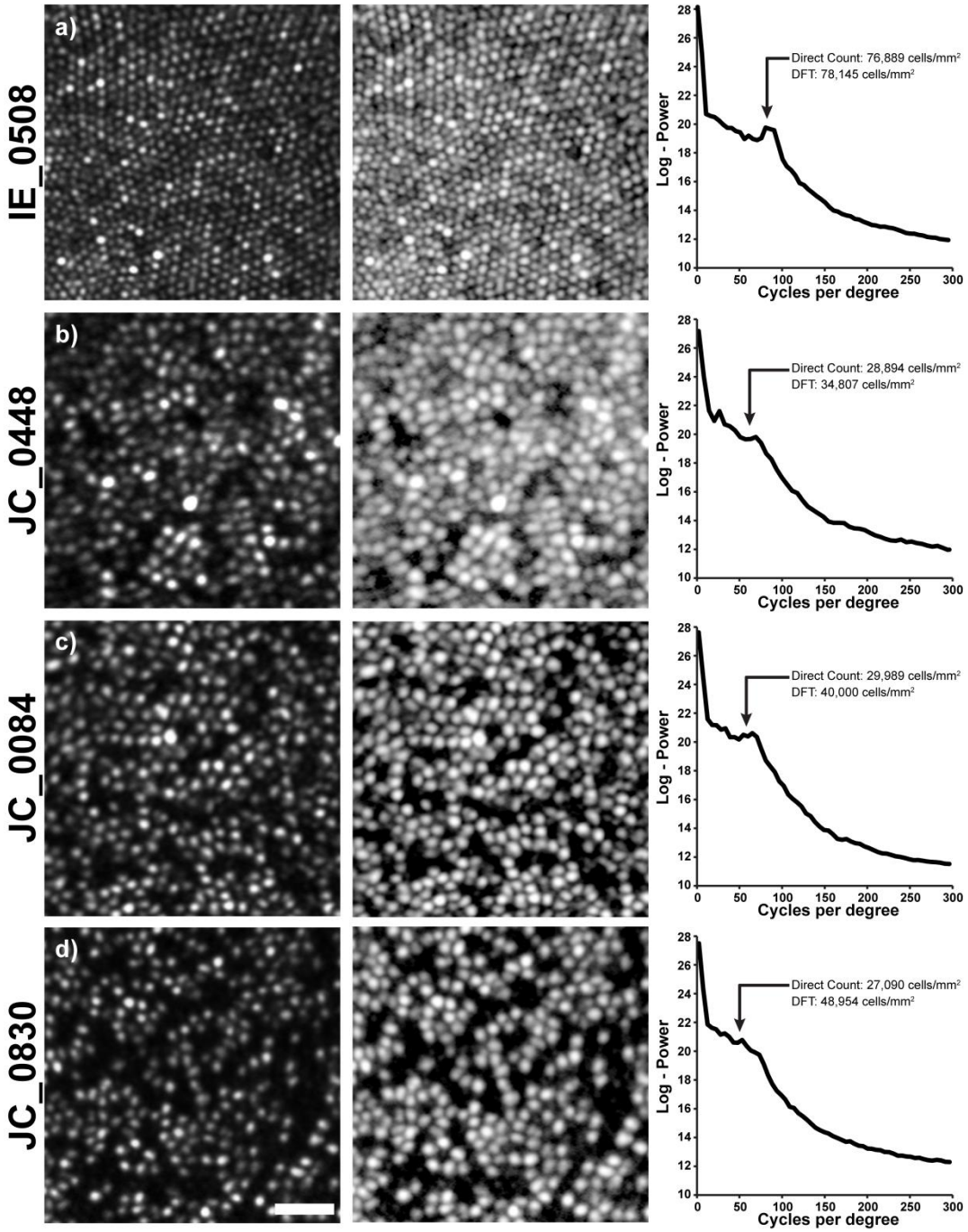

Figure 5.3: We examined power-spectrum derived estimates of cone density in patients with various pathologies. Shown in the left column are images from a subject with retinitis pigmentosa (IE_0508), a subject with red-green color blindness caused by an LVAVA mutation (JC_0448)(Neitz et al., 2011), a subject with red-green color blindness caused by an LIAVA mutation (JC_0084)(Carroll, Neitz, Hofer, Neitz, & Williams, 2004), and a subject with photoreceptor disruption with an unknown etiology(JC_0830). Scale bar is 20 μm. Shown in the middle column is the 2D log10-power spectrum for each image, with the radial average of the 2D log-power spectrum shown in the right panel. As can be seen in the cone density values, there is disagreement in the mosaics with disrupted cone mosaics, and the power-spectrum derived density overestimates the actual density of the image.

derived method and that from the direct count with manual correction method, we created a Bland-Altman plot (**Figure 5.2**). In the normative subset of images from Garrioch *et al.* we found a mean difference, $\overline{D}$, of less than 2%, with the power spectrum-derived density estimates being on average 1,377 cones/mm^2 greater than the direct-count measurements (**Figure 5.2**). As this is comparable to the measurement error of either method, we consider this to represent good agreement between the methods. The adjusted variance of differences, $\hat{\sigma}_{\frac{2}{d}}$, was calculated using equation 3 and the 95% limits of agreement were found to be ± 6,079 cones/mm^2, and are represented by the dashed lines in **Figure 5.2**. Overall, the differences do not vary systematically over the range of cone density measurements.

We next sought to assess the agreement between these methods in individuals with retinal disease. In a patient with retinitis pigmentosa having a complete and contiguous parafoveal cone mosaic (**Figure 5.3**, IE_0508), there is good agreement (76,889 cones/mm^2 for direct count vs 78,145 cones/mm^2 for power-spectrum derived). However, in patients with patchy disruption of the cone mosaic (JC_0448, JC_0084, JC_0830) we observed worse agreement with the power-spectrum derived value overestimating the direct-count density by 20-81% (**Figure 5.3**). As the conversion of modal spacing in the power spectrum to density assumes a complete mosaic, this insensitivity to cell loss would invariably result in overestimation of the real density.

As the resolution of ophthalmic AO instruments has improved, it is now possible to resolve rods as well as cones in images of the perifoveal photoreceptor mosaic (Doble et al., 2011; Dubra et al., 2011; Merino et al., 2011). The presence of two distinct mosaics within a single image also compromises the accuracy of power-spectrum derived estimates of density. As shown in **Figure 5.4**, density estimates based on the cone and rod modal spacing detected by the algorithm overestimate the direct count

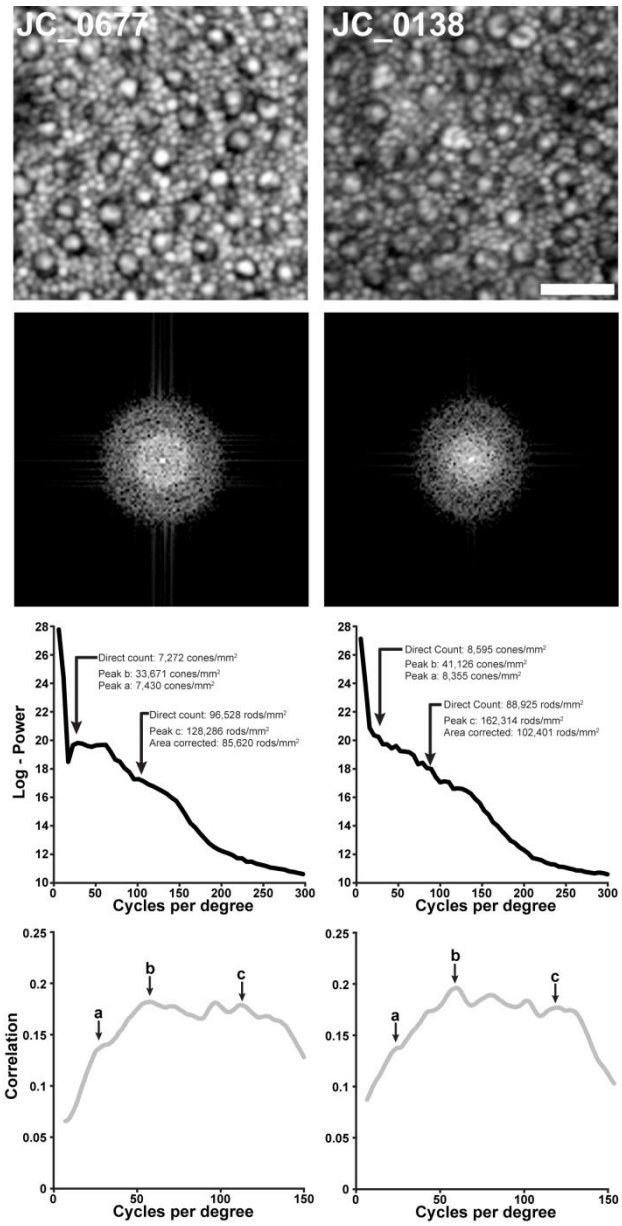

Figure 5.4: Estimating density in images containing rod and cone photoreceptors. Shown are two retinal images from about 10 degrees temporal to fixation (scale bar is 20 μm), along with the 2D $\log_{10}$-power spectrum for each image. In these images, the automated power-spectrum derived density estimates overestimate the direct count density values for both the cone and rod mosaics. The presumed cone peak in the correlation plot (peak b) actually corresponds to the size of the cones themselves, not their modal spacing. The subtle peak on the ascending limb of the correlation plot (peak a) corresponds to cone spacing, using this spacing to estimate density yields values in better agreement with the direct count estimates. Using this estimate of cone density together with an estimate of the area of each cone from peak b and the modal spacing of the rod mosaic (peak c), it is possible to estimate the number of rods displaced by the cone mosaic and derive a corrected estimate of rod density. This approach yields rod density values in better agreement with the direct count values.

densities. However in both cases, the power spectrum contains information that can be used to correct the density estimates. In these images, most perifoveal cones have a bright central reflective core surrounded by a dark ring. We previously hypothesized that this dark ring represented the extent of the cone inner segment (Genead et al., 2011). It is this aspect of the cone profile that generates the dominant low frequency structure detected by the algorithm (peak b in **Figure 5.4**). The spatial frequency of this peak in the two mosaics in **Figure 5.4** corresponds to a structure of 7.5 μm and 7.6 μm in diameter, consistent with previous histological estimates of cone inner segment diameter (about 7.8 μm) at this eccentricity for the temporal retina (Packer, Hendrickson, & Curcio, 1989). There is a second weaker peak in the power spectrum that can be seen in the plot of the correlation function (peak a in **Figure 5.4**). This manually identified peak corresponds to a cone density of 7,430 cones/mm^2 and 8,355 cones/mm^2 for the two mosaics in **Figure 5.4**, much closer to the direct count estimates of 7,272 cones/mm^2 and 8,595 cones/mm^2, respectively.

On first glance, the rod density estimates calculated from the power-spectrum derived spacing are 1.5 times greater than the direct count density (**Figure 5.4**). However, as stated in the methods, the derivation of an estimate of density from the modal spacing from the power spectrum assumes that the objects in the image are contiguous and periodic. In these perifoveal images, the cones disrupt the contiguity of the rod mosaic and thus the area occupied by the cones needs to be corrected for in order to extract an accurate estimate of rod density from the modal spacing. Using the cone density estimate derived from the cone spacing (peak a in **Figure 5.4**) and an estimate of cone area based on the cone size (peak b in **Figure 5.4**), together with the estimated rod spacing from the power spectrum (peak c in **Figure 5.4**), we can estimate the number of rods displaced by the cones in the image. This provides a corrected power-spectrum derived estimate of 85,620 rods/mm^2 and 102,401 rods/mm^2 which is in

better agreement with the direct count estimates of 96,528 rods/mm^2 and 88,925 rods/mm^2, respectively. While the need for manual selection of the additional peaks in these power spectra severely limits the clinical utility of this approach, our analysis provides a good starting point to examine the interplay between the rod and cone sub-mosaics in the frequency domain image.

Discussion

We developed and tested an automated algorithm for extracting estimates of cone and rod density from the power spectrum. In AOSLO images of the normal parafoveal cone mosaic, the power spectrum-derived density estimates showed good agreement with direct-count estimates (an average bias of 1,377 cones/mm^2, or 1.9%), and the algorithm's average repeatability was 6.7%. This repeatability is comparable to that reported for a fully automated direct count algorithm, however the power-spectrum derived density estimates are actually closer to the true value (direct count + manual correction) than are the estimates obtained by the fully automated direct count algorithm. Of course in high-quality images where every cell is visible, a direct count approach would be preferred as it offers the opportunity to assess additional metrics such as the packing geometry of the mosaic, which requires a 2D map of the cell positions.

However, in images where not every cell is visible or that are of generally poorer quality, direct counting may prove more unreliable. Thus the power spectrum method may in fact be preferred for deriving estimates of cell density. Examination of additional datasets from other AO devices is needed to test this concept. As illustrated in **Figure 5.3**, this robustness (i.e., insensitivity to not every cell being visible) actually becomes a liability when analyzing mosaics from diseased retinae with cells that have degenerated. This would greatly diminish the clinical utility of the power spectrum method.

There are additional limitations to the method proposed here. First, the estimation of density from the power spectrum spacing relies on the assumption of a crystalline triangular mosaic (Coletta & Williams, 1987). While in normal mosaics this presumption of regularity holds (Baraas et al., 2007; Carroll, Rossi, et al., 2010; Curcio & Sloan, 1992; Li & Roorda, 2007), it fails in mosaics of patients with retinal degeneration. As shown in **Figure 5.3**, this would limit the accuracy of density estimates from disrupted mosaics. A second limitation is that the power spectrum contains information about the object profile as well as the spacing of the objects in the image. Given that the cone profile varies with eccentricity, focal plane, and with disease (Carroll et al., 2012; Genead et al., 2011; Godara, Cooper, et al., 2012; Hansen et al., 2013), disentangling the contribution of the cone profile will be difficult. However, it was recently shown that the cone profile can be manipulated through the use of annular pupils (Sulai & Dubra, 2012), and this may provide a way to tease apart the relative impact of the cone profile on the power spectrum.

Given the continued improvements in retinal image quality combined with development of additional algorithms for automatically identifying photoreceptors in AO retinal images, the utility of the power spectrum method may not be in computing cell density. However, the agreement between the power-spectrum derived density and that from an automated algorithm in the complete, continuous mosaics analyzed here may offer a sort of screening tool for automatically examining images in a clinical setting. For example, if used in conjunction with an automated cone identification algorithm, the power spectrum method could be used to flag images that require manual inspection, based on the magnitude of disagreement between the methods. Alternatively, the power spectrum method could be integrated into future algorithms to instruct them as to the modal spacing of the objects to be detected.

While this study provides a detailed examination of the relationship between two particular metrics for describing the photoreceptor mosaic, similar analyses of alternative methods for objectively characterizing the photoreceptor mosaic are needed. As clinical applications of AO retinal imaging expand, it is important to understand the information provided by various mosaic metrics to converge on approaches that are both clinically practical and relevant.

Chapter Six: Effects of intra-frame distortion on measures of cone mosaic geometry from adaptive optics scanning light ophthalmoscopy

Chapter six was submitted during my graduate studies.

Citation

Cooper, R. F., Sulai Y. N., Dubis, A. M., Chui, T. Y., Rosen, R. B., Michaelides, M., Dubra, A.,& Carroll, J. (2015) Effects of intra-frame distortion on measures of cone mosaic geometry from adaptive optics scanning light ophthalmoscopy. Translational Vision Science & Technology. *Submitted.*

Contributions

For this chapter, experimental design assistance was provided by Dr. Yusufu Sulai, Dr. Alfredo Dubra, and Dr. Joseph Carroll. The imaging support was provided from the Moorfields Eye Hospital by Drs. Adam Dubis and Michel Michaelides, and the New York Eye and Ear Infirmary by Drs. Toco Chui and Richard Rosen. I performed the image acquisition, data processing, image/coordinate analyses, and wrote the publication and figures. Dr. Carroll and Dr. Dubra provided editing assistance. Imaging support was provided by Nadim Choudhury, Mara Goldberg, Brian Higgins, Christopher S. Langlo, Nikhil Menon, Erika Phillips, Phyllis Summerfelt, and Melissa A. Wilk.

Introduction

Adaptive optics (AO) ophthalmoscopy enables high-resolution imaging of the human retina *in vivo* (Bedggood & Metha, 2012; Dubra & Sulai, 2011; Liang et al., 1997; Miller et al., 2011; Roorda et al., 2006). AO was first incorporated to a custom fundus camera (Liang et al., 1997), permitting the visualization of cone photoreceptors outside the foveal center (Baraas et al., 2007; Bedggood & Metha, 2012; Dees et al., 2011; Liang et al., 1997). More recently, AO was added to a confocal scanning laser ophthalmoscope (cSLO); enhancing the axial sectioning of cSLOs as well as providing high lateral resolution (Roorda et al., 2002). Similarly, adaptive optics scanning light ophthalmoscopes (AOSLO) allow the visualization of microscopic retinal structures, including foveal cones (Dubra et al., 2011; Wilk et al., 2014; Zhang, 2015) and rods(Cooper, Dubis, et al., 2011; Dubra et al., 2011; Merino et al., 2011). AO can also be applied to optical coherence tomography (OCT), combining OCT's excellent axial resolution with the enhanced lateral resolution from AO. This enables the extraction of high-resolution volumetric data consisting of symmetric voxels (3x3x3 microns), and the visualization of weakly reflective structures in the retina (Hermann et al., 2004; Kocaoglu, Lee, et al., 2011; Merino, Dainty, Bradu, & Podoleanu, 2006; Miller et al., 2011; Mujat et al., 2010; Pircher, Zawadzki, Evans, Werner, & Hitzenberger, 2008; Zawadzki et al., 2008).

Regardless of the AO imaging modality used, analysis of images of the photoreceptor mosaic often includes extraction of measurements that describe the geometry of the cone mosaic (Baraas et al., 2007; Dees et al., 2011; Dubra et al., 2011; Duncan et al., 2007; Rossi et al., 2011). However, in (point or line) scanning ophthalmoscopes the image pixels are recorded sequentially, rather than simultaneously as in fundus ophthalmoscopes. Given the relatively low frame rate (<30Hz) and the high

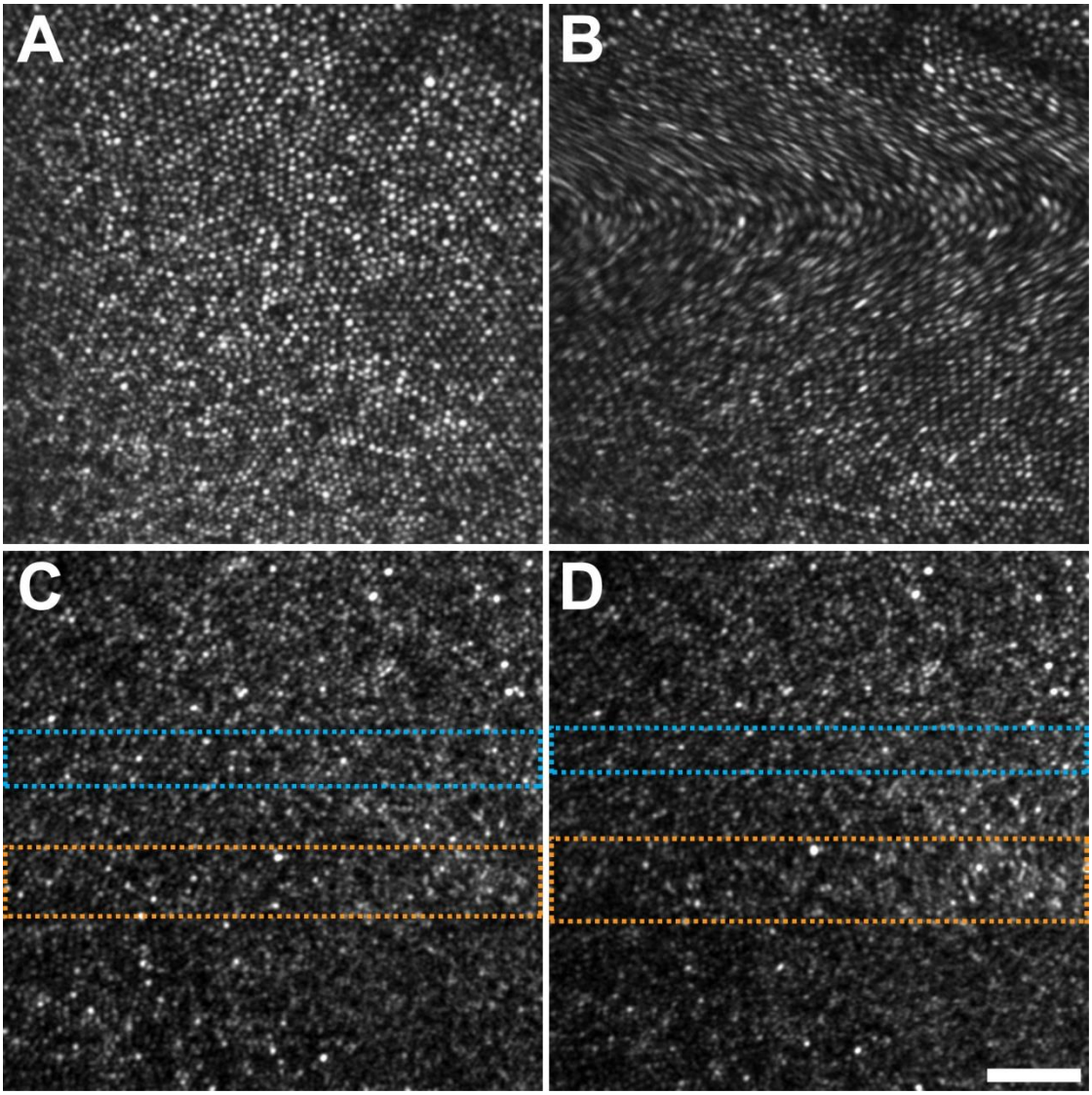

Figure 6.1: AOSLO images containing different quantities of distortion. (A) and (B) are AOSLO images from the same retinal location; however, (A) was considered minimally distorted by an expert observer (RFC), while (B) contained too much distortion to be usable for analysis. While some forms of intraframe distortion are easily discernable, as between (A) and (B), this distortion is not always obvious. (C) and (D) are considered minimally distorted reference frames, however, residual distortion exists within both frames as either a compression (cyan box), or expansion (orange box) of the image. Scale bar is 50 μm.

magnification of current AO scanning ophthalmoscopes (~1°), even the involuntary eye motion in a healthy subject can cause substantial image distortion (local shear and compression/expansion). In AOSLO, distortions from eye motion can be mitigated by registration (Dubra & Harvey, 2010; Vogel, Arathorn, Roorda, & Parker, 2006) and eye

tracking (Arathorn et al., 2007; Sheehy et al., 2012) methods, in conjunction with the selection of a minimally distorted reference (or template) image. However, even an AOSLO image that appears distortionless still contains residual distortion (**Figure 6.1A,C**), potentially compromising the quantitative analysis of retinal structures.

Quantifying the impact of intra-frame distortion on measurements of photoreceptor arrangement is therefore essential to understanding the precision of such measurements. Here we examined the effect of intra-frame distortion on metrics of cone mosaic geometry derived from AOSLO images using two approaches. First, we evaluated the variability in image metrics obtained when utilizing different reference frames (selected by a single expert observer) from within a single AOSLO image sequence to generate a final image for analysis. Second, we compared AOSLO-derived measurements to those from "distortionless" AO-fundus images of the same subject to assess the anatomical accuracy of AOSLO images. These data provide important insight into possible limitations on the sensitivity of AOSLO-derived image metrics that should be taken into consideration when making longitudinal measurements of the cone mosaic.

Methods

Human Subjects

This research followed the tenets of the Declaration of Helsinki, and was approved by the institutional research boards at the Medical College of Wisconsin (MCW), Marquette University, Moorfields Eye Hospital (MEH), and the New York Eye and Ear Infirmary (NYEEI). Twenty-nine subjects were recruited for this study (19 at MCW, five at MEH, five at NYEEI). Subjects provided informed consent after the nature and possible consequences of the study were explained. Axial length measurements were obtained

from each subject using an IOL Master (Carl Zeiss Meditec, Dublin, CA) and were used in conjunction with a simplified Gullstrand II model to convert from degrees of visual angle to retinal distance in microns.

Imaging the Photoreceptor Mosaic

Images of the photoreceptor mosaic were obtained from subjects using a previously described AOSLO (Dubra & Sulai, 2011) at three different sites (MCW, NYEEI, and MEH), and a newly-constructed AO fundus camera (**Figure 2.2**).

Static Image Distortion

In all AOSLO images, a sinusoidal static distortion was present in each image due to the properties of the horizontal resonance scanner. This distortion has been characterized and corrected in previous work (Dubra & Sulai, 2011; Roorda et al., 2002), and was removed by resampling each frame of the AOSLO image sequence using a 118.1 line/mm Ronchi ruling.

To examine residual static distortion in both these “desinusoided” AOSLO images and the AO fundus images, we acquired images of a custom glass-embedded two micron grid with an eight micron pitch (**Figure 6.2A,C**) by placing the grid at the focal plane of a model eye with a 19 mm focal length lens, and closed the AO loop to reduce residual system distortion. We then compared images of the grid to a derived ideal grid. We determined the center of each grid square using a previously defined semi-automatic cone counting algorithm (Garrioch et al., 2012). To derive the ideal grid, we used the image grid coordinates contained from the central 5x5 grids to determine the average inter-grid distance. An ideal coordinate grid with a pitch equivalent to the inter-grid distance was created and aligned to the most central image grid square

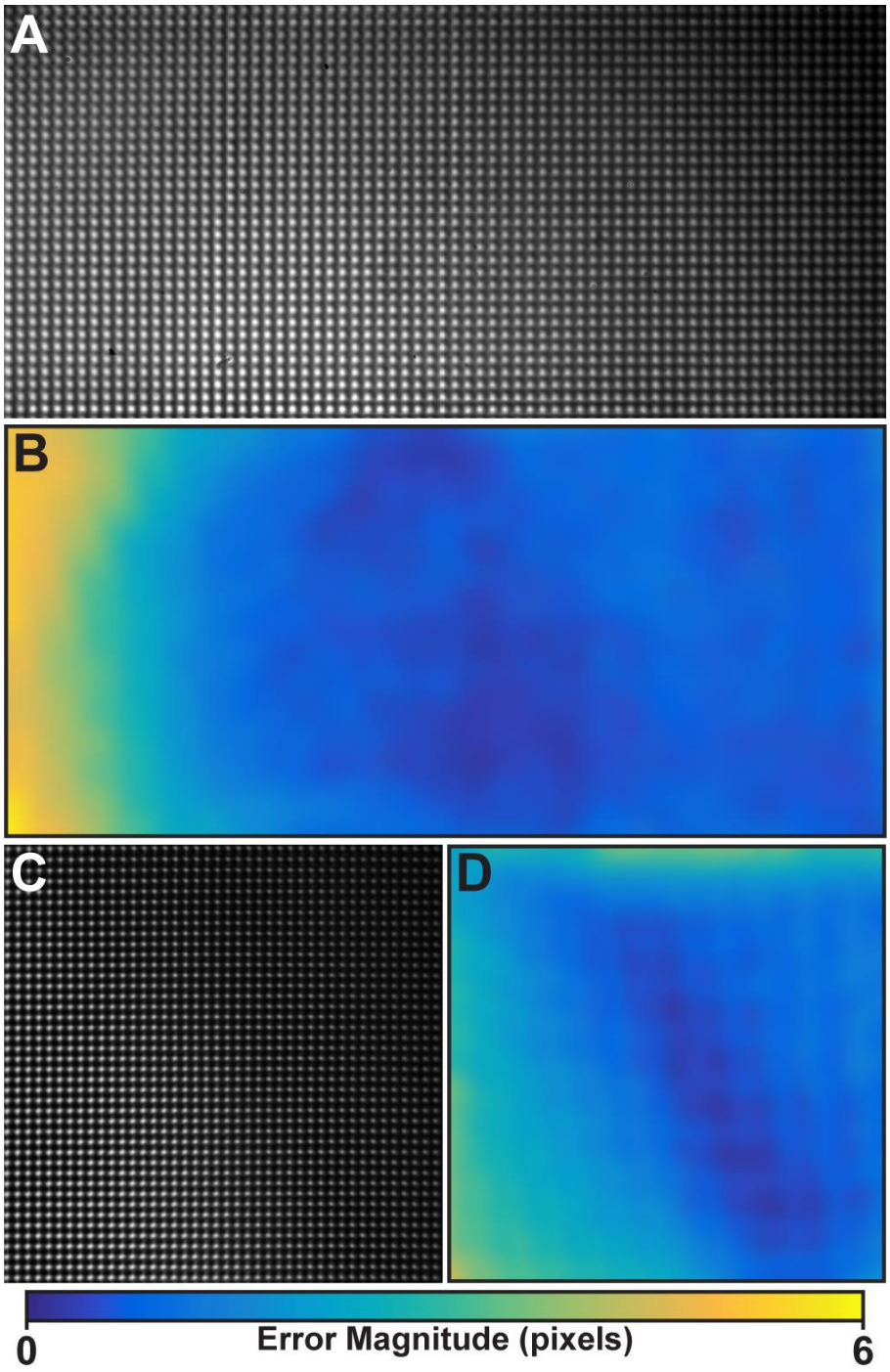

Figure 6.2: Static system distortion in AO fundus camera and AOSLO images. Qualitatively, images obtained of a 2-dimensional grid using an AO fundus camera (A) and AOSLO (C) appear undistorted. Quantitatively, residual distortions exist within each image; (B) and (D) illustrate the residual distortions that are present in the AO fundus image (B) and the AOSLO image (D). In order to correct these localized distortions, the images must be digitally resampled. Warmer colors correspond to high residual distortion (max: 6.1 pixels), while cooler colors correspond to low residual distortion (min: 0 pixels).

coordinates. Image grid and actual grid coordinates were paired by finding the nearest image grid neighbor coordinate for each ideal coordinate. A heat map was created from the distance between each ideal and image coordinate pair (**Figure 6.2B,D**). Overall distortion was defined as the root mean squared deviation from the perfect grid across all coordinates.

AOSLO Image Distortion from Eye Motion

To examine the distortion induced by normal involuntary microsaccades, image sequences were obtained from 20 subjects at 1.0°, 2.0°, and 5.0° temporal (1T, 2T, and 5T) from the center of fixation. Within each sequence, a reference frame judged to have minimal intra-frame distortion was selected by comparing consecutive frames for minimal translation and distortion. The remaining frames were aligned to the reference frame using a previously described strip-registration method (Dubra & Harvey, 2010). The 50 frames with the highest cross-correlation were averaged to produce a single image for that reference frame. A total of 10 reference frames were chosen in this manner for each AOSLO image sequence, by a single expert observer (RFC). From the resultant 10 images, a *master* image with minimal visible distortion was selected, and the remaining nine *slave* images were coarsely aligned to this image by repositioning them using i2k Retina (DualAlign LLC; Clifton Park, NY). All aligned images were cropped to 0.55 degrees. These cropped slave images were then finely aligned to the cropped master image using strip-registration (Dubra & Harvey, 2010). The strip-registration transformation applied to each image was recorded and converted to a pixel shift vector (PSV) which represented the x and y shifts applied to each row in each average image. Due to image stretching (**Figure 6.1C,D: orange box**) and compression (**Figure 6.1C,D: cyan box**), all 10 average images would rarely have pixel shift vectors for the top and bottom rows. Therefore, only PSVs from rows present in all 10 average

images were included in the analysis. This resulted in a smaller analyzable area (~0.5°) across all subjects.

AOSLO Eye Motion Distortion Compared to AO Fundus Images

To further examine the distortion observed in AOSLO images, image sequences were obtained from nine additional subjects at 1°, 2°, and 5° temporal from the center of fixation using both the AOSLO and the AO fundus camera at MCW. We processed the AOSLO image sequences as described above, resulting in 10 average images at each location for each subject. Each AO fundus image sequence was flat-fielded to remove illumination non-uniformities (Bedggood & Metha, 2012; Rha, Schroeder, Godara, & Carroll, 2009). Within each AO fundus image sequence, a reference frame with minimal motion blur was selected, and the remaining frames within the sequence were registered to the reference frame using cross correlation. The 80 frames with the highest correlation were averaged to create a single image for that AO fundus image sequence. The 10 average AOSLO images from each location were first manually aligned to the AO fundus image using Photoshop CS6 (Adobe, San Jose, CA). Each AOSLO image was cropped to 0.55°. To enable fine alignment, the image intensity in both the AOSLO and AO fundus images was normalized using local histogram equalization. The normalized AOSLO images were then registered to the normalized AO fundus image using strip-registration (Dubra & Harvey, 2010). The transformation applied to each AOSLO image was recorded, and the transformations between each AOSLO image to the AO fundus image were converted to PSVs.

The Effect of Image Distortion on Cone Photoreceptor Metrics

To assess the effect of distortion on metrics of mosaic geometry, cone locations were identified within each AOSLO master image or AO fundus image using a previously described semi-automated algorithm (Garrioch et al., 2012). The cone coordinates for

each average image were derived by transforming the master AOSLO image coordinates or AO fundus image coordinates using their corresponding inverse PSVs. For each subject, the cone coordinates from each image were cropped to the smallest common area from all images. The resultant coordinates were then analyzed using four measurements of photoreceptor arrangement: density, inter-cell distance (ICD), Voronoi cell area regularity (VCAR), and percentage of six-sided Voronoi regions. Density was calculated by first determining the Voronoi tessellation of the coordinates. Voronoi regions that extended outside the minimum and maximum and coordinates were considered *unbound* and excluded from the analysis. Voronoi cells contained within the minimum and maximum coordinates were considered *bound*. Density was determined by dividing the total number of bound Voronoi regions by the total bound Voronoi cell area. ICD was calculated by determining the average distance between all cells with bound Voronoi domains. VCAR was calculated by dividing the mean bound Voronoi cell area by the standard deviation of the bound Voronoi cell areas. The number of sides of each Voronoi cell was assessed to determine the percentage of six-sided Voronoi cells, to determine if the number of sides was conserved between each average image (AOSLO-only), and if the number of sides matched the AO fundus image (AOSLO/AO fundus comparison). Additionally, in AOSLO-only image sequences, average PSV and repeatability statistics were calculated for each metric within each subject as previously described (Bland & Altman, 1999). In AOSLO to AO fundus image comparisons, we determined the PSVs applied to each coordinate, and examined the coordinate shift and magnitude within each AOSLO/AO fundus image pair. In addition, we calculated the difference between the metrics derived from the AO fundus image to the metrics from each AOSLO average image. These differences were then converted to relative percentages of the metrics derived from AO fundus image cone coordinates. The

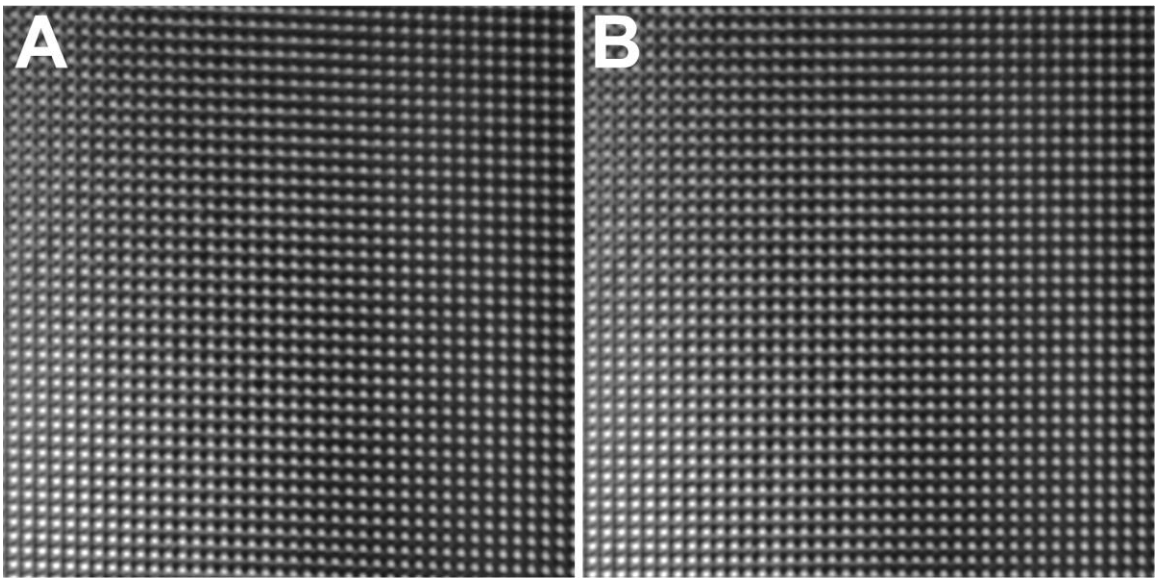

Figure 6.3: A) Rigid (affine) distortion present in AOSLO images B) AOSLO image distortion corrected with an affine transform and coherent point drift.

relative percentages across all subjects were compared to the AO fundus image's metrics using a one-sample Wilcoxon signed rank test.

Results

Static Image Distortion

The images of 2D grid patterns revealed that both the AOSLO and AO-fundus camera have small residual distortions at the edges of their FOVs (**Figure 6.2A,C**).[b] Interestingly, the majority of the distortion detected in the AO fundus image was on the left edge of the FOV (**Figure 6.2B**), with a maximum of 6.1 pixels, or 0.01°, with a root mean square deviation of 1.9 pixels ($3.1°x10^{-3}$). In the AOSLO, distortion was also found

[b]In addition to the static distortions reported here, a rigid, non-sinusoidal distortion (due to a misaligned slow scanner) was present in the grid images from five of the subjects imaged in this study (JC_10549, JC_10567, JC_10418, AD_10302, JC_10620, **Figure 6.3A**). This distortion was due to a small misalignment in our AOSLO's slow scanner. To remove the shear distortion from the affected images, we created an ideal grid as described above and used coherent point drift(Myronenko A., 2010) to register the image grid coordinates to the ideal coordinates. The affine transform used to register to the two point sets was then applied to the affected images to correct the image shear (**Figure 6.3B**).

Table 6.1: AOSLO mean pixel shift vector (PSV) magnitude for each subject at each eccentricity

	Mean (± stdev) PSV Magnitude		
Subject	**1° Temporal**	**2° Temporal**	**5° Temporal**
AD_10252	1.53±0.94	1.55±1.00	1.58±0.91
AD_10253	1.17±0.63	1.14±0.61	1.39±0.98
JC_0677	1.73±0.97	1.08±0.65	1.56±1.08
JC_0878	1.65±0.90	1.62±1.39	2.44±1.33
JC_10121	1.45±0.78	1.56±1.09	2.26±1.51
JC_10122	1.14±0.73	1.17±0.65	1.08±0.64
JC_10145	1.60±0.97	1.72±0.94	1.49±1.01
JC_10304	1.32±1.05	1.66±1.01	1.42±1.06
JC_10316	1.90±1.07	1.75±0.83	1.50±0.84
JC_10318	3.42±3.03	3.05±1.52	1.78±0.89
MM_0103	1.66±1.25	1.16±0.71	1.68±1.00
MM_0136	1.43±0.77	3.27±1.33	3.51±1.92
MM_0173	2.21±1.39	2.28±1.69	2.39±1.31
MM_0182	1.52±0.88	2.13±1.24	2.27±1.32
MM_0207	2.29±1.43	1.95±1.24	1.68±1.03
RR_0025	1.11±0.62	1.24±0.76	0.97±0.55
RR_0114	1.56±0.99	1.57±0.88	1.60±0.93
RR_0358	1.45±0.80	1.53±1.16	1.25±0.69
RR_0384	1.65±0.87	1.55±0.79	1.76±1.05
RR_0424	1.63±0.99	1.45±0.76	1.37±0.88
Average	**1.67±1.16**	**1.72±1.05**	**1.75±1.09**

around the edges of the FOV (**Figure 6.2B,D**), however, it had a smaller maximum magnitude of 4.2 pixels, or 7.0° x10^{-3}, and a root mean square deviation of 1.7 pixels (2.8°x10^{-3}). Despite the relatively high maximum deviations in both AOSLO and AO fundus camera, the vast majority of grid locations were close (<1 pixel, or <1.6°x10^{-3}) to the “ideal” 2D grid; this was reflected in the low RMSD in both the AOSLO and AO fundus camera 2D grids.

Table 6.2: The percent repeatability of each subject at each eccentricity

	1° Temporal				2° Temporal				5° Temporal			
Subject	Density (%)	ICD (%)	% 6 Sided (%)	VCAR (%)	Density (%)	ICD (%)	% 6 Sided (%)	VCAR (%)	Density (%)	ICD (%)	% 6 Sided (%)	VCAR (%)
AD_10252	1.8	0.8	1.7	9.4	2.2	1.1	4.2	3.1	2.4	1.2	2.4	7.6
AD_10253	2.1	1.0	1.1	2.6	1.6	0.7	5.1	4.0	4.3	1.9	5.0	2.8
JC_0677	1.9	0.9	1.8	3.4	2.0	1.0	3.9	2.9	2.5	1.2	9.9	4.1
JC_0878	2.0	1.0	1.3	7.7	3.4	1.6	7.5	5.7	4.0	1.9	5.4	3.5
JC_10121	3.4	1.6	0.8	2.9	3.4	1.7	3.0	3.9	7.0	3.3	6.3	5.4
JC_10122	1.8	0.9	1.5	4.3	1.2	0.6	3.2	4.4	1.6	0.8	4.3	4.4
JC_10145	3.7	1.7	1.5	4.5	2.7	1.3	5.1	4.3	3.8	1.8	6.2	10.0
JC_10304	3.0	1.4	3.5	4.7	4.9	2.3	5.7	3.9	3.2	1.5	6.7	3.2
JC_10316	4.0	1.8	2.3	13.1	3.2	1.5	4.0	8.8	2.6	1.2	5.9	13.2
JC_10318	7.3	3.2	4.6	8.6	6.8	3.1	1.5	12.6	4.2	2.0	3.1	6.6
MM_0103	3.6	1.7	4.0	3.6	2.4	1.2	7.6	4.8	2.2	1.0	3.5	10.8
MM_0136	1.9	0.9	1.1	4.5	5.1	2.5	6.9	3.6	8.7	4.3	10.5	4.1
MM_0173	3.6	1.8	3.1	5.5	3.9	1.9	6.0	3.1	6.1	2.9	7.1	9.9
MM_0182	2.5	1.3	1.5	11.7	4.2	2.1	6.4	6.2	3.8	1.8	3.3	6.0
MM_0207	3.4	1.6	1.9	9.6	2.2	1.1	5.0	6.4	3.3	1.6	6.0	9.8
RR_0025	2.0	0.9	0.9	3.6	2.7	1.3	3.8	1.2	2.0	1.1	10.6	2.3
RR_0114	2.6	1.3	2.0	12.3	3.3	1.5	3.1	6.7	3.1	1.6	7.8	4.0
RR_0358	2.5	1.2	0.9	5.6	4.3	2.1	4.5	4.7	2.2	1.1	6.0	1.5
RR_0384	2.9	1.3	2.0	5.3	2.1	1.0	5.4	5.5	3.2	1.6	4.9	2.6
RR_0424	2.4	1.1	1.0	5.2	2.0	1.0	5.4	2.7	2.8	1.4	9.1	5.0
Average	**2.9**	**1.6**	**2.1**	**7.5**	**3.4**	**1.7**	**5.1**	**5.8**	**3.9**	**2.0**	**6.5**	**7.5**

The Effect of AOSLO Image Distortion on the Repeatability of Measures of Cone Mosaic Geometry

The magnitude of distortion induced by eye motion in AOSLOs was found to vary substantially between images and subjects; average (± standard deviation) PSV magnitudes ranged from as little as 0.97±0.55 to as much as 3.42±3.03 (**Table 6.1**). Upon examination of the effect of these distortions on the repeatability of metrics of photoreceptor structure (**Table 6.2**), we found that the mean (± standard deviation) repeatability of density was 2.9±1.2%, at 1T. Therefore, on average, the difference

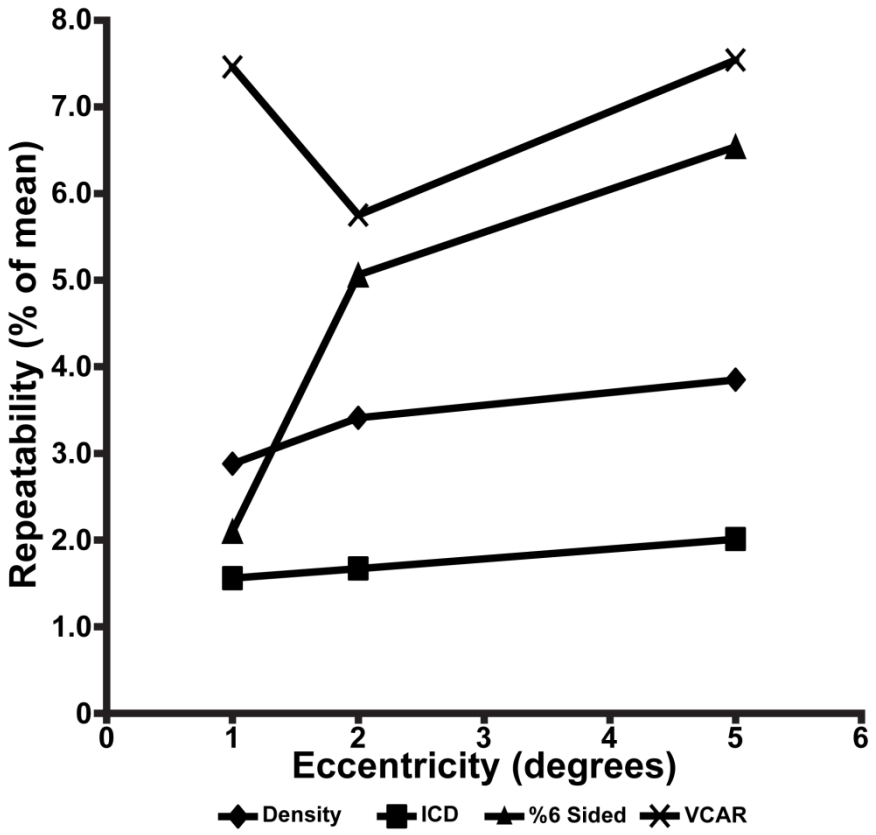

Figure 6.4: Repeatability as a function of eccentricity. Shown is data for density (diamonds), inter-cell distance (ICD, squares), %6-sided Voronoi cells (triangles), and Voronoi cell area regularity (VCAR, crosses). Density and ICD increased similarly as a function of eccentricity. %6-sided Voronoi cells increased dramatically from 1T to 2T, and more modestly from 2T to 5T. VCAR was the only metric that did not monotonically increase, showing better repeatability at 2T than at both 1T and 5T.

between two density measurements for the same subject would be less than 2.9% for 95% of pairs of observations. However, the repeatability varied from 1.1 to 7.3%; while the repeatabilities for most subjects were distributed tightly about the mean, the repeatabilities of some subjects were substantial outliers, contributing to the wider range. This property was mirrored in other metrics: ICD had a mean of 1.6% and a range of 0.8-3.2%, percentage of 6-sided Voronoi cells had a mean of 2.1% but a range of 0.8-4.6%, and VCAR had a mean of 7.5% and a range of 2.6-13.1%. The Voronoi cell morphology was conserved in an average of 84.7% of Voronoi cells at 1T, implying that number of sides for 15.3% of Voronoi domains will change simply by using different reference

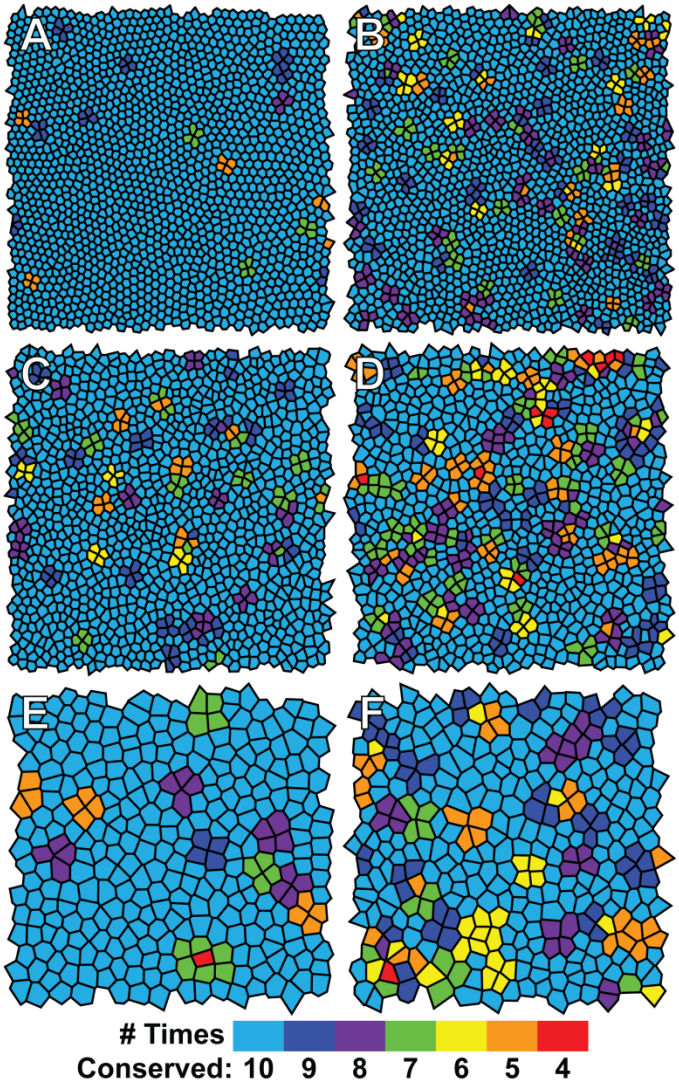

Figure 6.5: Conservation of Voronoi cell domain sides. Shown are Voronoi diagrams from exemplar AOSLO image sequences, illustrating conservation of cell domain sides across all 10 AOSLO frames. Each Voronoi cell is color-coded to indicate the maximum number of times that cell had the same number of sides across all average images. The left column shows ROIs that had a highly conserved number of Voronoi cell sides, and the right column shows ROIs with lower conservation. Each row corresponds to images obtained at 1° (A-B), 2° (C-D) or 5° (E-F) temporal to fixation. The images from 1T generally had a higher percentage of %6 sided cells than both 2T and 5T, potentially affecting the stability of the Voronoi map.

frames. Interestingly, we determined that PSV magnitude was significantly correlated ($p<0.01$) with the repeatability of density, ICD, and the percentage of 6-sided Voronoi cells, but not VCAR.

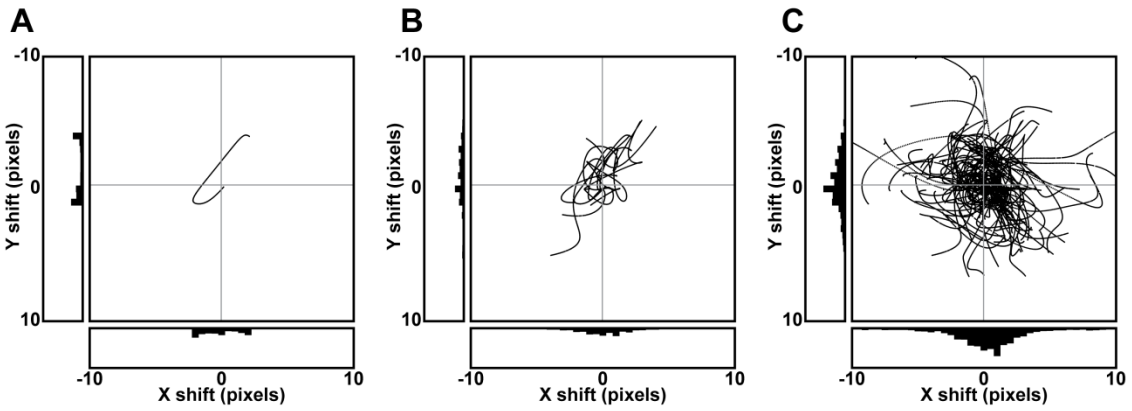

Figure 6.6: AOSLO image distortion relative to an AO fundus camera image. A) All pixel shift vectors (PSVs) between a single AOSLO/AO fundus camera image pair plotted with respect to their X and Y components. Histograms of the X and Y components of each PSV are shown at the bottom and to the left of each PSV shift plot. Single image pairs do not appear to adhere to a particular distribution. When combining all PSVs between a single subject's 10 AOSLO/AO fundus image pairs (B), the Gaussian distribution is substantially more visible. Displaying the PSVs from all subjects and image pairs (C) more accurately depicts the distribution of PSVs.

Interestingly, we found that the repeatability of each metric varied as a function of eccentricity (**Figure 6.4**). On average, the repeatability of the cone density degrades with eccentricity, increasing from 2.9±1.2% at 1T to 3.4±1.4% and 3.9±1.8% at 2T and 5T, respectively. Similarly, ICD's repeatability increased linearly, from 1.6±0.54%, 1.7±0.64%, and 2.0±0.85% at 1T, 2T, and 5T, respectively. The repeatability of percent 6-sided Voronoi cells was much lower at 1T (2.1±1.1%) than at 2T and 5T (5.1±1.6%, 6.5±2.4%). VCAR's repeatability dropped from 7.5±3.3% at 1T to 5.8±2.5% at 2T, and rose again to 7.5±3.3% at 5T. The conservation of Voronoi cell morphology also changed as a function of eccentricity; conservation decreased from the average of 84.7% at 1T to 71.6% and 73.2% at 2T and 5T (**Figure 6.5**). PSV magnitude remained significantly correlated with density and ICD at 2T and 5T; however, the percentage of 6 sided Voronoi cells was no longer correlated, and VCAR remained uncorrelated.

Table 6.3: Mean (± stdev) x and y pixel shifts of AOSLO image sequences relative to their corresponding AO fundus images

	1° Temporal		2° Temporal		5° Temporal	
Subject	**X Shift (pixels)**	**Y Shift (pixels)**	**X Shift (pixels)**	**Y Shift (pixels)**	**X Shift (pixels)**	**Y Shift (pixels)**
AD_10055	0.52±1.81	0.16±2.90	1.28±1.36	-0.55±1.70	-0.54±1.31	-0.28±2.35
AD_10302	0.06±1.42	0.93±1.83	-1.97±2.1	1.60±1.35	-0.98±1.23	0.06±1.43
JC_0002	1.09±0.91	-0.81±1.37	-0.57±1.26	0.89±1.26	0.38±1.47	-0.67±1.36
JC_0616	2.02±1.35	0.53±1.21	-0.64±1.53	-0.73±1.79	2.34±1.5	-1.08±1.47
JC_0905	-1.10±3.76	2.11±1.87	2.51±3.55	-0.91±1.60	-2.51±6.71	-2.45±3.84
JC_10418	1.11±1.70	-0.59±3.16	1.02±1.09	-0.35±2.88	-1.19±0.97	0.29±1.94
JC_10549	0.15±1.39	0.32±0.95	0.20±0.99	2.28±1.23	0.89±1.38	0.55±1.49
JC_10567	-0.32±3.00	-1.09±1.96	1.87±1.34	0.89±2.31	0.80±1.05	0.45±1.83
JC_10620	0.87±3.42	1.65±2.56	1.37±1.43	-2.25±4.44	-2.40±3.64	0.60±2.09
Average	**0.5±2.30**	**0.36±2.11**	**0.58±1.79**	**0.07±2.28**	**-0.43±2.79**	**-0.26±2.11**

The Effect of AOSLO Image Distortion on the Accuracy of Measures of Cone Mosaic Geometry

When examining the distortion in AOSLO images aligned to AO fundus images at 1T, we found that, on average, PSVs were Gaussian distributed with a mean (± standard deviation) of 0.27±2.5 pixels along the x-axis, and 0.36±2.4 pixels along the y-axis (**Figure 6.6C**), with corresponding magnitudes of 1.84±1.8 pixels along the x-axis and 1.79±1.6 pixels along the y-axis. The PSVs were Gaussian distributed within a single subject (**Figure 6.6B**), but not within a single AOSLO/AO fundus image pair (**Figure 6.6A**). Other eccentricities followed similar patterns (**Table 6.3**).

We determined that on average both the density and ICD metrics from AOSLO images were not significantly different than AO fundus images (**Figure 6.7A,B**) across all eccentricities ($p>0.05$, Wilcoxon signed rank test). The percentage of six-sided cells calculated from AOSLO images was significantly different from AO fundus images only at 1T ($p<0.001$, Wilcoxon signed rank test, **Figure 6.7C**). VCAR assessed in AOSLO images was significantly different than in AO fundus images for all examined

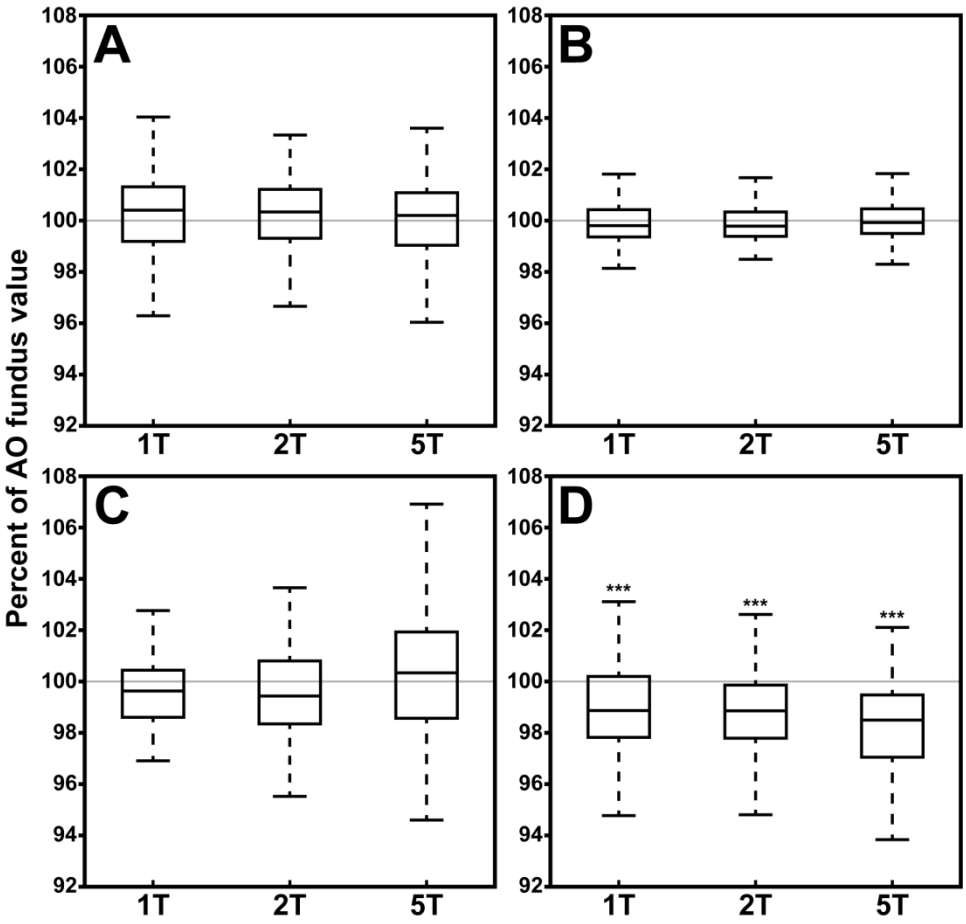

Figure 6.7: Relative differences between AOSLO and AO fundus camera measurements. Density (A), ICD (B), and % 6 Sided (C) were not significantly different at $p<0.05$, across all eccentricities. However, AOSLO measurements of VCAR were significantly different than those measured from the AO fundus camera (D). These differences were maintained across all eccentricities, suggesting that VCAR does not provide an accurate, but may provide a precise, estimate of the true Voronoi cell area regularity.

eccentricities ($p<0.001$, Wilcoxon signed rank test, **Figure 6.7D**). On average, AOSLO number of Voronoi cell sides matched the flood frames in 77.7%, 74.9% and 73.4% at 1T, 2T, and 5T, respectively (**Figure 6.8**).

Discussion

Image distortions within optical systems are typically only assessed using ray-tracing software. However, empirically measured residual distortions are rarely reported

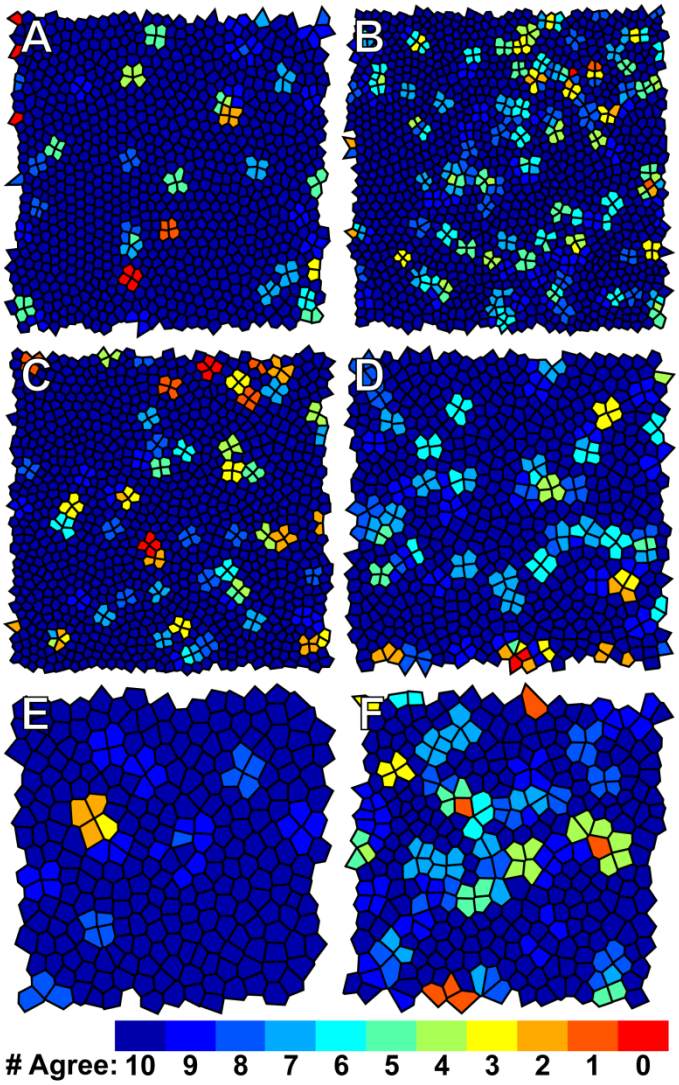

Figure 6.8: Agreement between AOSLO-derived Voronoi domains and AO fundus-derived Voronoi domains. Voronoi diagrams from exemplar AO fundus images showing the Voronoi cell domain agreement with respect to the corresponding aligned AOSLO average images. Each Voronoi cell is color-coded to indicate how many times the number of sides of the AO fundus derived Voronoi cell matched the number of sides of the Voronoi cell derived from the aligned AOSLO average images. The left column shows ROIs with a high amount of agreement to the AOSLO image sequences, and the right column shows ROIs with lower agreement. Each row corresponds to images acquired at 1° (A-B), 2° (C-D) or 5° (E-F) temporal to fixation.

(Garrioch et al., 2012; Ramaswamy & Devaney, 2013). After accounting for the static image distortion in both our AO ophthalmoscopes, we examined intra-frame distortion due to involuntary eye motion and its contribution to the repeatability of measures of the cone mosaic in AOSLO images. Then, we assessed the accuracy of these AOSLO-

derived measures by comparing them to those from AO fundus camera images, which are relatively free of intra-frame distortion. These data illustrate an important characteristic of images obtained from scanning ophthalmoscopes that must be taken into consideration when interpreting metrics describing the geometry of the cone mosaic or other cell mosaics such as RPE cells, or when characterizing the shape/dimension of structures like blood vessels or nerve fiber layer bundles. The approach outlined here could be used to evaluate any scanning ophthalmoscope.

One limitation of our method is due to the image registration used in these analyses. The registration employs a strip-based rigid transform and assumes that image distortion is caused only by intra-frame eye motion. This does not account for torsional eye motion (Putnam, 2003; Ramaswamy & Devaney, 2013), nor the static image distortion mentioned above, and as a result, registration is often imperfect. If one examines a video from a distorted edge within a registered set of images, the cone photoreceptors can be seen “wobbling”. In this work, the impact of this wobble was mitigated by averaging multiple frames and by using ROIs within areas of minimal static distortion. However, if unmitigated, it could significantly affect the accuracy of measurements that require the precise tracking of cells within single frames, such in temporal analyses (Cooper, Dubis, et al., 2011; Grieve & Roorda, 2008; Pallikaris, Williams, & Hofer, 2003; Pircher et al., 2010), or when assessing images from multiple time points (Wang et al., 2015).

It is important to emphasize that these findings apply only to the AOSLO systems used here (which had equivalent designs). It cannot be assumed that these results will be conserved between system designs, as the magnitude and variability of these distortions will vary between hardware (Cooper, Harvey, et al., 2013). Moreover, even slightly misaligned scanners can induce rigid deformations of images produced from scanning ophthalmoscopes; until measuring it directly using the 2D grid, (see **Figure**

6.3) we were completely unaware of such a misalignment in our system. Thus, not only must these distortions be measured experimentally across different systems, but they should be reassessed following any system alignment so they can be compensated for by digitally resampling each image. Our data highlight the need to conduct such an analysis prior to relying on measurements of the cone mosaic from a given device. Additional factors could limit the generalizability of these findings. For example, we examined repeatability at a fixed ROI size; however, it has been previously noted that the size of the ROI directly influences both the metrics that are derived from a mosaic (Lombardo et al., 2014), and their repeatability (Garrioch et al., 2012). Moreover, these results are limited to only three eccentricities. While we observe a monotonic increase (worsening) in the repeatability all metrics except for VCAR, these trends may not continue with increased retinal eccentricity. In addition, we observed that the repeatability of density, ICD, and percent six-sided cells was significantly linked to PSV magnitude (**Tables 6.1 and 6.2**). Therefore, in subjects where increased image distortion is unavoidable (such as in subjects with nystagmus or poor fixation) one would expect the repeatability of the measurements to be worse. In particular, this suggests that measurement repeatability should also be separately characterized in subject populations that have a predisposition for image distortion magnitudes greater than that of the normal population.

When we compared AOSLO images to AO fundus images, we determined that on average, AOSLO images align almost perfectly to AO fundus images (**Figure 6.5C**), resulting in metrics that were not significantly different than those derived from AO fundus images, except for VCAR (**Figure 6.7**). This suggests that the repeatability reported for all metrics except VCAR are repeatable about the actual value of the metric, not just the mean of the sample population. Moreover, these data imply that the AOSLO distortion can approximate a "distortionless" AO fundus image, suggesting that multiple

AOSLO images could be aligned in order to achieve an accurate estimate of cone mosaic geometry without requiring an AO fundus camera. However, it is unlikely that 10 images (used here) would provide enough sampling of the PSV distribution to enable a consistently unbiased estimation of the AO fundus image, and more images would be required to provide an accurate estimate of the true average distortion. Moreover, the manual selection of 10 co-localized frames from each AOSLO image sequence is impractical when datasets can consist of more than 100 image sequences. Thus, more efficient reference frame selection methods are needed to enable the creation of an average AOSLO image that accurately approximates an AO fundus image (*i.e.* the anatomical “truth”).

In conclusion, we defined the effect of intra-frame distortions due to involuntary intra-frame eye movements on measurements of repeatability in healthy subjects. Moreover, we determined that a large, minimally distorted set of images acquired from our AOSLO could be used to approximate “distortionless” AO fundus images. However, these data likely represent a “best case” scenario, and characterizing both the static distortions and image distortions due to intra-frame eye motion within each system and within multiple subject populations remains essential to the development of this modality as a clinical tool.

Chapter Seven: Spatial and temporal variation of rod photoreceptor reflectance in the human retina

Chapter seven was published during my graduate studies in collaboration with Alfredo Dubra, who, at the time, was at the University of Rochester, in Rochester New York.

Citation:

Cooper, R. F., Dubis, A. M., Pavaskar, A., Rha, J., Dubra, A., & Carroll, J. (2011). Spatial and temporal variation of rod photoreceptor reflectance in the human retina. Biomedical Optics Express, 2(9), 2577-2589.

Contributions:

These experiments were designed by Dr. Carroll and me, with input from Dr. Austin Roorda, Ben Masella (bleaching calculations) and Dr. Jungtae Rha (photoreceptor reflectivity origins). All authors and Brett Schroeder provided imaging support. Zach Harvey provided AOSLO control software support. I imaged all subjects within this paper and implemented and performed the spatial and temporal analyses. In addition, I completed the writing and figure making for the publication in collaboration with Dr. Carroll.

Introduction

In examining the first direct in vivo images of the human cone mosaic, one of the more salient features of the appearance of individual cone photoreceptors is that they vary considerably in their reflectance (Miller et al., 1996; Wade & Fitzke, 1998). With the advent of ophthalmic adaptive optics (AO) (Hofer, Artal, Singer, Aragon, & Williams, 2001; Liang et al., 1997), it has become almost routine to non-invasively obtain images of the cone mosaic. Regardless of the AO imaging modality used (scanning laser ophthalmoscope, fundus camera, or optical coherence tomography), similar regional variation in the appearance of cones has been seen in the corresponding in vivo images of the cone mosaic (Chui et al., 2008a; Duncan et al., 2007; Fernández et al., 2008; Kocaoglu, Lee, et al., 2011; Pallikaris et al., 2003; Roorda et al., 2002; Roorda & Williams, 2002; Zawadzki et al., 2009; Zhang et al., 2006). By measuring the Stiles-Crawford effect of individual cones using an AO fundus camera, it was shown that this spatial variability is not caused by cone-to-cone differences in directional tuning (Pallikaris et al., 2003; Roorda & Williams, 2002). Despite being a universal feature of images of the cone mosaic, the origin of the cell to cell variability in cone reflectance remains unclear.

Besides exhibiting variability in reflectivity between different cones, individual cones also vary in their reflectivity over time, on scales ranging from seconds to hours (Pallikaris et al., 2003; Pircher et al., 2010; Rha, Jonnal, Thorn, et al., 2006). These changes occur both in the presence and absence of a stimulus and it has been suggested that these changes reflect physiological activity within the photoreceptor. For example, using a flood-illuminated AO fundus camera, Pallikaris et al. suggested that long-term variation in cone reflectivity could be due to the process of disc shedding (Pallikaris et al., 2003). Recently, Pircher et al. (2010) and Jonnal et al. (2010) provided

data suggesting that the longer term temporal changes in cone reflectivity are due to the outer segment renewal process. In contrast, rapid changes in reflectivity can be seen in response to stimulation with light (Grieve & Roorda, 2008; Jonnal et al., 2007; Rha et al., 2009), and it has been suggested that these rapid changes in cone reflectivity measured in vivo are related to the phototransduction process (Jonnal et al., 2007). The clinical applications of such measurements could be substantial; with the ability to monitor cone structure and function, researchers would be positioned to elucidate more clearly the disease sequence of retinal degenerations, and also provide additional tools for assessing therapeutic efficacy in individuals receiving intervention.

The human retina has two classes of photoreceptor, cones and rods. While rods outnumber cones by nearly 20:1, cones have received considerably more attention in cellular retinal imaging, primarily due to their easy visualization, even without AO-equipped devices (Liang et al., 1997; Pircher et al., 2010; Wade & Fitzke, 1998; Wolsley et al., 2010). This is unfortunate, given the prominent role that rods play in aging (Curcio, 2001; Curcio, Millican, Allen, & Kalina, 1993; Curcio, Owsley, & Jackson, 2000; Gao & Hollyfield, 1992) and devastating retinal degenerations (Berson, 1993; Newsome, 1988). In cases where rod dysfunction precedes that of the cones, the inability to image rod structure and function represents a significant barrier in bringing high-resolution imaging tools to bear on their management. Part of the difficulty in translating previous studies on the spatial and temporal properties of cones to the rod mosaic has simply been an inability to readily resolve rods in vivo. Besides a couple reports of rod visualization in the diseased retina (Carroll, et al., 2012; Carroll, Choi, & Williams, 2008), there had only been a single report of rod visualization in the normal retina. However, it was the result of significant image processing and enhancement, and provided only intermittent rod visualization (Doble et al., 2011). Recently, we developed an AOSLO capable of imaging the contiguous rod photoreceptor mosaic (Dubra & Sulai, 2011; Dubra et al., 2011). Here

we sought to investigate the spatial and temporal variation in reflectivity of the rod mosaic and compare its behavior to that previously observed for the cone photoreceptor mosaic.

Methods

Human subjects

One male (JC_0002, age 28 years, emmetrope) and one female (JC_0138, age 27 years, −1D myope) were recruited for the study. Neither of the subjects had any retinal pathology, though the male subject does have an inherited color vision defect (deuteranopia). All research followed the tenets of the Declaration of Helsinki, and study protocols were approved by the institutional research boards at the Medical College of Wisconsin and Marquette University. Subjects provided informed consent after the nature and possible consequences of the study were explained. Axial length measurements were obtained on both subjects using an IOL Master (Carl Zeiss Meditec, Dublin, CA) for scaling of the retinal images.

Imaging the photoreceptor mosaic

An AOSLO was used to image each subject's photoreceptor mosaic. The AOSLO is housed at the Medical College of Wisconsin, and system design details can be found elsewhere (Dubra & Sulai, 2011). A 680nm superluminescent diode with a full-width at half-maximum (FWHM) bandwidth of 8.5nm from Superlum Ireland (Carrigtwohill, County Cork, Ireland), was used for reflectance retinal imaging. Assuming a refractive index of 1.43 for the cone outer segment, we estimate the coherence length of this source as 17 μm. The power incident on the cornea was 111.11 μW.

The subjects were each imaged at one-hour intervals beginning at 10am and ending at 10pm. Their right eye was dilated and accommodation suspended using one

drop each of Phenylephrine Hydrochloride (2.5%) and Tropicamide (1%), and the drops were re-administered between each imaging session. A foveal and peripheral retinal location was selected for imaging and analysis: 0.5° temporal-superior from fixation, and 10° temporal from fixation, respectively. The field of view of the raw images was 0.96° x 0.96°. At each time point, a single image sequence was acquired at the foveal location, and six image sequences were taken at the 10° temporal location. The additional image sequences in the peripheral location were acquired to minimize the effects of any hourly fixation drift and ensure maximum overlap of the common image area. Individual image sequences contained 150 frames. Each image sequence was acquired within about 10 minutes from the start of each hour. Owing to the fact that the targeted image location was exposed to the imaging light (680 nm) even when we were not saving an image sequence, we estimate that at each time point the cones and rods were 100% and 70% bleached, respectively. For the remainder of each hour, the subject's visual activity was not limited and consisted mainly of reading and computer work. As such, other than the time spent acquiring images, each subject was exposed to normal indoor lighting conditions for the entire experiment duration of 12 hours.

Processing of AOSLO image sequences

In order to correct for distortions in the retinal images due to the sinusoidal motion of the resonant optical scanner, we first estimated the distortion from images of a Ronchi ruling, and then re-sampled the images over a grid of equally spaced pixels. After this "desinusoiding", the movies were manually inspected to identify reference frame(s) with minimal distortion and maximal sharpness for subsequent registration using custom software (Dubra & Harvey, 2010). Registration of frames within a given image

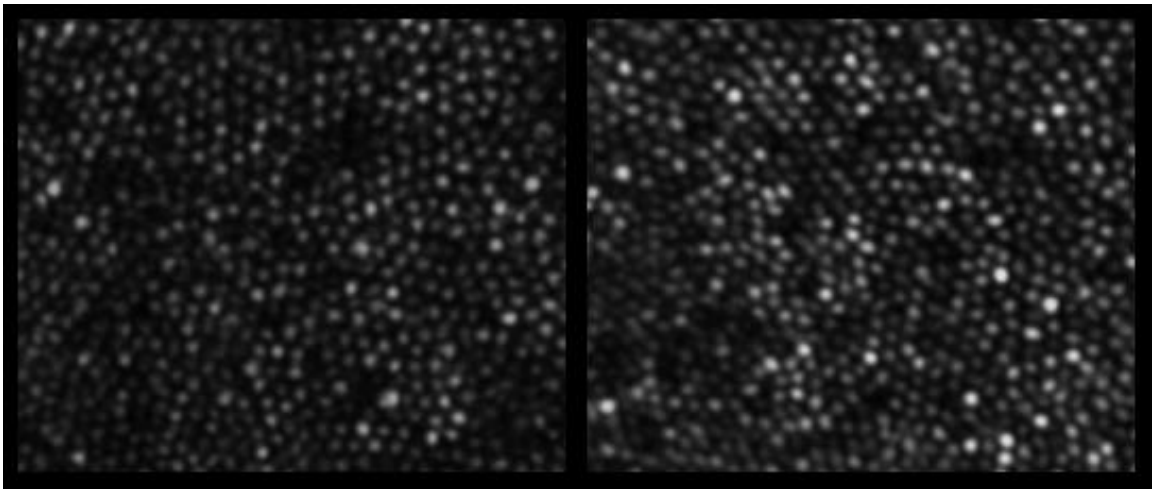

Figure 7.1: Time-lapse video showing changes in cone reflectance at 0.5° temporal-superior over 12 hours for JC_0138 (left) and JC_0002 (right). Each image is 112 x 92 μm. (Media 1)

sequence was performed using a “strip” registration method, in which the images were registered by dividing the image of interest into strips, aligning each strip to the location in the reference frame that maximizes the normalized cross correlation between them. Once all the frames were registered, the 50 frames with the highest normalized cross correlation to the reference frame were averaged, in order to generate a final image with an increased signal to noise ratio (SNR) for subsequent analysis. For the peripheral imaging location, the multiple registered average images from each time point were manually inspected, and the image with maximum apparent overlap to the images from the other time points was selected for further processing and analysis.

For a given imaging location, the average images from each time point were registered to each other using an affine transformation (i2kRetina, Dual Align, LLC, Clifton Park, NY). This aligned image stack was then cropped to a common area, a reference frame was selected, and the image stack then went through strip registration as described above. Finally, the image series were normalized to the temporal mean of

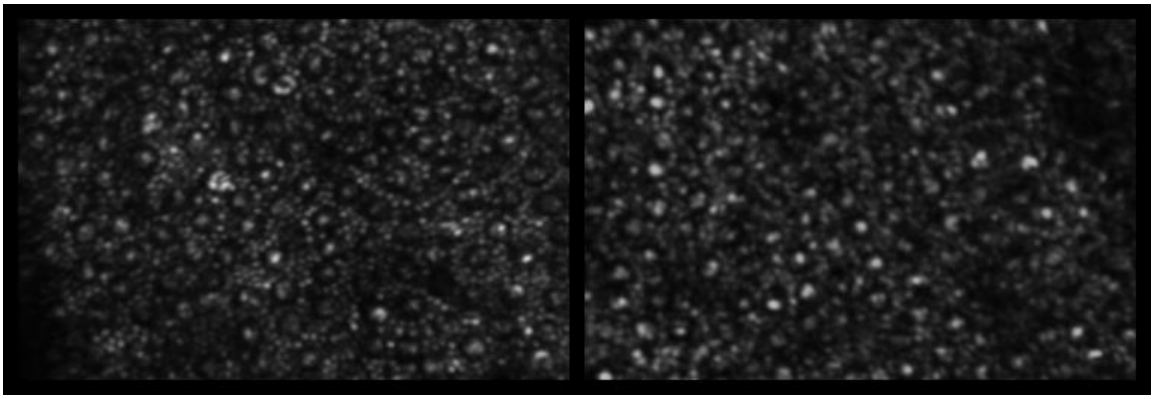

Figure 7.2: Time-lapse video showing changes in rod reflectance at ~10° temporal over 12 hours for JC_0138 (left) and JC_0002 (right). Each image is 168 x 122 μm. (Media 2)

the nonzero portions of the stack. The movies, **Figure 7.1** and **Figure 7.2**, display the result of these registrations for the foveal and peripheral imaging locations, respectively.

Generating reflectance profiles

To ensure we were selecting the center of a given cell, we first averaged the images from all 13 time points at each imaging location for both subjects, resulting in four composite images (**Figure 7.3** and **Figure 7.4**). These images were then used to determine preliminary cone and rod coordinate locations. The position of foveal cones was identified using a modified version of previously described semi-automated algorithm, which also allowed manual addition/subtraction of cones missed or selected in error (Li & Roorda, 2007). A total of 1,980 cones were selected for analysis using this method. The position of peripheral rods was determined by manual selection, and a total of 1,690 rods were selected for analysis. From these preliminary coordinates, the final coordinates were determined using custom MATLAB (Mathworks, Natick, Massachusetts, USA) software that identified the local maximum within a 3x3 pixel (1.25x1.25 μm) region around the initial cone (or rod) coordinate. Owing to the increase in cell diameter, multiple waveguide modes were present in the peripheral cone

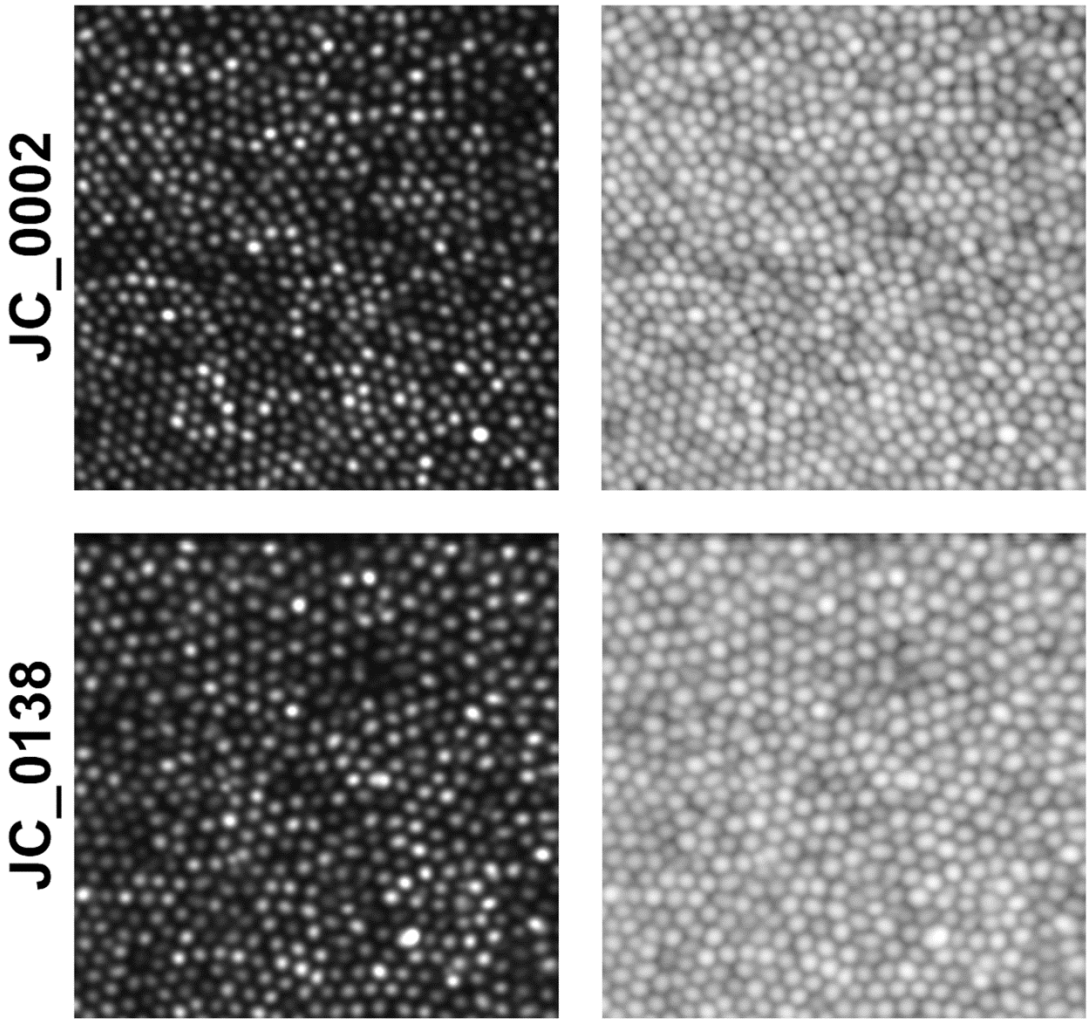

Figure 7.3: Photoreceptor composite images for the foveal (0.5° temporal-superior) imaging locations. These images were created by aligning and averaging all 13 time points, and are shown using both a linear (left) and logarithmic (right) display. Scale bar is 25 µm.

photoreceptors. This resulted in variability in the reflectance of individual peripheral cones within their cell boundary. In addition, the small number of cones (<50) present in the peripheral images would make any global conclusion about their reflectance behavior over time difficult. As such, we decided not to analyze the reflectivity of these peripheral cones.

The final coordinates were adjusted for each frame within the aligned image stack, in order to compensate for small errors in image registration. This was done by

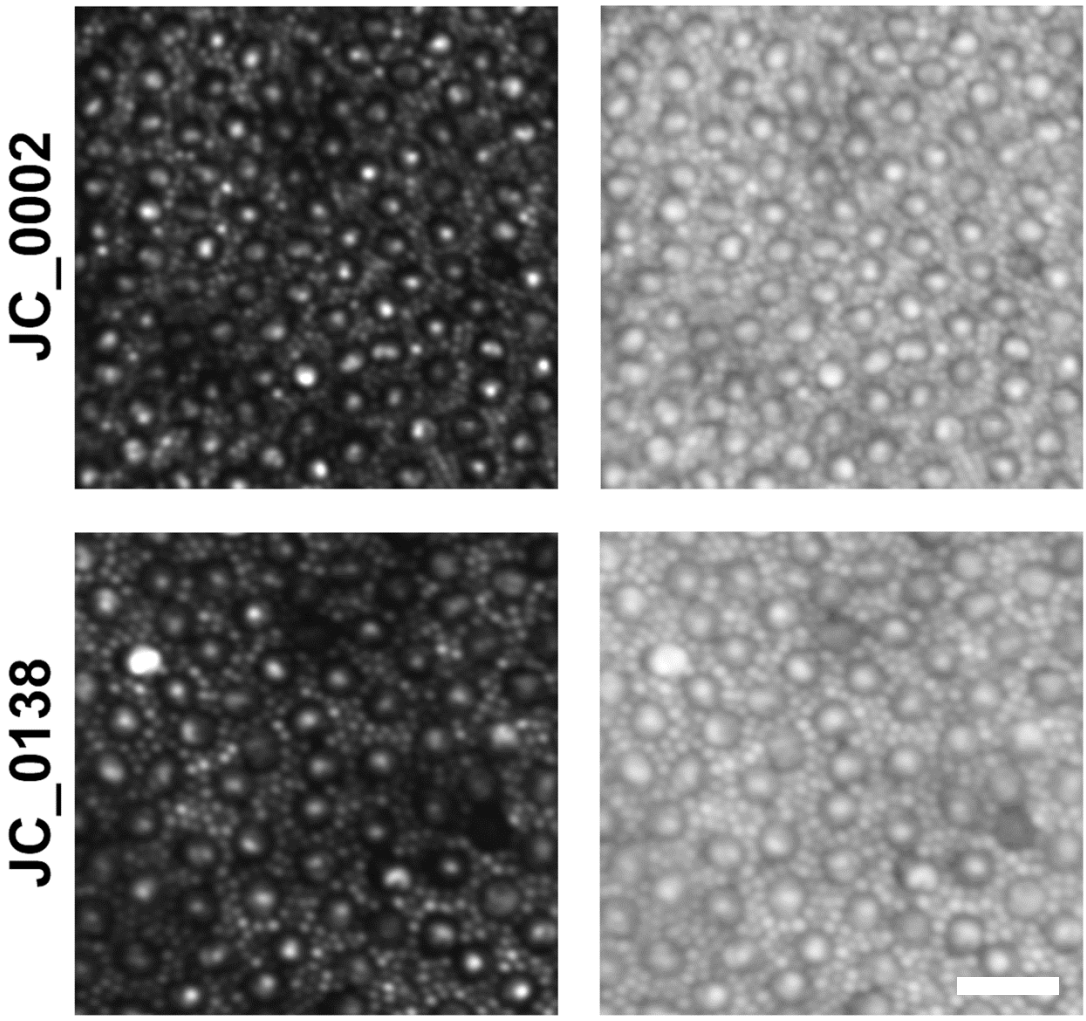

Figure 7.4: Photoreceptor composite images for the peripheral (~10° temporal) imaging locations. These images were created by aligning and averaging all 13 time points, and are shown using both a linear (left) and logarithmic (right) display. Scale bar is 25 µm.

first projecting a mask for each cell through the aligned image stack. A square 3x3 pixel and circular 5 pixel diameter mask was used for rods and cones, respectively. For each frame, each cells' mask was repositioned to a local maximum, which never occurred greater than 1 pixel away from the original final coordinate. Reflectance profiles for every isolated cone and rod were generated by plotting reflectance as a function of time, where reflectance at a given time point is defined as the average intensity of all the pixels within the photoreceptor mask. For easier visualization of the behavior of

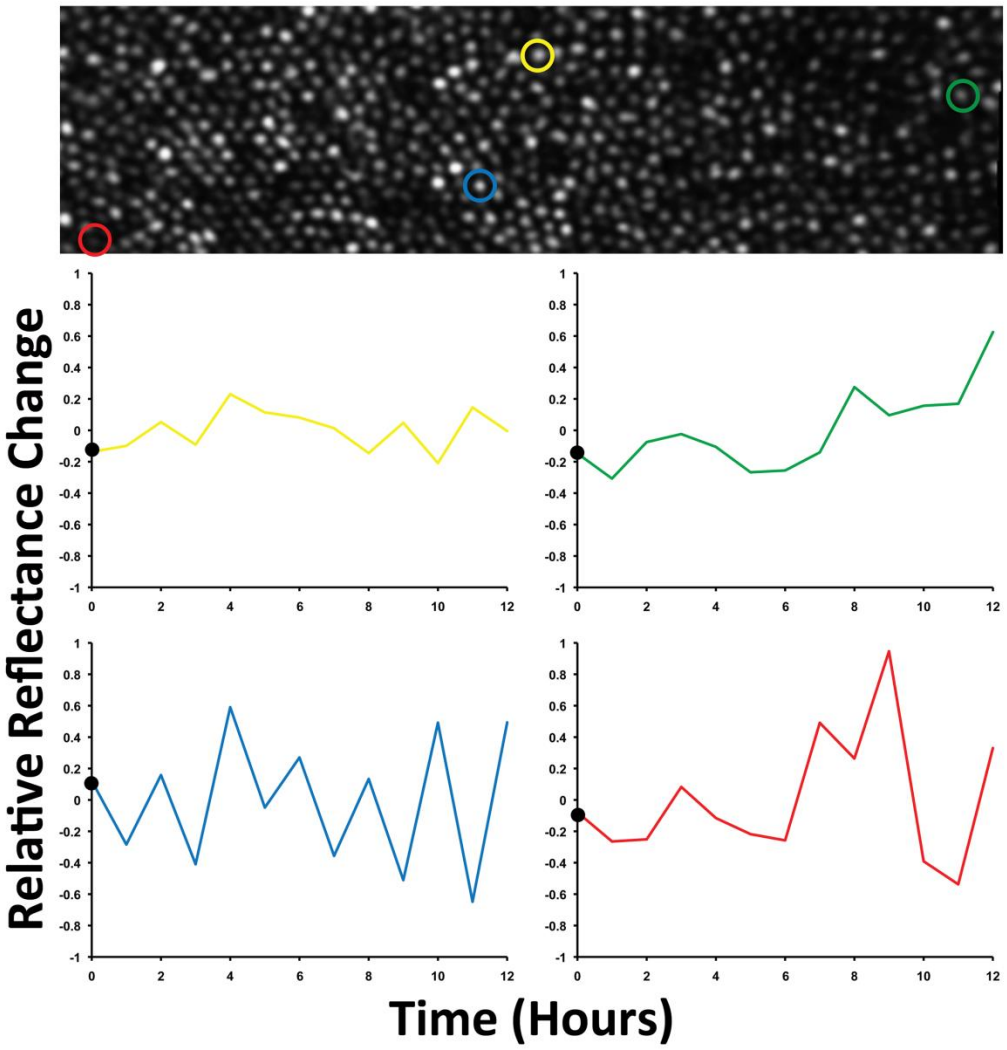

Figure 7.5: Movie sequence of hourly AOSO images of the cone mosaic in JC_0002, showing representative normalized cone reflectance profiles. The archetypes shown are flat (top left), gradual (top right), oscillatory (bottom left), or abrupt (bottom right). The circles in the retinal image are color coded to their respective profile plot, and their size was chosen for improved visualization and does not represent the area over which reflectance was analyzed. (Media 3)

individual cells, we normalized the reflectance values of each profile to the mean reflectance of that particular cell and then subtracted 1. This results in plots that effectively show the relative reflectance changes.

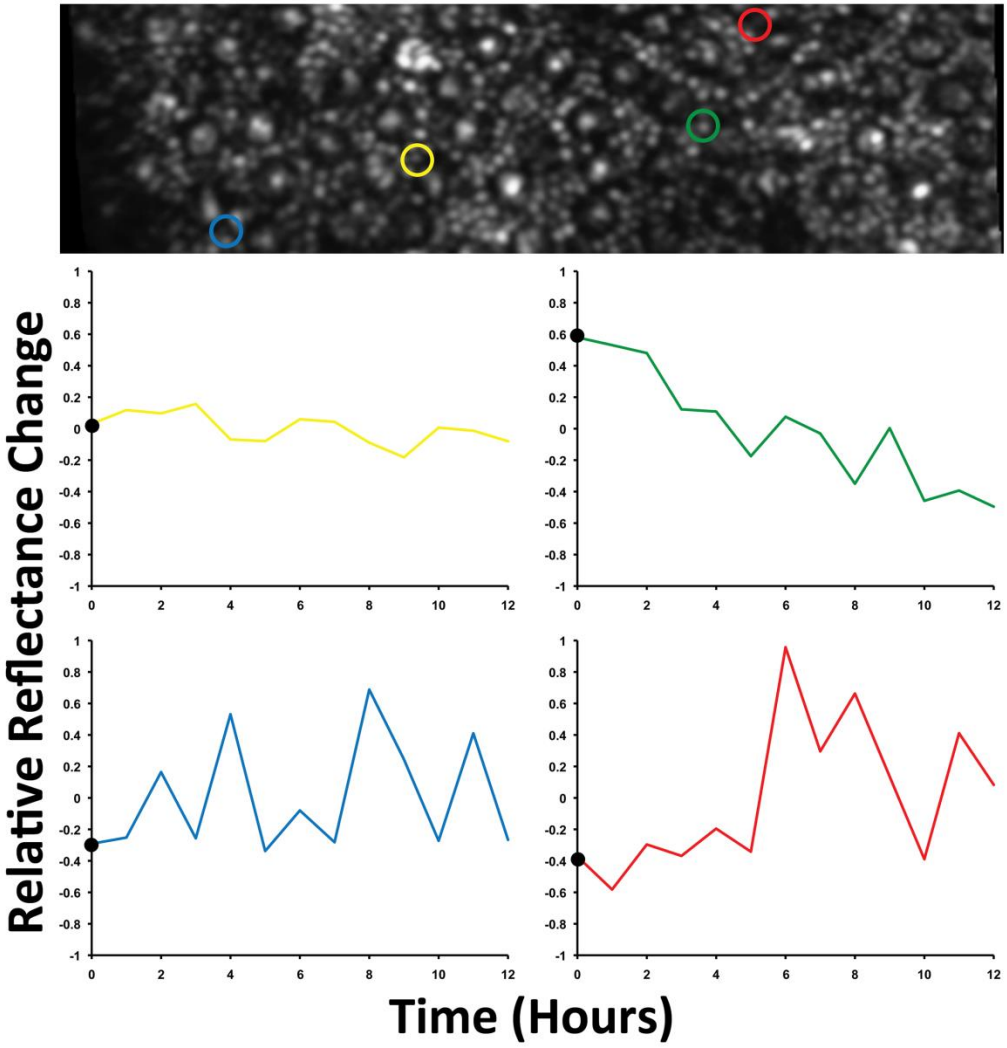

Figure 7.6: Movie sequence of hourly AOSO images of the rod mosaic in JC_0138 showing representative normalized rod reflectance profiles. The primary archetypes were flat (top left), gradual (top right), oscillatory (bottom left), or abrupt (bottom right). The circles in the retinal image are color coded to their respective profile plot, and their size was chosen for improved visualization and does not represent the area over which reflectance was analyzed. (Media 4)

Analyzing reflectance profiles

Each cell type (rod/cone) was analyzed separately for each subject. To analyze the reflectance profiles for a given cell type, we determined the linear component (slope) of each profile by calculating the least squares linear fit of the profile. The mean and standard deviation of the slopes was calculated, and each cell was placed in one of two

groups. Those with linear components that fell below 1 standard deviation from the mean were placed in the low slope group, and the remaining cells placed in the high slope group. Next, the linear component was removed from each profile and the standard deviation of the resultant signal was computed. The mean and standard deviation of the signal standard deviations for cells within each group was calculated. Cells having a signal standard deviation below 1 standard deviation from the mean for that group of cells were considered to have a linear reflectance profile, with the remaining cells regarded as having a fluctuating reflectance profile.

Further classification is possible, but is used for illustrative purposes only. For cells having a linear reflectance profile (top panels in **Figure 7.5** and **Figure 7.6**), the cells with low slope were considered flat while those with high slope were considered gradual. For cells having a fluctuating reflectance profile (bottom panels in **Figure 7.5** and **Figure 7.5**), the cells with low slope were considered to have oscillatory profiles while those with high slope could be either oscillatory or abrupt. Among the high slope cells, those with the highest signal standard deviation (greater than 1 standard deviation from the mean) were classified as abrupt and the remainder was classified as oscillatory, having signal standard deviations within 1 standard deviation of the mean. All statistical analysis was done using Instat (GraphPad Software, Inc., La Jolla, CA).

Results

Temporal variability of rod and cone photoreceptor reflectance

Inspection of the movies in **Figure 7.1** and **Figure 7.2** reveals remarkable temporal variability of the reflectance of individual cone and rod photoreceptors, respectively. Moreover, it is clear that not all cells are behaving the same way – some cells have multiple oscillations in their reflectance, while others showed no change in reflectance

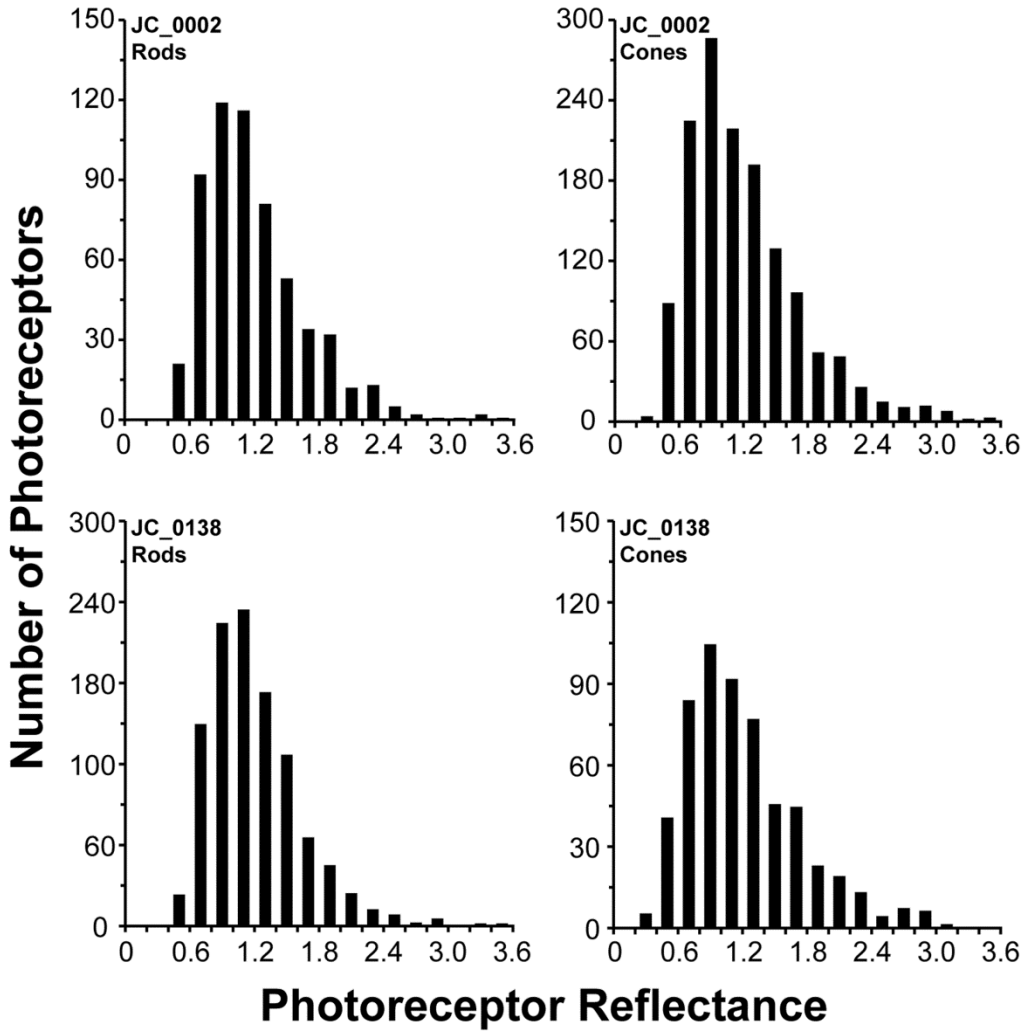

Figure 7.7: Histogram of normalized reflectance of the cone and rod photoreceptor mosaics, for the 11am time point. Both the rods and cones each show significant variation in reflectivity, and similar results were observed at the other time points.

over the 12-hour experiment. This variation can be further appreciated in **Figure 7.5** and **Figure 7.6**, which show normalized reflectance profiles for cones (JC_0002) and rods (JC_0138). The cells displayed were chosen so as to capture the range in archetypes observed. Using the classification scheme defined above, we found that for JC_0002, 15.6% of the cones and 13.5% of the rods had flat or gradual profiles, while for JC_0138, 16.1% of the cones and 13.7% of the rods had flat or gradual profiles. One could likely further refine the classification of these profiles by assessing the magnitude

of the linear component; however subsequent thresholds on metrics like these would be subjective and not contribute further to the understanding of the biological basis of these reflectance changes. The conclusion from these data is that there is enormous variation in both cone and rod reflectivity over time.

Cell-to-cell variation of cone and rod reflectance

As mentioned earlier, one of the more prominent features in images of the cone mosaic is variation in the reflectivity of individual cones. While the origin of this variation is not fully understood, we examined whether the rod mosaic showed similar variation. At the 11am time point, we analyzed the distribution of the normalized reflectance values for the cones and rods for both subjects. **Figure 7.7** shows the corresponding normalized histograms, and there was substantial variation in both cell types. For the cones, the standard deviation was 52% of the mean for both JC_0138 and JC_0002. For the rods, the standard deviation was 42% of the mean for JC_0138 and 48% of the mean for JC_0002. For each subject, the rods were found to have a significantly lower standard deviation that the cones (JC_0002, $p = 0.0246$; JC_0138, $p<0.0001$). One explanation for the rods being apparently less variable is that the rods had an overall lower reflectivity than the cones (JC_0002; cones = 61.74 a.u., rods = 38.16 a.u., $p<0.0001$, Mann-Whitney test; JC_0138; cones = 61.91 a.u., rods = 50.47 a.u., $p<0.0001$, Mann-Whitney test). Despite initially setting the gain of the PMT's to provide roughly equal mean pixel intensity for the foveal and peripheral imaging locations, the peripheral cones appear to have driven the behavior of the overall image intensity. This leaves the rods as being dimmer on average and may account for their apparently lower standard deviation. A second factor to consider is that rods and cones have different morphology (Hoang et al., 2002), which of course would be expected to contribute to their waveguide behavior.

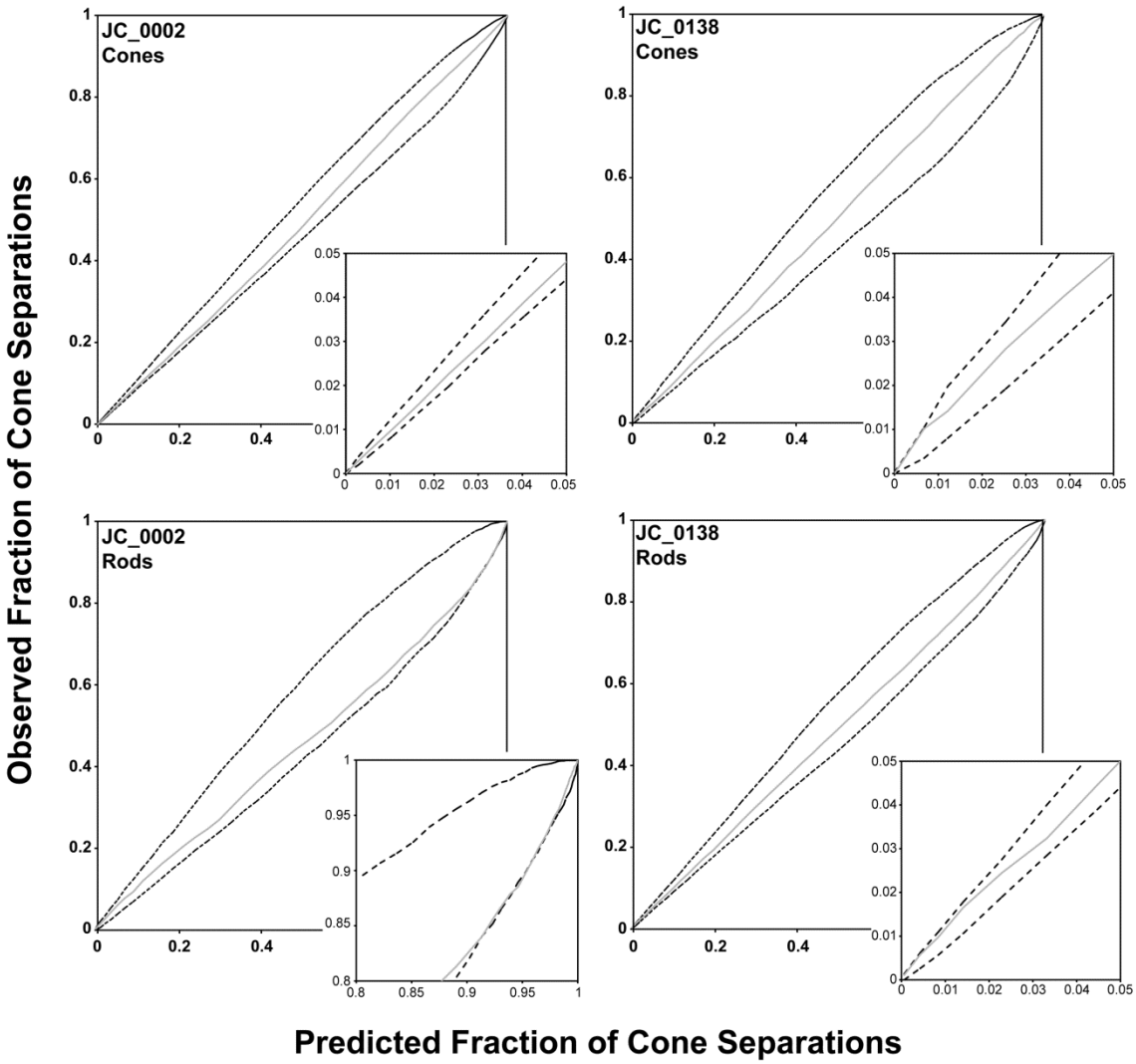

Figure 7.8: Cumulative histogram comparison (CHC) plots for the linear reflectance profile cells. In each plot, the solid line represents the fraction of intercell separations within a given distance for the actual cone or rod mosaic versus that for the average of 1000 random simulations. The minimum and maximum bounds of these simulations are given as dashed lines. The insets show areas of the CHC plots where the actual data approaches or exceeds the bounds of the random simulations.

Regardless, the general behavior of substantial inter-cell variation in reflectivity that has been well documented in cones appears to exist in the rods as well.

Spatial analysis of cell classification

As we identified each cell as having a linear or fluctuating reflectivity profile, we could examine whether the two submosaics were distributed randomly, or whether there was

any tendency for cells belonging to the same submosaic to be near each other. This analysis was done using a previously described technique (Diggle, 1983), which uses information about the photoreceptor mosaic on all spatial scales and has been used to examine the relative arrangement of long- and middle-wavelength sensitive cones within the trichromatic cone mosaic (Hofer et al., 2005; Roorda et al., 2001). The distances between each cell having a linear reflectance profile and every other cell having a linear reflectance profile was calculated, and a cumulative histogram of intercell distances was generated. Monte Carlo simulations (n = 1000) were used to compute the expected cumulative histogram of inter-cell distances in a random arranged mosaic. These random mosaics were generated by taking the (x,y) coordinates of all of the cells and randomly assigning a constant fraction of them to be linear. The average, minimum, and maximum cumulative histograms were calculated and compared to the actual cumulative histogram for that particular group of cells. **Figure 7.8** shows cumulative histogram comparisons (CHC) for all four data sets. The arrangement of the cells having linear reflectivity profiles within the overall cone (or rod) mosaic is indistinguishable from random for three of the four data sets, as evident by the fact that the CHC plot for the actual data does not fall outside of the minimum or maximum bounds of the random simulations. The rod mosaic of JC_0002 has a slight bias towards clumping (as the CHC inset reveals fewer large inter-rod distances compared to that of the random simulations). It was previously shown that a slight bias towards clumping of cones of like spectral subtype (long- or middle-wavelength sensitive) could be attributed to residual optical blur (Hofer et al., 2005; Roorda et al., 2001), and it may be that optical blur in our images also affects our analysis. As such, we conclude that the arrangement of cells having linear reflectivity profiles within the overall mosaic can be considered indistinguishable from random.

Discussion

We successfully imaged the rod and cone photoreceptor mosaic over 12 hours using an AOSLO. By registering images from different time points, we were able to track the reflectance behavior of individual rod and cone photoreceptors over time. As has been shown previously for cones, we find that individual rods vary in their reflectance over time. This suggests that a common physiological mechanism underlies this phenomenon. Moreover, at a given moment in time, the rod mosaic showed remarkable variation in rod-to-rod reflectivity, which has also been observed for the cone mosaic (Miller et al., 1996; Wade & Fitzke, 1998). The origin of the cell-cell variation remains to be elucidated; however our data would also suggest a common mechanism behind this feature of the rod and cone mosaics. Interestingly, our data reveal no tendency for neighboring cells to have the same reflectance profile behavior. As we develop techniques to further classify cells into additional archetypes, it will be interesting to re-examine the spatial arrangement of cells of like type.

There were a number of limitations of the current study. First, the results are based on only two subjects, though there is no reason to think that the findings do not represent a universal property of the healthy human rod photoreceptor mosaic. Second, a relatively coarse sampling (hourly) was used. Future experiments using finer time sampling are needed to better characterize the temporal variation of rod photoreceptors reflectance. Along these lines, it is worth noting that our classification scheme is rather arbitrary, but nevertheless illustrates the significant variability in reflectivity profiles among cones and rods.

Previous studies have suggested that differences in cone reflectivity observed in AO images are due to differences in the length of the outer segment (Jonnal et al., 2010; Jonnal et al., 2007). Specifically, it has been suggested that sinusoidal reflectance

oscillations can only be observed when using imaging sources with coherence lengths longer than that of the outer segment. However, both our results and those of Pallikaris et al. (Pallikaris et al., 2003), resulting from using light sources with coherence lengths shorter than twice the length of a photoreceptor outer segment, strongly indicate that fluctuations in photoreceptor reflectivity are not only attributable to interference between light reflected at opposite ends of the outer segments. It is plausible that local sub-cellular changes at either the anterior or posterior end of the outer segment contribute to the overall reflectance profile. More importantly, the reflectivity fluctuations reported in these studies, which notably using different imaging modalities, are an order of magnitude larger than those reported previously (Jonnal et al., 2010; Jonnal et al., 2007), and contained a more complex temporal behavior. The important point is that complete characterization of the origin of these reflectance changes will require the use of short and long coherence length sources.

Regardless of the exact origin of the reflectance changes observed here, the fact remains that they appear to be similar in both cones and rods – suggesting a common physiological process. Thus, examination of temporal variation of photoreceptor reflectance may provide a means for assessing relative rod photoreceptor health in aging and in retinal disease. If temporal reflectance fluctuation is a property of all photoreceptors in “normal” retina, then it follows that pathological retina may exhibit altered characteristics. Of particular interest would be examining patients who have defects in ciliary trafficking of proteins from the inner segment to the outer segment (Kimberling & Moller, 1995; Malm et al., 2011). Also of interest (and likely to be of more use clinically) are the optical reflectance changes of rods and cones in response to photic stimulation. Previous reports have suggested that this behavior may have its origin in the phototransduction cascade (Jonnal et al., 2007). The plethora of human mutations that selectively impair different components of the phototransduction cascade

(Daiger, Bowne, & Sullivan, 2007; Molday, 1998; Nishiguchi, Sandberg, Gorji, Berson, & Dryja, 2005; Perrault et al., 1999), combined with our ability to track the behavior of individual rods (and cones) over time, provides a unique opportunity to dissect, *in vivo*, the origin of these optical phenomena.

BIBLIOGRAPHY

Ahnelt, P. K., & Kolb, H. (2000). The mammalian photoreceptor mosaic-adaptive design. *Progress in Retinal and Eye Research, 19*(6), 711-777.

Arathorn, D. W., Yang, Q., Vogel, C. R., Zhang, Y., Tiruveedhula, P., & Roorda, A. (2007). Retinally stabilized cone-targeted stimulus delivery. *Optics Express, 15*(21), 13731-13744.

Artal, P., & Navarro, R. (1989). High-resolution imaging of the living human fovea: measurement of the intercenter cone distance by speckle interferometry. *Optics Letters, 14*(20), 1098-1100.

Babcock, H. W. (1953). The possibility of compensating astronomical seeing. *Publications of the Astronomical Society of the Pacific, 65*(386), 229-236.

Baraas, R. C., Carroll, J., Gunther, K. L., Chung, M., Williams, D. R., Foster, D. H., & Neitz, M. (2007). Adaptive optics retinal imaging reveals S-cone dystrophy in tritan color-vision deficiency. *Journal of the Optical Society of America A, 24*(5), 1438-1447.

Bedggood, P., & Metha, A. (2012). Variability in bleach kinetics and amount of photopigment between individual foveal cones. *Investigative Ophthalmology & Visual Science, 53*(7), 3673-3681.

Bennett, A. G., Rudnicka, A. R., & Edgar, D. F. (1994). Improvements on Littmann's method of determining the size of retinal features by fundus photography. *Graefe's Archive for Clinical and Experimental Ophthalmology, 232*(6), 361-367.

Berson, E. L. (1993). Retinitis Pigmentosa: The Friedenwald Lecture. *Investigative Ophthalmology & Visual Science, 34*(5), 1659-1676.

Bland, J. M., & Altman, D. G. (1986). Statistical methods for assessing agreement between two methods of clinical measurement. *Lancet, 1*(8476), 307-310.

Bland, J. M., & Altman, D. G. (1996). Statistics notes: measurement error. *British medical journal, 313*(7059), 744.

Bland, J. M., & Altman, D. G. (1999). Measuring agreement in method comparison studies. *Statistical Methods in Medical Research, 8*(2), 135-160.

Burns, S. A., Tumbar, R., Elsner, A. E., Ferguson, D., & Hammer, D. X. (2007). Large-field-of-view, modular, stabilized, adaptive-optics-based scanning laser ophthalmoscope. *Journal of the Optical Society of America A, 24*(5), 1313-1326.

Burns, S. A., Zhangyi, Z., Chui, T. Y. P., Song, H., Elsner, A. E., & Malinovsky, V. E. (2008). Imaging the inner retina using adaptive optics. *Investigative Ophthalmology & Visual Science, 49*, E-Abstract 4512.

Carroll, J., Baraas, R. C., Wagner-Schuman, M., Rha, J., Siebe, C. A., Sloan, C., . . . Neitz, M. (2009). Cone photoreceptor mosaic disruption associated with Cys203Arg mutation in the M-cone opsin. *Proceedings of the National Academy of Sciences, USA, 106*(49), 20948-20953.

Carroll, J., Choi, S. S., & Williams, D. R. (2008). In vivo imaging of the photoreceptor mosaic of a rod monochromat. *Vision Research, 48*(26), 2564-2568.

Carroll, J., Dubra, A., Gardner, J. C., Mizrahi-Meissonnier, L., Cooper, R. F., Dubis, A. M., . . . Michaelides, M. (2012). The effect of cone opsin mutations on retinal structure and the integrity of the photoreceptor mosaic. *Investigative Ophthalmology & Visual Science, 53*(13), 8006-8015.

Carroll, J., Kay, D. B., Scoles, D., Dubra, A., & Lombardo, M. (2013). Adaptive optics retinal imaging-clinical opportunities and challenges. *Current Eye Research, 38*(7), 709-721.

Carroll, J., McMahon, C., Neitz, M., & Neitz, J. (2000). Flicker-photometric electroretinogram estimates of L:M cone photoreceptor ratio in men with photopigment spectra derived from genetics. *Journal of the Optical Society of America A, 17*(3), 499-509.

Carroll, J., Neitz, M., Hofer, H., Neitz, J., & Williams, D. R. (2004). Functional photoreceptor loss revealed with adaptive optics: an alternate cause of color blindness. *Proceedings of the National Academy of Sciences USA, 101*(22), 8461-8466.

Carroll, J., Rossi, E. A., Porter, J., Neitz, J., Roorda, A., Williams, D. R., & Neitz, M. (2010). Deletion of the X-linked opsin gene array locus control region (LCR) results in disruption of the cone mosaic. *Vision Research, 50*(19), 1989-1999.

Chiu, S. J., Lokhnygina, Y., Dubis, A. M., Dubra, A., Carroll, J., Izatt, J. A., & Farsiu, S. (2013). Automatic cone photoreceptor segmentation using graph theory and dynamic programming. *Biomedical Optics Express, 4*(6), 924-937.

Choi, S. S., Doble, N., Hardy, J. L., Jones, S. M., Keltner, J. L., Olivier, S. S., & Werner, J. S. (2006). In vivo imaging of the photoreceptor mosaic in retinal dystrophies and correlations with visual function. *Investigative Ophthalmology & Visual Science, 47*(5), 2080-2092.

Chui, T. Y. P., Song, H., & Burns, S. A. (2008a). Adaptive-optics imaging of human cone photoreceptor distribution. *Journal of the Optical Society of America A, 25*(12), 3021-3029.

Chui, T. Y. P., Song, H. X., & Burns, S. A. (2008b). Individual variations in human cone photoreceptor packing density: variations with refractive error. *Investigative Ophthalmology & Visual Science, 49*(10), 4679-4687.

Cideciyan, A. V., Hufnagel, R. B., Carroll, J., Sumaroka, A., Luo, X., Schwartz, S. B., . . . Jacobson, S. G. (2013). Human cone visual pigment deletions spare sufficient

photoreceptors to warrant gene therapy. *Human Gene Therapy, 24*(12), 993-1006.

Coletta, N. J., & Williams, D. R. (1987). Psychophysical estimate of extrafoveal cone spacing. *Journal of the Optical Society of America A, 4*(8), 1503-1513.

Cook, J. E. (1996). Spatial properties of retinal mosaics: An empirical evaluation of some existing measures. *Visual Neuroscience, 13*(1), 15-30.

Cooper, R. F., Dubis, A. M., Pavaskar, A., Rha, J., Dubra, A., & Carroll, J. (2011). Spatial and temporal variation of rod photoreceptor reflectance in the human retina. *Biomedical Optics Express, 2*(9), 2577-2589.

Cooper, R. F., Harvey, Z., Dubow, M., Sulai, Y., Pinhas, A., Scoles, D., . . . Carroll, J. (2013). The effect of AOSLO image distortion on metrics of mosaic geometry. *Investigative Ophthalmology & Visual Science, 54*, E-Abstract 5546.

Cooper, R. F., Langlo, C. S., Dubra, A., & Carroll, J. (2013). Automatic detection of modal spacing (Yellott's ring) in adaptive optics scanning light ophthalmoscope images. *Ophthalmic & Physiological Optics, 33*(4), 540-549.

Cooper, R. F., Rha, J., Dubra, A., & Carroll, J. (2011). Examining FFT and direct counting estimates of photoreceptor density in adaptive optics retinal images. *Investigative Ophthalmology & Visual Science, 52*, E-Abstract 1321.

Curcio, C. A. (2001). Photoreceptor topography in ageing and age-related maculopathy. *Eye, 15*, 376-383.

Curcio, C. A., Allen, K. A., Sloan, K. R., Lerea, C. L., Hurley, J. B., Klock, I. B., & Milam, A. H. (1991). Distribution and morphology of human cone photoreceptors stained with anti-blue opsin. *The Journal of Comparative Neurology, 312*, 610-624.

Curcio, C. A., Millican, C. L., Allen, K. A., & Kalina, R. E. (1993). Aging of the human photoreceptor mosaic: Evidence for selective vulnerability of rods in central retina. *Investigative Ophthalmology & Visual Science, 34*(12), 3278-3296.

Curcio, C. A., Owsley, C., & Jackson, G. R. (2000). Spare the rods, save the cones in aging and age-related maculopathy. *Investigative Ophthalmology and Visual Science, 41*, 2015-2018.

Curcio, C. A., & Sloan, K. R. (1992). Packing geometry of human cone photoreceptors: Variation with eccentricity and evidence for local anisotropy. *Visual Neuroscience, 9*(2), 169-180.

Curcio, C. A., Sloan, K. R., Kalina, R. E., & Hendrickson, A. E. (1990). Human photoreceptor topography. *Journal of Comparative Neurology, 292*(4), 497-523.

Curcio, C. A., Sloan, K. R., & Meyers, D. (1989). Computer methods for sampling, reconstruction, display and analysis of retinal whole mounts. *Vision Research, 29*(5), 529-540.

Daiger, S. P., Bowne, S. J., & Sullivan, L. S. (2007). Perspective on genes on mutations causing retinitis pigmentosa. *Archives of Ophthalmology, 125*, 151-158.

Deans, S. R. (1983). *The Radon Transform and Some of Its Applications*. New York: John Wiley & Sons.

Dees, E. W., Dubra, A., & Baraas, R. C. (2011). Variability in parafoveal cone mosaic in normal trichromatic individuals. *Biomedical Optics Express, 2*(5), 1351-1358.

Diggle, P. J. (1983). *Statistical Analysis of Spatial Point Patterns*. London: Academic Press.

Doble, N., Choi, S. S., Codona, J. L., Christou, J., Enoch, J. M., & Williams, D. R. (2011). In vivo imaging of the human rod photoreceptor mosaic. *Opt Lett, 36*(1), 31-33.

Dubra, A., & Harvey, Z. (2010). Registration of 2D Images from Fast Scanning Ophthalmic Instruments. In B. Fischer, B. Dawant, & C. Lorenz (Eds.), *Biomedical Image Registration* (Vol. 6204, pp. 60-71): Springer Berlin / Heidelberg.

Dubra, A., & Sulai, Y. (2011). Reflective afocal broadband adaptive optics scanning ophthalmoscope. *Biomedical Optics Express, 2*(6), 1757-1768.

Dubra, A., Sulai, Y., Norris, J. L., Cooper, R. F., Dubis, A. M., Williams, D. R., & Carroll, J. (2011). Noninvasive imaging of the human rod photoreceptor mosaic using a confocal adaptive optics scanning ophthalmoscope. *Biomedical Optics Express, 2*(7), 1864-1876.

Duncan, J. L., Zhang, Y., Gandhi, J., Nakanishi, C., Othman, M., Branham, K. E. H., . . . Roorda, A. (2007). High-resolution imaging with adaptive optics in patients with inherited retinal degeneration. *Investigative Ophthalmology & Visual Science, 48*(7), 3283-3291.

Fay, J. D., Faridi, A., Garg, A., & Pennesi, M. E. (2012). Measuring the performance of an adaptive optics flood illuminated camera for imaging the cone mosaic in the clinical setting. *Investigative Ophthalmology & Visual Science, 53*, E-Abstract 5674.

Fernández, E. J., Hermann, B., Považay, B., Unterhuber, A., Sattmann, H., Hofer, B., . . . Drexler, W. (2008). Ultrahigh resolution optical coherence tomography and pancorrection for cellular imaging of the living human retina. *Optics Express, 16*(15), 11083-11094.

Flatter, J. A., Cooper, R. F., Dubow, M. J., Pinhas, A., Singh, R. S., Kapur, R., . . . Carroll, J. (2014). Outer retinal structure after closed-globe blunt ocular trauma. *Retina, 34*(10), 2133-2146.

Gao, H., & Hollyfield, J. G. (1992). Aging of the human retina: Differential loss of neurons and retinal pigment epithelial cells. *Investigative Ophthalmology & Visual Science, 33*(1), 1-17.

Garrioch, R., Langlo, C., Dubis, A. M., Cooper, R. F., Dubra, A., & Carroll, J. (2012). Repeatability of in vivo parafoveal cone density and spacing measurements. *Optometry and Vision Science, 89*(5), 632-643.

Genead, M. A., Fishman, G. A., Rha, J., Dubis, A. M., Bonci, D. M., Dubra, A., . . . Carroll, J. (2011). Photoreceptor structure and function in patients with congenital achromatopsia. *Investigative Ophthalmology & Visual Science, 52*(10), 7298-7308.

Godara, P., Cooper, R. F., Sergouniotis, P. I., Diederichs, M. A., Streb, M. R., Genead, M. A., . . . Carroll, J. (2012). Assessing retinal structure in complete congenital stationary night blindness and Oguchi disease. *American Journal of Ophthalmology, 154*(6), 987-1001.

Godara, P., Wagner-Schuman, M. L., Rha, J., Connor, T. B., Stepien, K., & Carroll, J. (2012). Imaging the photoreceptor mosaic with adaptive optics: beyond counting cones. *Advances in Experimental Medicine and Biology, 723*, 451-458.

Gómez-Vieyra, A., Dubra, A., Malacara-Hernández, D., & Williams, D. R. (2009). First-order design of off-axis reflective ophthalmic adaptive optics systems using afocal telescopes. *Optics Express, 17*(21), 18906-18919.

Grieve, K., & Roorda, A. (2008). Intrinsic signals from human cone photoreceptors. *Investigative Ophthalmology & Visual Science, 49*(2), 713-719.

Han, D. P., Croskrey, J. A., Dubis, A. M., Schroeder, B., Rha, J., & Carroll, J. (2012). Adaptive optics and spectral-domain optical coherence tomography of human photoreceptor structure after short duration pascal macular grid and panretinal laser photocoagulation. *Archives of Ophthalmology, 130*(4), 518-521.

Hansen, S. O., Cooper, R. F., Dubra, A., Carroll, J., & Weinberg, D. V. (2013). Selective cone photoreceptor injury in acute macular neuroretinopathy. *Retina, 33*(8), 1650-1658.

Hardy, J. W. (1998). *Adaptive Optics for Astronomical Telescopes*. New York: Oxford University Press.

Helmholtz, H. (1851). Beschreibung des Augenspiegels (pp. 28-34): Springer Berlin Heidelberg.

Helmholtz, H. v. (1866). *Treatise on Physiological Optics* (J. P. C. Southall, Trans. 2nd ed. Vol. 1962). New York: Dover.

Hermann, B., Fernández, E. J., Unterhuber, A., Sattmann, H., Fercher, A. F., Drexler, W., . . . Artal, P. (2004). Adaptive-optics ultrahigh-resolution optical coherencetomography. *Optics Letters, 29*(18), 2142-2144.

Hirsch, J., & Hylton, R. (1984). Orientation dependence of visual hyperacuity contains a component with hexagonal symmetry. *Journal of the Optical Society of America A, 1*(3), 300-308.

Hirsch, J., & Miller, W. H. (1987). Does cone positional disorder limit resolution. *Journal of the Optical Society of America A, 4*(8), 1481-1492.

Hoang, Q. V., Linsenmeier, R. A., Chung, C. K., & Curcio, C. A. (2002). Photoreceptor inner segments in monkey and human retina: Mitochondrial density, optics, and regional variation. *Visual Neuroscience, 19*, 395-407.

Hofer, H., Artal, P., Singer, B., Aragon, J. L., & Williams, D. R. (2001). Dynamics of the eye's wave aberration. *Journal of the Optical Society of America A, 18*, 497-506.

Hofer, H., Carroll, J., Neitz, J., Neitz, M., & Williams, D. R. (2005). Organization of the human trichromatic cone mosaic. *Journal of Neuroscience, 25*(42), 9669-9679.

Hofer, H., Carroll, J., & Williams, D. R. (2009). Photoreceptor Mosaic. In R. S. Editor-in-Chief: Larry (Ed.), *Encyclopedia of Neuroscience* (pp. 661-668). Oxford: Academic Press.

Iglesias, I., Ragazzoni, R., Julien, Y., & Artal, P. (2002). Extended source pyramid wave-front sensor for the human eye. *Optics Express, 10*(9), 419-428.

Jonnal, R. S., Besecker, J. R., Derby, J. C., Kocaoglu, O. P., Cense, B., Gao, W., . . . Miller, D. T. (2010). Imaging outer segment renewal in living human cone photoreceptors. *Optics Express, 18*(5), 5257-5270.

Jonnal, R. S., Rha, J., Zhang, Y., Cense, B., Gao, W., & Miller, D. T. (2007). In vivo functional imaging of human cone photoreceptors. *Optics Express, 14*(24), 16141-16160.

Kay, D. B., Land, M. E., Cooper, R. F., Dubis, A. M., Godara, P., Dubra, A., . . . Stepien, K. E. (2013). Outer retinal structure in best vitelliform macular dystrophy. *Journal of the American Medical Association Ophthalmology, 131*(9), 1207-1215.

Kimberling, W. J., & Moller, C. (1995). Clinical and molecular genetics of Usher syndrome. *Journal of the American Academy of Audiology, 6*, 63-72.

Kocaoglu, O. P., Cense, B., Jonnal, R. S., Wang, Q., Lee, S., Gao, W., & Miller, D. T. (2011). Imaging retinal nerve fiber bundles using optical coherence tomography with adaptive optics. *Vision Research, 51*(16), 1835-1844.

Kocaoglu, O. P., Lee, S., Jonnal, R. S., Wang, Q., Herde, A. E., Derby, J. C., . . . Miller, D. T. (2011). Imaging cone photoreceptors in three dimensions and in time using ultrahigh resolution optical coherence tomography with adaptive optics. *Biomedical Optics Express, 2*(4), 748-763.

Krispel, C. M., Chen, D., Melling, N., Chen, Y. J., Martemyanov, K. A., Quillinan, N., . . . Burns, M. E. (2006). RGS expression rate-limits recovery of rod photoresponses. *Neuron, 51*(4), 409-416.

Kuhn, H., & Wilden, U. (1987). Deactivation of photoactivated rhodopsin by rhodopsin-kinase and arrestin. *Journal of Receptor Research, 7*(1-4), 283-298.

Larocca, F., Nankivil, D., Farsiu, S., & Izatt, J. A. (2013). Handheld simultaneous scanning laser ophthalmoscopy and optical coherence tomography system. *Biomedical Optics Express, 4*(11), 2307-2321.

Li, K. Y., & Roorda, A. (2007). Automated identification of cone photoreceptors in adaptive optics retinal images. *Journal of the Optical Society of America A, 24*(5), 1358-1363.

Li, K. Y., Tiruveedhula, P., & Roorda, A. (2010). Intersubject variability of foveal cone photoreceptor density in relation to eye length. *Investigative Ophthalmology & Visual Science, 51*(12), 6858-6867.

Liang, J., Grimm, B., Goelz, S., & Bille, J. (1994). Objective measurement of the wave aberrations of the human eye using a Hartmann-Shack wavefront sensor. *Journal of the Optical Society of America A, 11*, 1949-1957.

Liang, J., Williams, D. R., & Miller, D. (1997). Supernormal vision and high-resolution retinal imaging through adaptive optics. *Journal of the Optical Society of America A, 14*(11), 2884-2892.

Llorente, L., Barbero, S., Cano, D., Dorronsoro, C., & Marcos, S. (2004). Myopic versus hyperopic eyes: axial length, corneal shape, and optical aberrations. *Journal of Vision, 4*(4), 288-298.

Lombardo, M., Lombardo, G., Schiano Lomoriello, D., Ducoli, P., Stirpe, M., & Serrao, S. (2013). Interocular symmetry of parafoveal photoreceptor cone density. *Retina, 33*(8), 1640-1649.

Lombardo, M., Serrao, S., Ducoli, P., & Lombardo, G. (2013). Eccentricity dependent changes of density, spacing and packing arrangement of parafoveal cones. *Ophthalmic & Physiological Optics, 33*(4), 516-526.

Lombardo, M., Serrao, S., & Lombardo, G. (2014). Technical factors influencing cone packing density estimates in adaptive optics flood illuminated retinal images. *Public Library of Science ONE, 9*(9), e107402.

Malm, E., Ponjavic, V., Moller, C., Kimberling, W. J., Stone, E. S., & Andreasson, S. (2011). Alteration of rod and cone function in children with Usher syndrome. *European Journal of Ophthalmology, 21*, 30-38.

Martin, J. A., & Roorda, A. (2009). Pulsatility of parafoveal capillary leukocytes. *Experimental Eye Research, 88*(3), 3563-3560.

Masella, B., Morgan, J. I. W., Merigan, W., Gray, D. C., Hunter, J. J., Wolfe, R., . . . Williams, D. R. (2007). *Retinal damage observed with autofluorescence imaging of retinal pigment epithelium cells in vivo*. Paper presented at the ARVO Annual Meeting, Fort Lauderdale, Florida, USA.

Meitav, N., & Ribak, E. N. (2011). Measuring the ordering of closely-packed particles. *Applied Physics Letters, 99*(22), 1-3.

Menghini, M., Lujan, B. J., Zayit-Soudry, S., Syed, R., Porco, T. C., Bayabo, K., . . . Duncan, J. L. (2015). Correlation of outer nuclear layer thickness with cone density values in patients with retinitis pigmentosa and healthy subjects. *Investigative Ophthalmology & Visual Science, 56*(1), 372-381.

Merino, D., Dainty, C., Bradu, A., & Podoleanu, A. G. (2006). Adaptive optics enhanced simultaneous *en-face* optical coherence tomography and scanning laser ophthalmoscopy. *Optics Express, 14*(8), 3345-3353.

Merino, D., Duncan, J. L., Tiruveedhula, P., & Roorda, A. (2011). Observation of cone and rod photoreceptors in normal subjects and patients using a new generation adaptive optics scanning laser ophthalmoscope. *Biomedical Optics Express, 2*(8), 2189-2201.

Méry, J. (1704). Des mouvements de l'Iris et par occasion de la partie principale de l'organe de la Vuë. *Mémoire de l'Açademie des Sciences, 23*, 277-284.

Miller, D. T., Kocaoglu, O. P., Wang, Q., & Lee, S. (2011). Adaptive optics and the eye (super resolution OCT). *Eye (London), 25*(3), 321-330.

Miller, D. T., Williams, D. R., Morris, G. M., & Liang, J. (1996). Images of cone photoreceptors in the living human eye. *Vision Research, 36*, 1067-1079.

Mkrtchyan, M., Lujan, B. J., Merino, D., Roorda, A., & Duncan, J. L. (2012). Outer retinal structure in patients with acute zonal occult outer retinopathy. *American Journal of Ophthalmology, 153*(4), 757-768.

Molday, R. S. (1998). Photoreceptor membrane proteins, phototransduction, and retinal degenerative diseases. The Friedenwald Lecture. *Investigative Ophthalmology & Visual Science, 39*, 2491-2513.

Morgan, J. I., Hunter, J. J., Masella, B., Wolfe, R., Gray, D. C., Merigan, W. H., . . . Williams, D. R. (2008a). Light-induced retinal changes observed with high-resolution autofluorescence imaging of the retinal pigment epithelium. *Investigative Ophthalmology & Visual Science, 49*(8), 3715-3729.

Morgan, J. I. W., Chung, D. C., Nozato, K., Maguire, A. M., & Bennett, J. (2012). Imaging retinal structure in patients and carriers of choroidermia. *Investigative Ophthalmology & Visual Science, 53*, E-Abstract 4648.

Morgan, J. I. W., Gray, D. C., Wolfe, R., Masella, B., Dubra, A., & Williams, D. R. (2007). *Imaging individual human retinal pigment epithelium cells in vivo*. Paper presented at the ARVO Annual Meeting, Fort Lauderdale, Florida, USA.

Morgan, J. I. W., Hunter, J. J., Masella, B., Wolfe, R., Gray, D. C., Merigan, W. H., . . . Williams, D. R. (2008b). Light-induced retinal changes observed with high-resolution autofluorescence imaging of the retinal pigment epithelium. *Investigative Ophthalmology & Visual Science, 49*(8), 3715-3729.

Mujat, M., Ferguson, R. D., Patel, A. H., Iftimia, N., Lue, N., & Hammer, D. X. (2010). High resolution multimodal clinical ophthalmic imaging system. *Optics Express, 18*(11), 11607-11621.

Myronenko A., S. X. (2010). Point-set registration: coherent point drift. *IEEE Transactions on Pattern Analysis and Machine Intelligence, 32*(12), 2262-2275.

Neitz, J., Wagner-Schuman, M., Dubra, A., Sjoberg, S. A., Moore, A. T., Young, T. L., . . . Michaelides, M. (2011). Cone mosaic disruption caused by L/M opsin mutations in Bornholm Eye Disease. *Investigative Ophthalmology & Visual Science, 52*, E-Abstract: 4896.

Newsome, D. A. (1988). Retinitis pigmentosa, Usher's syndrome, and other pigmentary retinopathies. In D. A. Newsome (Ed.), *Retinal dystrophies and degenerations* (pp. 161-194). New York: Raven Press.

Nikonov, S., Kholodenko, R., Lem, J., & Pugh Jr., E. N. (2006). Physiological Features of the S- and M-cone Photoreceptors of Wild-type Mice from Single-cell Recordings. *The Journal of Cell Biology, 127*(4), 359-374.

Nishiguchi, K. M., Sandberg, M. A., Gorji, N., Berson, E. L., & Dryja, T. P. (2005). Cone cGMP-gated channel mutations and clinical findings in patients with achromatopsia, macular degeneration, and other hereditary cone diseases. *Human Mutation, 25*, 248-258.

Oyster, C. W. (1999). *The Human Eye: Structure and Function*. Sunderland, MA: Sinauer Associates, Inc.

Packer, O., Hendrickson, A. E., & Curcio, C. A. (1989). Photoreceptor topography of the retina in the adult pigtail macaque (*Macaca nemestrina*). *The Journal of Comparative Neurology, 288*, 165-183.

Pallikaris, A., Williams, D. R., & Hofer, H. (2003). The reflectance of single cones in the living human eye. *Investigative Ophthalmology & Visual Science, 44*(10), 4580-4592.

Park, S. P., Chung, J. K., Greenstein, V., Tsang, S. H., & Chang, S. (2013). A study of factors affecting the human cone photoreceptor density measured by adaptive optics scanning laser ophthalmoscope. *Experimental Eye Research, 108*, 1-9.

Patel, P. J., Chen, F. K., Ikeji, F., & Tufail, A. (2011). Intersession repeatability of optical coherence tomography measures of retinal thickness in early age-related macular degeneration. *Acta Ophthalmologica, 89*(3), 229-234.

Perrault, I., Rozet, J. M., Gerber, S., Ghazi, I., Leowski, C., Ducroq, D., . . . Kaplan, J. (1999). Leber congenital amaurosis. *Molecular Genetics and Metabolism, 68*, 200-208.

Pircher, M., Kroisamer, J. S., Felberer, F., Sattmann, H., Götzinger, E., & Hitzenberger, C. K. (2010). Temporal changes of human cone photoreceptors observed in vivo with SLO/OCT. *Biomedical Optics Express, 2*(1), 100-112.

Pircher, M., & Zawadzki, R. J. (2007). Combining adaptive optics with optical coherence tomography: unveiling the cellular structure of the retina *in vivo*. *Expert Review of Ophthalmology, 2*(6), 1019-1035.

Pircher, M., Zawadzki, R. J., Evans, J. W., Werner, J. S., & Hitzenberger, C. K. (2008). Simultaneous imaging of human cone mosaic with adaptive optics enhanced scanning laser ophthalmoscopy and high-speed transversal scanning optical coherence tomography. *Optics Letters, 33*(1), 22-24.

Polyak, S. (1957). *The Vertebrate Visual System*. Chicago: University of Chicago Press.

Polyak, S. L. (1941). *The Retina*. Chicago: The University of Chicago Press.

Popovic, Z., Knutsson, P., Thaung, J., Owner-Peterson, M., & Sjöstrand, J. (2011). Noninvasive imaging of human foveal capillary network using dual-conjugate adaptve optics. *Investigative Ophthalmology & Visual Science, 52*(5), 2649-2655.

Pugh, E. N. J., & Lamb, T. D. (2000). Phototransduction in vertebrate rods and cones: Molecular mechanisms of amplification, recovery, and light adaptation. In D. G. Stavenga, W. J. DeGrip, & E. N. J. Pugh (Eds.), *Molecular Mechanisms in Visual Transduction* (Vol. 3). Amsterdam: Elsevier.

Pum, D., Ahnelt, P. K., & Grasl, M. (1990). Iso-orientation areas in the foveal cone mosaic. *Visual Neuroscience, 5*, 511-523.

Purves, D., Augustine, G. J., Fitzpatrick, D., Hall, W. C., LaMantia, A., & White, L. E. (2011). *Neuroscience* (5 ed.): Sinauer Associates, Inc.

Putnam, N. M., Hofer, H. J., Doble, N., Chen, L., Carroll, J., & Williams, D. R. (2005). The locus of fixation and the foveal cone mosaic. *Journal of Vision, 5*(7), 632-639.

Putnam, N. M., Hofer, H.J., Doble, N., Chen, L., Williams, D.R. (2003). The fixational stability of the human eye measured by imaging the cone mosaic. *Investigative Ophthalmology & Visual Science, 44*(13), 4196.

Ramaswamy, G., & Devaney, N. (2013). Pre-processing, registration and selection of adaptive optics corrected retinal images. *Ophthalmic and Physiological Optics, 33*(4), 527-539.

Ratnam, K., Carroll, J., Porco, T. C., Duncan, J. L., & Roorda, A. (2013). Relationship between foveal cone structure and clinical measures of visual function in patients with inherited retinal degenerations. *Investigative Ophthalmology & Visual Science, 54*(8), 5836-5847.

Ratnam, K., Västinsalo, H., Roorda, A., Sankila, E.-M. K., & Duncan, J. L. (2013). Cone structure in patients with Usher syndrome type III and mutations in the *Clarin 1* gene. *Journal of the American Medical Association Ophthalmology, 131*(1), 67-74.

Rha, J., Jonnal, R. S., Thorn, K. E., Qu, J., Zhang, Y., & Miller, D. T. (2006). Adaptive optics flood-illumination camera for high speed retinal imaging. *Optics Express, 14*(10), 4552-4569.

Rha, J., Jonnal, R. S., Zhang, Y., Cense, B., Gao, W., & Miller, D. T. (2006). Dependence of cone scintillation on photopigment bleaching and coherence length of the imaging light source. *Investigative Ophthalmology & Visual Science, 47*, E-abstract 1555.

Rha, J., Jonnal, R. S., Zhang, Y., & Miller, D. T. (2005). Rapid fluctuation in the reflectance of single cones and its dependence on photopigment bleaching. *Investigative Ophthalmology & Visual Science, 46*, E-abstract 3546.

Rha, J., Schroeder, B., Godara, P., & Carroll, J. (2009). Variable optical activation of human cone photoreceptors visualized using short coherence light source. *Optics Letters, 34*(24), 3782-3784.

Rodieck, R. W. (1991). The density recovery profile: A method for the analysis of points in the plane applicable to retinal studies. *Visual Neuroscience, 6*, 95-111.

Roorda, A., Garcia, C. A., Martin, J. A., Poonja, S., Queener, H., Romero-Borja, F., . . . Zhang, Y. (2006). What can adaptive optics do for a scanning laser ophthalmoscope? *Bulletin de la Societe belge d'ophtalmologie*(302), 231-244.

Roorda, A., Metha, A. B., Lennie, P., & Williams, D. R. (2001). Packing arrangement of the three cone classes in primate retina. *Vision Research, 41*, 1291-1306.

Roorda, A., Romero-Borja, F., Donnelly, W. J., Queener, H., Hebert, T. J., & Campbell, M. C. W. (2002). Adaptive optics scanning laser ophthalmoscopy. *Optics Express, 10*(9), 405-412.

Roorda, A., & Williams, D. R. (1999). The arrangement of the three cone classes in the living human eye. *Nature (London), 397*, 520-522.

Roorda, A., & Williams, D. R. (2002). Optical fiber properties of individual human cones. *Journal of Vision, 2*(5), 404-412.

Roorda, A., Zhang, Y., & Duncan, J. L. (2007). High-resolution in vivo imaging of the RPE mosaic in eyes with retinal disease. *Investigative Ophthalmology & Visual Science, 48*(5), 2297-2303.

Rossi, E. A., Carroll, J., & Roorda, A. (2008). The relationship between the cone photoreceptor mosaic and visual acuity in normal observers and blue cone monochromat carriers. *Journal of Vision, 8*(17), 20a.

Rossi, E. A., Chung, M., Dubra, A., Hunter, J. J., Merigan, W. H., & Williams, D. R. (2011). Imaging retinal mosaics in the living eye. *Eye*, 1-8.

Rossi, E. A., & Roorda, A. (2010). The relationship between visual resolution and cone spacing in the human fovea. *Nature Neuroscience, 13*(2), 156-157.

Scoles, D., Higgins, B. P., Cooper, R. F., Dubis, A. M., Summerfelt, P., Weinberg, D. V., . . . Dubra, A. (2014). Microscopic inner retinal hyper-reflective phenotypes in retinal and neurologic disease. *Investigative Ophthalmology & Visual Science, 55*(7), 4015-4029.

Scoles, D., Sulai, Y. N., & Dubra, A. (2013). In vivo dark-field imaging of the retinal pigment epithelium cell mosaic. *Biomedical Optics Express, 4*(9), 1710-1723.

Scoles, D. H., Sulai, Y. N., Langlo, C., Fishman, G. A., Curcio, C. A., Carroll, J., & Dubra, A. (2014). In vivo imaging of human cone photoreceptor inner segments. *Investigative Ophthalmology & Vision Science, 55*(7), 4244-4251.

Scoles, D. H., Sulai, Y. N., Manguikian, A. D., Shareef, S., & Dubra, A. (2012). Reflectance adaptive optics nerve fiber layer imaging in primary open angle glaucoma. *Investigative Ophthalmology & Visual Science, 53*, E-Abstract: 6957.

Sharpe, L. T., Stockman, A., Jägle, H., & Nathans, J. (1999). Opsin genes, cone photopigments, color vision, and color blindness. In K. R. Gegenfurtner & L. T. Sharpe (Eds.), *Color Vision: From Genes to Perception* (pp. 3-52). New York: Cambridge University Press.

Sheehy, C. K., Yang, Q., Arathorn, D. W., Tiruveedhula, P., de Boer, J. F., & Roorda, A. (2012). High-speed, image-based eye tracking with a scanning laser ophthalmoscope. *Biomedical Optics Express, 3*(10), 2611-2622.

Song, H., Chui, T. Y., Zhong, Z., Elsner, A. E., & Burns, S. A. (2011). Variation of cone photoreceptor packing density with retinal eccentricity and age. *Investigative Ophthalmology and Visual Science, 52*(10), 7376-7384.

Sredar, N., Ivers, K. M., Queener, H. M., Zouridakis, G., & Porter, J. (2013). A principal component analysis based approach to determine predominant lamina cribrosa beam orientation directly from in vivo images. *Journal of Vision, 13*(15), 36.

Stillinger, F. H., Jr. , DiMarzio, E. A., & Kornegay, R. L. (1964). Systematic approach to explanation of the rigid disk phase transition. *Journal of Chemical Physics, 40*(6), 1564-1576.

Sulai, Y. N., & Dubra, A. (2012). Adaptive optics scanning ophthalmoscopy with annular pupils. *Biomedical Optics Express, 3*(7), 1647-1661.

Syed, R., Sundquist, S. M., Ratnam, K., Zayit-Soudry, S., Zhang, Y., Crawford, J. B., . . . Duncan, J. L. (2013). High-resolution images of retinal structure in patients with choroideremia. *Investigative Ophthalmology and Visual Science, 54*(2), 950-961.

Tachibanaki, S., Arinobu, D., Shimauchi-Matsukawa, Y., Tsushima, S., & Kawamura, S. (2005). Highly effective phosphorylation by G protein-coupled receptor kinase 7 of light-activated visual pigment in cones. *Proceedings of the National Academy of Sciences of the USA, 102*(26), 9329-9334.

Tachibanaki, S., Tsushima, S., & Kawamura, S. (2001). Low amplification and fast visual pigment phosphorylation as mechanisms characterizing cone photoresponses.

Proceedings of the National Academy of Sciences of the USA, 98(24), 14044-14049.

Takayama, K., Ooto, S., Hangai, M., Arakawa, N., Oshima, S., Shibata, N., . . . Yoshimura, N. (2012). High-resolution imaging of the retinal nerve fiber layer in normal eyes using adaptive optics scanning laser ophthalmoscopy. *Public Library of Science ONE, 7*(3), e33158.

Takayama, K., Ooto, S., Hangai, M., Ueda-Arakawa, N., Yoshida, S., Akagi, T., . . . Yoshimura, N. (2013). High-resolution imaging of retinal nerve fiber bundles in glaucoma using adaptive optics scanning laser ophthalmoscopy. *American Journal of Ophthalmology, 155*(5), 870-881.

Tam, J., Dhamdhere, K. P., Tiruveedhula, P., Manzanera, S., Barez, S., Bearse Jr., M. A., . . . Roorda, A. (2011). Disruption of the retinal parafoveal capillary newtork in type 2 diabetes before the onset of diabetic retinopathy. *Investigative Ophthalmology & Visual Science, 52*(12), 9257-9266.

Tam, J., Martin, J. A., & Roorda, A. (2010). Non-invasive visualization and analysis of parafoveal capillaries in humans. *Investigative Ophthalmology & Visual Science, 51*(3), 1691-1698.

Torti, C., Považay, B., Hofer, B., Unterhuber, A., Carroll, J., Ahnelt, P. K., & Drexler, W. (2009). Adaptive optics optical coherence tomography at 120,000 depth scans/s for non-invasive cellular phenotyping of the living human retina. *Optics Express, 17*(22), 19382-19400.

Tyson, R. K. (1997). *Principles of Adaptive Optics* (2nd ed.). San Diego: Academic Press.

Vogel, C. R., Arathorn, D. W., Roorda, A., & Parker, A. (2006). Retinal motion estimation in adaptive optics scanning laser ophthalmoscopy. *Optics Express, 14*(2), 487-497.

Wade, A. R., & Fitzke, F. W. (1998). In vivo imaging of the human cone-photoreceptor mosaic using a confocal laser scanning ophthalmoscope. *Lasers and Light in Ophthalmology, 8*(3), 129-136.

Wagner-Schuman, M., Neitz, J., Rha, J., Williams, D. R., Neitz, M., & Carroll, J. (2010). Color-deficient cone mosaics associated with Xq28 opsin mutations: a stop codon versus gene deletions. *Vision Research, 50*(23), 2396-2402.

Wang, Q., Tuten, W. S., Lujan, B. J., Holland, J., Bernstein, P. S., Schwartz, S. D., . . . Roorda, A. (2015). Adaptive optics microperimetry and OCT images show preserved function and recovery of cone visibility in macular telangiectasia type 2 retinal lesions. *Investigative Ophthalmology & Visual Science, 56*(2), 778-786.

Weiss, E. R., Ducceschi, M. H., Horner, T. J., Li, A., Craft, C. M., & Osawa, S. (2001). Species-specific differences in expression of G-protein-coupled receptor kinase (GRK) 7 and GRK1 in mammalian cone photoreceptor cells: implications for cone cell phototransduction. *Journal of Neuroscience, 21*(23), 9175-9184.

Wilk, M. A., McAllister, J. T., Cooper, R. F., Dubis, A. M., Patitucci, T. N., Summerfelt, P., . . . Carroll, J. (2014). Relationship between foveal cone specialization and pit morphology in albinism. *Investigative Ophthalmology & Visual Science, 55*(7), 4186-4198.

Williams, D. R. (2011). Imaging single cells in the living retina. *Vision Research, 51*(13), 1379-1396.

Williams, D. R., & Coletta, N. J. (1987). Cone spacing and the visual resolution limit. *Journal of the Optical Society of America A, 4*(8), 1514-1523.

Wojtas, D. H., Wu, B., Ahnelt, P. K., Bones, P. J., & Millane, R. P. (2008). Automated analysis of differential interference contrast microscopy images of the foveal cone mosaic. *Journal of the Optical Society of America A, 25*(5), 1181-1189.

Wolsley, C. J., Saunders, K. J., Silvestri, G., & Anderson, R. S. (2010). Comparing mfERGs with estimates of cone density from in vivo imaging of the photoreceptor mosaic using a modified Heidelberg retina tomograph. *Vision Research, 50*(15), 1462-1468.

Yellott, J. I., Jr. (1982). Spectral analysis of spatial sampling by photoreceptors: topological disorder prevents aliasing. *Vision Research, 22*(9), 1205-1210.

Yellott, J. I., Jr. (1983). Spectral consequences of photoreceptor sampling in the rhesus monkey. *Science, 221*(4608), 382-385.

Yoon, M. K., Roorda, A., Zhang, Y., Nakanishi, C., Wong, L. J., Zhang, Q., . . . Duncan, J. L. (2009). Adaptive optics scanning laser ophthalmoscopy images in a family with the mitochondrial DNA T8993C mutation. *Investigative Ophthalmology & Visual Science, 50*(4), 1838-1847.

Zawadzki, R. J., Cense, B., Zhang, Y., Choi, S. S., Miller, D. T., & Werner, J. S. (2008). Ultrahigh-resolution optical coherence tomography with monochromatic and chromatic aberration correction. *Optics Express, 16*(11), 8126-8143.

Zawadzki, R. J., Choi, S. S., Fuller, A. R., Evans, J. W., Hamann, B., & Werner, J. S. (2009). Cellular resolution volumetric in vivo retinal imaging with adaptive optics-optical coherence tomography. *Optics Express, 17*(5), 4084-4094.

Zhang, T., Godara, P., Blancob, E.R., Griffin, R.L., Wang, X., Curcio, C.A., Zhang, Y. (2015). Variability in human cone topography assessed by adaptive optics scanning laser ophthalmoscopy. *American Journal of Ophthalmology, 160*(2), 290-300.

Zhang, Y., Cense, B., Rha, J., Jonnal, R. S., Gao, H., Zawadzki, R. J., . . . Miller, D. T. (2006). High-speed volumetric imaging of cone photoreceptors with adaptive optics spectral-domain optical coherence tomography. *Optics Express, 14*(10), 4380-4394.

Zhang, Y., Rha, J. T., Jonnal, R. S., & Miller, D. T. (2005). Adaptive optics parallel spectral domain optical coherence tomography for imaging the living retina. *Optics Express, 13*(12), 4792-4811.

Zhong, Z., Petrig, B. L., Qi, X., & Burns, S. A. (2008). In vivo measurement of erythrocyte velocity and retinal blood flow using adaptive optics scanning laser ophthalmoscopy. *Optics Express, 16*(17), 12746-12756.